

Politecnico di Torino

Politecnico di Torino

Energy and Nuclear Engineering

A.a. 2025/2026

Graduation Session September 2026

Multiphysics modelling for a NuScale-like SMR core using the Kraken framework

Supervisors:

Dr. N. Abrate
Dr. J. Bartos
Prof. A. Froio
Dr. S. Wijaya

Candidate:

Pietro Borelli

Abstract

In modern nuclear reactor analysis, high-fidelity multiphysics modeling has become essential to accurately model the interactions between different physical phenomena while reducing the need for conservative assumptions.

Conducted at NRG Pallas, this thesis focuses on gaining practical experience in multiphysics coupling utilizing the Kraken computational framework, developed by the VTT Technical Research Centre of Finland. The primary objective is to implement and assess a 3D full-core multiphysics model of a NuScale-like Small Modular Reactor. The coupled model is developed using a systematic, step-by-step approach.

First, a standalone deterministic neutronic model based on the nodal diffusion solver Ants is developed using the two-step approach. Serpent2, a 3D continuous-energy Monte Carlo code, is used to homogenize and generate burnup-dependent two-group cross-section libraries to be used in the nodal solver. The equilibrium cycle is then obtained by depleting the whole core and shuffling the fuel based on the NuScale three-batch fuel management strategy. The standalone deterministic model is compared with a full-core Serpent simulation, showing good agreement. The difference in critical boron concentration remains below 20 ppm, while the maximum difference in radial power is below 2%.

Subsequently, the neutronic solver is coupled with the porous-medium thermal-hydraulic code Kharon, allowing for an accurate evaluation of the coolant temperature and density. Finally, the fuel behavior module SuperFINIX is introduced to account for the Doppler feedback. This step-by-step integration evaluates how the transition from uniform fuel and coolant temperatures to spatially resolved thermal fields affects key reactor parameters, showing the changes in the axial power profile and the required critical boron concentration for the whole cycle operation. Results indicate that the thermal-hydraulic coupling modifies the axial power distribution at the beginning of the cycle and introduces a reactivity difference of approximately 250 pcm. However, including fuel behavior shows that the thermal-hydraulic and fuel temperature feedbacks partially compensate each other in terms of global reactivity.

Lastly, in line with the Best Estimate Plus Uncertainty approach, an Uncertainty Quantification analysis is performed on a simplified version of the coupled model. Specifically, the analysis is conducted on the full-core coupled neutronic and thermal-hydraulic model. A random sampling technique is used to evaluate how uncertainties in the input parameters (core power, coolant flow rate, outlet pressure, and inlet temperature) propagate to the calculated critical boron concentration. The analysis identifies inlet temperature and core power as the parameters with the greatest influence on the critical boron concentration, resulting in an overall standard deviation of approximately 18 ppm.

Table of Contents

List of Tables VI

List of Figures VII

Glossary XI

1 Introduction 1

1.1 Background 1

1.2 Objectives and structure of the thesis 2

1.3 Literature Review 2

2 Theoretical Background 5

2.1 Neutronics 5

2.1.1 Computational Methods in Reactor Physics 6

2.1.2 The Two-Step Calculation Approach 8

2.1.3 Burnup and Depletion Calculation 11

2.2 Core Thermal-Hydraulics 12

2.3 Fuel Thermomechanics 13

2.3.1 Thermal Behaviour and Heat Transfer 13

2.3.2 Mechanical Behaviour 14

2.4 Multiphysics Feedback 15

3 Methodology 17

3.1 Reactor Model 17

3.1.1 Core and Fuel Assembly 18

3.1.2 Core Design 21

3.2 The Kraken multiphysics framework . . . 22
3.2.1 Neutronics . . . 23
3.2.2 Thermal-hydraulics: Kharon . . . 24
3.2.3 Fuel behaviour: SuperFINIX and FINIX . . . 25
3.2.4 Coupling manager: Cerberus/Cetus . . . 26
3.3 Workflow . . . 28

4 Group Constant Generation 29
4.1 The Polynomial Library . . . 29
4.2 Methodology and Spatial Discretization . . . 30
4.3 Fuel assembly homogenization . . . 32
4.3.1 Serpent Setup . . . 32
4.3.2 Burnup and Historical Conditions . . . 33
4.3.3 Instantaneous Variations and Branching Matrix . . . 34
4.3.4 Discontinuity Factors and Form Functions . . . 35
4.4 Reflector Homogenization . . . 35
4.4.1 Radial Reflector . . . 35
4.4.2 Axial Reflector . . . 36
4.5 Infinite-Lattice Comparison . . . 36
4.5.1 Isotopic inventory and burnup step sensitivity . . . 39

5 Multiphysics Coupling 41
5.1 Standalone neutronics simulation . . . 41
5.1.1 Equilibrium Cycle Search . . . 42
5.1.2 Code Verification at Equilibrium . . . 43
5.1.3 Standalone Model Characteristics . . . 45
5.2 Neutronics and thermal-hydraulics . . . 47
5.2.1 Thermal-Hydraulics model . . . 47
5.2.2 Results of neutronics and thermal-hydraulics coupling . . . 48
5.3 Neutronics, themal-hydraulics and fuel behaviour . . . 51
5.3.1 Fuel behaviour model . . . 52

5.3.2 Results of neutronics, thermal-hydraulics and fuel behaviour coupling 52

6 Uncertainty quantification 57

6.1 UQ Results 59

7 Conclusion 63

7.1 Key Findings 63

7.2 Future Work 64

A Material compositions 65

B Evolution of Neutron Poisons 67

C Sensitivity of the thermal-hydraulic model 69

D Comparison with NuScale FSAR: Relative Assembly Power Distribution 71

E Sensitivity of fuel behaviour to gadolinium homogenization 73

Bibliography 75

List of Tables

3.1 NuScale system design information [25, 26]. 18

3.2 NuScale core design parameters [41]. 18

3.3 Axial positions of spacer grids [41]. 21

4.1 Node-averaged parameters present in the polynomial library. 30

4.2 Depletion calculation conditions. 34

4.3 Branch conditions for cross-section generation. 34

4.4 Comparison of infinite multiplication factor k_∞ computed with Serpent and Ants at nominal conditions and burnup 0.0 MWd/kgU. 37

5.1 Axial mesh discretization and node heights for the whole-core Ants model. 42

5.2 Reactivity parameters and coefficients. 46

6.1 The Uncertain Parameters and their Statistical Information. 58

6.2 Sample standard deviation of the critical boron concentration [ppm] as a function of burnup, for each uncertainty propagation case. 60

6.3 Comparison between the standard deviations obtained from the independent perturbation simulations and the standard deviation obtained from the simultaneous perturbation case. 62

A.1 Nuclide compositions of all fuel types [atoms/barn-cm]. 65

A.2 Volume fractions of the homogeneous mixtures [41]. 65

A.3 Nuclide compositions of structural materials, control rod absorber material, and fill gas. Number densities are given in units of 1/(barn·cm) [41]. 66

C.1 Sensitivity of the pressure drop to the axial dimension treatment. . . 69

List of Figures

2.1 Scheme of the Generalized Equivalence Theory for two-step procedures 10

3.1 Axial structure of fuel rod and control rod (not to scale); all dimensions are in cm. 19

3.2 Radial section of the fuel rod [41]. 19

3.3 Radial section of the guide tube + control rod [41]. 20

3.4 Comparison of fuel pin layouts between the assembly with and without gadolinium fuel pins. 20

3.5 Spacer grid model [41] 21

3.6 Core loading pattern with assembly batch legend. 22

3.7 The Kraken computation framework [18] 23

3.8 Representative multiphysics coupling mechanisms in nuclear reactors 27

3.9 Workflow followed for the development of the multiphysics model. . . 28

4.1 Representative axial discretization for group constant homogenization (not to scale). 31

4.2 Representative radial discretization for group constant homogenization. 31

4.3 Workflow for the generation of the polynomial library [52]. 32

4.4 Convergence of the Shannon entropy and the eigenvalue over the initial cycles. 33

4.5 Comparison of infinite multiplication factor k_∞ computed with Serpent and Ants at nominal conditions for fuel UOX. 37

4.6 Comparison of infinite multiplication factor k_∞ computed with Serpent and Ants at nominal conditions for the fuel blanket. 38

4.7 Plutonium-239 concentration: comparison between Serpent and Ants. 39

4.8 Comparison of infinite multiplication factor k_∞ with 28 and 52 burnup steps in the upper blanket. 40

5.1 Axial structure of fuel rod (not to scale), all dimensions are in cm. . . 42

5.2 Critical boron concentration over nine fuel cycles: comparison between Ants and Serpent. 43

5.3 Equilibrium cycle convergence (cycles 6–9). Critical boron concentration (solid lines, left axis) and absolute difference between consecutive cycles (scatter markers, right axis). 43

5.4 Critical boron concentration at the equilibrium cycle: comparison between Ants and Serpent. 44

5.5 Comparison of radial power distributions at BOC and EOC. The left column shows the normalized assembly power calculated by Ants, while the right column shows the relativ difference compared to the Serpent reference. 44

5.6 Average axial power distribution at BOC and EOC. 45

5.7 Burnup maps at BOC and EOC. 46

5.8 Average coolant temperature and average temperature difference between inlet and outlet at equilibrium cycle. 48

5.9 Radial coolant temperature distribution at equilibrium cycle at assembly level. 49

5.10 Axial power and coolant distribution at equilibrium cycle at the beginning and end of the cycle. 50

5.11 Critical boron concentration at equilibrium cycle: comparison between standalone N and coupled N+TH calculations. 50

5.12 Assembly power relative difference (%) between N+TH and N, at BOC (left) and EOC (right). 51

5.13 Radial fuel temperature distribution at equilibrium cycle. 52

5.14 Axial power and coolant distribution at equilibrium cycle at the beginning and end of the cycle. 53

5.15 Critical boron concentration comparison at equilibrium cycle. 54

5.16 Assembly power relative difference (%) between N+TH+FB and N, at BOC (left) and EOC (right). 55

6.1 Corner plot of the sampled input parameters for the uncertainty quantification analysis. 58

6.2 Standard deviation convergence at day 695. 59

6.3 Critical boron concentration versus thermal power across the 300 realizations of the power uncertainty propagation case, evaluated at BOC and EOC. 60

6.4 Critical boron concentration at Day 0 versus inlet temperature, flow rate, and outlet pressure, across the 300 realizations of the respective uncertainty propagation cases. 61

6.5 Evaluation of the critical boron concentration and its uncertainty. . . 61

B.1 Evolution of Samarium-149 number density in the upper blanket during depletion. The plot compares the reference Monte Carlo solution (Serpent) against the deterministic nodal solver (Ants) using two different temporal discretizations (28 and 52 burnup steps). The relative difference in the bottom panel is computed as $\frac{\text{Serpent}-\text{ANTS}}{\text{Serpent}}$. . 67

B.2 Evolution of Xenon-135 number density in the upper blanket during depletion. The plot compares the reference Monte Carlo solution (Serpent) against the deterministic nodal solver (Ants) using two different temporal discretizations (28 and 52 burnup steps). The relative difference in the bottom panel is computed as $\frac{\text{Serpent}-\text{ANTS}}{\text{Serpent}}$. . 68

C.1 Comparison of axial coolant density and temperature profile at EOC with different D_h. 70

C.2 Comparison of the average coolant temperature with modified axial dimensions. 70

D.1 Comparison of radial relative power distributions at BOC and EOC with the NuScale FSAR reference. 71

E.1 Max and average fuel temperature comparison. 73

E.2 Max assembly fuel temperature difference. 74

Glossary

ADF

Assembly Discontinuity Factor

BEPU

Best Estimate Plus Uncertainty

BOC

Beginning of cycle

BOS

Beginning of the step

CBC

Critical boron concentration

CFD

Computational Fluid Dynamics

CR

Control rod

CMM

Cumulative Migration Method

DF

Discontinuity Factor

DTC

Doppler temperature coefficien

EOC

End of cycle

EOS

End of the step

FB

Fuel behaviour

FF

Form Function

FSAR

NuScale Final Safety Analysis Report

GET

Generalized Equivalence Theory

GT

Guide tube

LELI

Linear Extrapolation / Linear Interpolation

LWR

Light Water Reactor

MC

Monte Carlo

MTC

Moderator temperature coefficien

MOC

Middle of cycle

N

Neutronics

PWR

Pressurized Water Reactor

RMS

Root mean square

SG

Spacer grid

SMR

Small Modular Reactor

TH

Thermal-hydraulics

TRC

Transport-Correction Method

UOX

Uranium Oxide

UQ

Uncertainty quantification

Chapter 1

Introduction

1.1 Background

Within a nuclear reactor core, physical phenomena occur simultaneously and interact with one another. Multiphysics simulation models these interactions using a single computational framework. Different physical solvers are integrated to capture the overall system behaviour in a consistent and realistic manner [1].

Historically, nuclear reactor and safety system design has relied on separate physics simulations and conservative approaches. Due to computational limits, domains such as neutronics (N), thermal-hydraulics (TH), and fuel behaviour (FB) have been analysed separately. Single-physics calculations can be accurate, but they cannot capture interactions or feedback between physical domains. This decoupled approach requires fixed boundary conditions, so it ignores these interactions. To compensate for this lack of detail, conservative safety margins are applied, leading to less efficient and more expansive systems [2].

Thanks to the continuous growth in computational power, multiphysics simulations have become more feasible and can now be used for high-fidelity reactor analysis [2]. Several studies, such as Ma et al. [3], have shown that multiphysics simulations provide different and more accurate predictions of reactor parameters compared to uncoupled simulations. For example, multiphysics models can predict axial power distribution and critical boron concentration (CBC) more accurately, improving predictions of reactor behaviour.

However, a more realistic model does not remove the uncertainty in its results. From a safety perspective, quantifying this uncertainty is necessary to determine the margins needed for conservative evaluations. Some uncertainties are inherent to the computational model, while others come from the input parameters. Therefore, uncertainty quantification (UQ) is needed to determine the confidence level that can be placed in the model outputs [4]. The Best Estimate Plus Uncertainty (BEPU) approach combines best-estimate predictions with the quantification of their associated uncertainties [5]. This approach is the main focus of this thesis: obtaining best-estimate core parameters and assessing their reliability by quantifying their

uncertainties.

1.2 Objectives and structure of the thesis

The main objective of this thesis is to implement a whole-core multiphysics model of a NuScale-like Small Modular Reactor (SMR) using the Kraken framework. The modelling approach is neutronics-centred, with thermal-hydraulic and fuel behaviour solvers introduced as feedback mechanisms. The main reactor parameter considered is the critical boron concentration letdown curve. A step-by-step coupling approach is adopted, starting from standalone neutronics and progressively introducing thermal-hydraulics and fuel behaviour. This allows the effects of these phenomena on the neutronic behaviour of the core to be assessed.

The thesis starts with a theoretical introduction presented in Chapter 2. Chapter 3 describes the methodology used in this thesis, starting with the reference NuScale-like SMR model, the Kraken framework, and the workflow used to build the multiphysics model. The neutronics model is based on a two-step approach. For this reason, Chapter 4 describes the generation of the group constants and the polynomial library. Moreover, a verification of the cross-section accuracy is performed.

The standalone neutronics model is then depleted to determine the equilibrium cycle using a 3-batch fuel management strategy. Several consecutive cycles are simulated to reach equilibrium conditions. Chapter 5 presents the whole-core simulation results and compares the standalone neutronics model with the progressively coupled multiphysics models. A comparison between whole-core nodal diffusion and Monte Carlo neutronics is also performed.

A preliminary uncertainty quantification analysis, presented in Chapter 6, is performed using random sampling. Four input parameters are considered: core power, coolant flow rate, inlet temperature, and outlet pressure. Their effect on the neutronic response is evaluated to check the reliability of the results. Finally, the conclusions of the thesis are presented in Chapter 7.

1.3 Literature Review

Multiphysics studies can be classified based on the type of reactor considered, the simulation domain, and the physical phenomena included in the analysis. Focusing on Light Water Reactors (LWRs), traditional multiphysics studies rely on coupling subchannel thermal-hydraulics codes with deterministic neutronics solvers. Thanks to their adequate accuracy and low computational cost, these approaches are still used today for whole-core simulations [6, 7]

Higher-fidelity approaches can be obtained by replacing the deterministic neutronics solver with a Monte Carlo (MC) method and the subchannel code with Computational Fluid Dynamics (CFD) [8, 9]. However, the high computational cost of this approach limits its application to smaller domains, such as single fuel pins or fuel

assemblies. Consequently, extending MC-CFD coupling to whole-core simulations remains challenging [10].

A possible compromise between fidelity and computational cost is to combine Monte Carlo neutronics with subchannel thermal-hydraulic solvers. This combines the higher neutronic fidelity of MC methods with the lower computational cost of subchannel solvers, making whole-core simulations feasible. Studies have shown that this type of coupling can be used for whole-core multiphysics applications [11, 12]. In these frameworks, neutronics is the main focus, while the thermal-hydraulic solver provides the necessary feedback, such as moderator density and temperature updates.

In addition to coupling neutronics with thermal-hydraulics, Monte Carlo neutronics can be coupled with fuel behaviour to obtain detailed power distributions and nuclide inventories [13]. Neutronics, thermal-hydraulics, and fuel behaviour can then be coupled together to model local phenomena [8]. Whole-core N-TH-FB coupling has also been studied using Monte Carlo neutronics. For example, Yu et al. [14] performed a pin-by-pin whole-core steady-state analysis. However, the high computational cost of these models usually limits their application to single-pin or local domains, or to whole-core steady-state calculations at a single time point. Other studies have therefore used deterministic neutronics to reduce the computational cost. Park et al. [15] performed whole-core N-TH-FB depletion calculations using deterministic neutronics. This approach makes whole-core N-TH-FB coupling feasible for multi-cycle simulations.

In the context of the BEPU methodology, uncertainty quantification for multiphysics models has gained importance [4]. In a multiphysics model, uncertainties can arise in each coupled solver. In neutronics, nuclear data are a source of uncertainty. Thermal-hydraulic, fuel behaviour, and neutronics models are also affected by uncertainties in manufacturing tolerances and model parameters. In addition, the boundary conditions used by each solver can also contribute to the overall uncertainty. For example, in a thermal-hydraulic model, using a fixed heat flux or power distribution as a boundary condition can introduce uncertainty in the results [15]. Most UQ studies have focused on specific sources of uncertainty, mainly nuclear data, manufacturing tolerances, and thermal-hydraulic input parameters. However, UQ for multiphysics simulations is still limited. Park et al. [15] showed that nuclear data uncertainties dominate the overall uncertainty of global neutronic parameters.

These multiphysics and uncertainty quantification methods are particularly relevant for the new generation of nuclear power plants, such as Small Modular Reactors. For designs such as the NuScale reactor, neutronic thermal-hydraulic coupling is important due to the interaction between reactor physics and passive cooling. Kakaei et al. [6] studied the coupled neutronic and thermal-hydraulics behaviour of a NuScale core, showing the interaction between natural circulation flow rates, temperature distributions, and reactivity feedbacks.

Modern computational frameworks have been developed to perform these coupled simulations. Examples include MOOSE [16] and VERA [17], which provide tools for multiphysics simulations in nuclear applications. Kraken [18] is another framework developed for this purpose. In this work, Kraken is selected because it is freely

available and can be coupled with the Monte Carlo code Serpent [19]. Although fully coupled multiphysics studies have already been conducted using Kraken, they have primarily focused on the verification and validation of the codes against large-scale reactor data. For instance, Valtavirta and Rintala [20] evaluated the performance of Kraken using the VVER-1000 X2 benchmark and verified the boron letdown curves and power distributions. Because Kraken is a relatively new framework, independent studies extending its application are still limited. Extending these approaches to an SMR, including whole-core N-TH-FB coupling and UQ analysis, would represent a useful next step in multiphysics simulations.

Chapter 2

Theoretical Background

This chapter presents the theoretical background for the multiphysics simulations performed in this thesis. The discussion begins by introducing concepts of neutron transport and fission physics. Next, an overview of the main computational methods used in reactor physics, both stochastic and deterministic, is provided. This is followed by a description of the two-step calculation approach. Furthermore, the theoretical principles of fuel burnup and isotopic depletion are presented to describe the reactor changes over the operational cycle. Finally, the basic principles of thermal-hydraulics and thermomechanics, which are the basis of the solvers used in this work, are briefly presented.

2.1 Neutronics

$$\begin{aligned}\hat{\Omega}\cdot\nabla\phi(\mathbf{r},E,\hat{\Omega})+\Sigma_t(\mathbf{r},E)\phi(\mathbf{r},E,\hat{\Omega}) = \\ = \int dE' \oint d\hat{\Omega}'\Sigma_s(\mathbf{r},E')f_s(\mathbf{r},E'\to E,\hat{\Omega}'\cdot\hat{\Omega})\phi(\mathbf{r},E',\hat{\Omega}')+ \\ + \frac{1}{k}\frac{\chi(\mathbf{r},E)}{4\pi}\int dE' \oint d\hat{\Omega}'\nu(\mathbf{r},E')\Sigma_f(\mathbf{r},E')\phi(\mathbf{r},E',\hat{\Omega}'). \quad (2.1)\end{aligned}$$

Equation 2.1 represents the neutron transport equation for steady-state conditions [21]. The equation expresses a balance between neutron losses and sources in a specific control volume with position $\mathbf{r}$, direction $\hat{\Omega}$, and energy E. The left-hand side of the equation represents the loss of neutrons from the phase-space element:

- Streaming term ($\hat{\Omega}\cdot\nabla\phi$): represents the neutron streaming in phase space (i.e., neutron leakage) out of the physical volume. Here, $\phi(\mathbf{r},E,\hat{\Omega})$ denotes the angular neutron flux.
- Collision term ($\Sigma_t\phi$): describes the removal of neutrons due to absorption and scattering into different energies or directions. Here, Σ_t is the macroscopic total cross section.

The right-hand side includes source contributions:

- In-scattering source (first integral): represents neutrons at position $\mathbf{r}$, with energy E' and direction $\hat{\Omega}'$, that are scattered into the control volume with energy E and direction $\hat{\Omega}$. Here, Σ_s is the macroscopic scattering cross section, while f_s is the scattering transfer probability function.
- Fission source (second integral): describes the production of neutrons through fission. Here, ν is the average number of neutrons emitted per fission, Σ_f is the macroscopic fission cross section, and $\chi(\mathbf{r}, E)$ is the fission neutron energy distribution function (fission spectrum).

To find a non-trivial steady-state solution, an eigenvalue k is introduced into the fission term. This eigenvalue, known as the effective multiplication factor (k_{eff}), quantifies the balance between neutron production and losses. Depending on the value of k_{eff}, the reactor can be subcritical ($k_{eff} < 1$), critical ($k_{eff} = 1$) or supercritical ($k_{eff} > 1$) [21].

It is important to distinguish between the infinite multiplication factor, k_∞, and the effective multiplication factor, k_{eff}. The infinite multiplication factor characterizes an idealized infinite medium in which neutron leakage is neglected. Consequently, it depends only on the material composition and the nuclear cross sections. In contrast, the effective multiplication factor also accounts for neutron leakage and is defined by the balance between neutron production through fission and neutron losses due to absorption and leakage.

2.1.1 Computational Methods in Reactor Physics

The 3-D Boltzmann transport equation (Eq. 2.1) can not be solved analytically without any approximation. Therefore, numerical methods must be employed. These methods can be divided into two categories: stochastic and deterministic approaches.

Stochastic Methods

Monte Carlo codes solve the neutron transport problem by simulating the life history of individual neutrons. Each neutron is tracked from birth until it is absorbed or leaks out of the system. The distance to the next collision, the interaction type, and the neutron energy and direction after each collision are determined by randomly sampling probability distributions derived from evaluated nuclear data libraries. During these simulations, quantities of interest are accumulated to estimate the average behaviour of the neutron population and calculate reactor physics parameters [22].

The main advantage of the Monte Carlo approach is its high fidelity. This method can model the reactor geometry without geometric approximations, use continuous-energy nuclear data, and preserve continuous angular dependence without angular discretization. For this reason, Monte Carlo simulations are considered the reference approach in reactor physics. However, their main drawback is the computational cost. Since Monte Carlo methods rely on random sampling, the standard deviation of an output is proportional to $1/\sqrt{N}$, where N is the number of simulated neutron histories. Therefore, reducing statistical uncertainty requires increasing the number of particle histories, leading to higher computational costs.

Deterministic Methods & Diffusion Theory

In deterministic methods, the phase space is discretized in energy (using multigroup theory), angle (using Spherical Harmonics P_N or Discrete Ordinates S_N approximation), and space [21]. Starting from the Boltzmann transport (Eq. 2.1), the continuous energy is discretized using the multigroup approximation. Assuming isotropic scattering, the equation is then integrated over all solid angles, giving the zeroth-order angular moment and the corresponding neutron balance equation for a generic energy group g [21]:

$$\nabla \cdot \mathbf{J}_g(\mathbf{r}) + \Sigma_{tg}(\mathbf{r})\Phi_g(\mathbf{r}) = \sum_{g'=1}^{G} \Sigma_{s,gg'}(\mathbf{r})\Phi_{g'}(\mathbf{r}) + \frac{1}{k}\chi_g(\mathbf{r}) \sum_{g'=1}^{G} \nu(\mathbf{r})\Sigma_{f,g'}(\mathbf{r})\Phi_{g'}(\mathbf{r}) \quad (2.2)$$

where $\Sigma_{s,gg'}(\mathbf{r})$ represents the group-to-group scattering cross section. $\mathbf{J}_g(\mathbf{r})$ represents the net current of energy group g, $\Phi_g(\mathbf{r})$ is the scalar flux of group g:

$$\mathbf{J}_g(\mathbf{r}) = \int d\hat{\Omega}\, \hat{\Omega}\, \phi_g(\mathbf{r}, \hat{\Omega}), \quad (2.3)$$

$$\Phi_g(\mathbf{r}) = \int d\hat{\Omega}\, \phi_g(\mathbf{r}, \hat{\Omega}). \quad (2.4)$$

Deterministic solvers employ the Neutron Diffusion Theory [21]. Diffusion theory assumes that neutrons diffuse from regions of high concentration to regions of low concentration. This physical approximation, known as Fick's Law, is valid only under specific hypotheses [23]:

- The medium is uniform, weakly absorbing, and scattering is assumed to be isotropic.
- The neutron flux is slowly varying with respect to position. This implies that the domain must be far from localized neutron sources and strong absorbers.

Mathematically, the diffusion approximation can be derived by applying the P_1 approximation to the angular dependence of the neutron transport equation. The zeroth-order angular moment ($n = 0$) leads to the neutron balance equation (Eq. 2.2), whereas the first-order angular moment ($n = 1$) provides a relationship between the neutron current and the neutron flux gradient:

$$\frac{1}{3}\nabla\Phi_g(\mathbf{r}) + \Sigma_{tr,g}(\mathbf{r})\mathbf{J}_g(\mathbf{r}) = 0 \quad (2.5)$$

where $\Sigma_{tr,g}$ is the macroscopic transport cross section, which accounts for the effects of anisotropic scattering through the transport correction. Rearranging Equation 2.5 gives the mathematical form of Fick's law:

$$\mathbf{J}_g(\mathbf{r}) = -D_g(\mathbf{r})\nabla\Phi_g(\mathbf{r}). \quad (2.6)$$

The multigroup diffusion coefficient D_g is defined as:

$$D_g(\mathbf{r}) = \frac{1}{3\Sigma_{tr,g}(\mathbf{r})}. \quad (2.7)$$

Finally, by substituting Fick's law (Eq. 2.6) into the multigroup neutron balance equation (Eq. 2.2), the multigroup neutron diffusion equation is obtained:

$$-\nabla \cdot (D_g(\mathbf{r})\nabla\Phi_g(\mathbf{r})) + \Sigma_{t,g}(\mathbf{r})\Phi_g(\mathbf{r}) = S_g(\mathbf{r}) \tag{2.8}$$

where $S_g(\mathbf{r})$ represents the total source term appearing on the right-hand side of Equation 2.2, including both scattering and fission contributions. Equation 2.8 represents the mathematical formulation adopted by deterministic reactor physics codes.

2.1.2 The Two-Step Calculation Approach

Applying the diffusion equation directly to the entire reactor core is not feasible because of its spatial heterogeneity. A core is typically divided into fuel assemblies, each composed of multiple fuel pins, structural materials, and coolant channels. Deterministic codes require a spatial homogenization and energy condensation procedure. For this reason, the two-step approach is used. This method divides a single whole-core reactor simulation into two separate steps:

- Lattice Calculation: in the first step, the neutron transport equation is solved over a restricted domain, typically a single 2D fuel assembly. Infinite lattice conditions (e.g., reflective boundary conditions) are applied. At this level, the exact heterogeneous geometry is modeled, utilizing either continuous-energy nuclear data or a very fine energy group structure. In this thesis, a Monte Carlo code is used. The objective of the first step is to obtain the flux distribution $\phi(\mathbf{r}, E)$. This flux is then used as a weighting function to perform spatial homogenization and energy condensation, generating the equivalent few macroscopic group constants required for the core simulation.
- Core Calculation: In the second step, a whole-core diffusion calculation is performed. To make this computationally feasible, the detailed heterogeneous geometry is replaced by a coarse spatial mesh of homogeneous nodes. The material properties of each node are defined by the equivalent few-group cross-sections generated during the lattice calculation. The multi-group neutron diffusion equation approximates the transport equation, and the energy dependence is condensed into a structure that typically consists of two macroscopic groups (fast and thermal) for LWRs.

Spatial Homogenization and Energy Condensation

The transition from the heterogeneous lattice calculation to the equivalent homogeneous nodal model requires the preservation of the volume-integrated reaction rates and the surface-averaged net currents [24]. To preserve reaction rates, the homogenized macroscopic cross-section $\hat{\Sigma}^i_{x,g}$ for reaction type x and energy group g in node V_i is defined as [25]:

$$\hat{\Sigma}^i_{x,g} = \frac{\int_{V_i}\int_{E_g} \Sigma_x(\mathbf{r}, E)\,\phi(\mathbf{r}, E)\,\mathrm{d}E\,\mathrm{d}V}{\int_{V_i}\int_{E_g} \phi(\mathbf{r}, E)\,\mathrm{d}E\,\mathrm{d}V}. \tag{2.9}$$

Similarly, the homogenized model must preserve the net neutron current across each nodal interface S_i^k:

$$\int_{S_i^k} \hat{\mathbf{J}}_g(\mathbf{r}) \cdot d\mathbf{S} = \int_{S_i^k} \mathbf{J}_g(\mathbf{r}) \cdot d\mathbf{S} \tag{2.10}$$

where the hat notation denotes the homogenized variables. To satisfy this constraint, Fick's law (Eq. 2.6) must be recalled. By substituting the diffusion approximation into Equation 2.10, the equivalent homogenized diffusion coefficient $\hat{D}_g^i$ for node i is defined as:

$$\hat{D}_g^i \equiv \frac{-\int_{S_i^k} \mathbf{J}_g(\mathbf{r}) \cdot d\mathbf{S}}{\int_{S_i^k} \nabla \hat{\Phi}_g(\mathbf{r}) \cdot d\mathbf{S}} \tag{2.11}$$

To preserve the correct reaction rates, the homogenized flux must have a specific average value inside the node. To preserve the exact neutron leakage across the boundary, it must also have a specific gradient at the interface. Because the homogenized node uses spatially constant parameters, a smooth flux shape that satisfies both the correct average value and the correct boundary gradient will have a surface value that differs from the true heterogeneous surface flux. As a result, two adjacent nodes will have two different homogeneous surface fluxes at their shared interface. Diffusion solvers force the surface flux to be continuous across nodes. However, enforcing this continuity mathematically compromises the preservation of currents and reaction rates [24].

To overcome this limitation, additional degrees of freedom must be introduced. This is the main idea behind the Generalized Equivalence Theory (GET) [24]. Instead of enforcing the continuity of the homogenized surface flux between adjacent nodes, GET allows the surface flux to be discontinuous while preserving the continuity of the net current. This is achieved by introducing the Discontinuity Factors (DF), defined as the ratio between the exact heterogeneous surface flux and the homogenized surface flux evaluated at the same interface:

$$f_{s,g} = \frac{\phi_{s,g}^{het}}{\phi_{s,g}^{hom}} \tag{2.12}$$

where $\phi_{s,g}^{het}$ is the actual heterogeneous flux at the surface s, while $\phi_{s,g}^{hom}$ is the flux at the surface s obtained from the homogenization.

Although discontinuity factors provide an exact interface correction for a homogenized fuel assembly, they are not practical in the two-step approach. The main goal of this approach is to avoid a whole-core transport calculation. Instead, each reactor region is homogenized independently using single-assembly infinite lattice calculations. However, calculating DFs requires the heterogeneous surface flux at each assembly interface. This can only be obtained from a heterogeneous whole-core calculation. Therefore, calculating DFs would require the same whole-core calculation that the two-step approach is intended to avoid.

Thus, Assembly Discontinuity Factors (ADFs) are introduced. ADFs are calculated by simulating an assembly under the assumption of an infinite lattice. In this

case, the homogenized flux is spatially constant in the assembly, meaning the homogenized surface flux is equal to the assembly-averaged homogenized flux. Since the homogenization preserves the reaction rate, the assembly-averaged homogenized flux is equal to the assembly average heterogeneous flux, so that the ADF can be expressed as:

$$ADF_{s,g} = \frac{\phi_{s,g}^{het}}{\bar{\phi}_{g}^{het}} \tag{2.13}$$

where $\phi_{s,g}^{het}$ is the heterogeneous flux at the surface and $\bar{\phi}_{g}^{het}$ is the assembly average heterogeneous flux. They both come from the infinite lattice calculation.

Figure 2.1 shows the overall two-step procedure. First, a Monte Carlo simulation is performed at the assembly level for homogenization and energy condensation. This provides the cross sections and discontinuity factors. Finally, a diffusion calculation for the whole-core is performed.

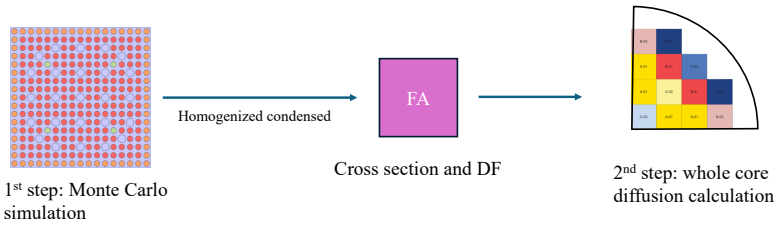


Figure 2.1: Scheme of the Generalized Equivalence Theory for two-step procedures

Leakage Corrections

During spatial homogenization, the Monte Carlo simulation is performed on a single assembly assuming an infinite lattice configuration. However, this simulation is not a critical system, and the neutron spectrum it produces is not suitable for generating cross sections [26]. For this reason, leakage corrections are introduced. After generating homogenized multigroup cross sections from the Monte Carlo simulation, a deterministic solver introduces an artificial leakage term through the material buckling B^2 to enforce $k_{eff} = 1$. This produces a leakage corrected critical spectrum, which is then used to condense the cross sections into the final macro-group structure [27].

To evaluate the leakage term, the diffusion coefficient D is also required. Since D is a diffusion theory parameter, it cannot be directly obtained from the Monte Carlo simulation. The Macroscopic Fundamental Mode method implemented in Serpent allows to approximate the diffusion coefficient with the Cumulative Migration Method (CMM) or the Transport-Correction (TRC) method [27]. Additional information on the theoretical formulation and implementation of these methods can be found in [27, 28].

Limitations of the two-step approach

While the two-step methodology with ADFs improves the accuracy of whole-core diffusion simulations, it still relies on approximations based on the infinite lattice

assumption [24].

In a reactor core, fuel assemblies interact with neighboring assemblies that may have different enrichments and conditions. These differences affect the neutron spectrum at assembly boundaries, so that the spectrum can differ from that obtained with reflective boundary conditions during homogenization. This limitation is important at the core-reflector interface.

Moreover, the homogenized cross sections and discontinuity factors are position-dependent. Still, the two-step approach computes them once under the infinite lattice assumption, without accounting for this dependence on the actual position in the core.

2.1.3 Burnup and Depletion Calculation

Fuel composition changes over time due to fission reactions, neutron captures, and radioactive decay. Depletion calculations are used to track these changes and generate the homogenized cross-sections as a function of burnup

The time evolution of the concentration N_j of a generic nuclide j is described by the Bateman equation [29]:

$$\frac{dN_j}{dt} = \sum_{i \neq j} S_{i \to j} - \lambda_j N_j - \phi \sigma_j N_j \tag{2.14}$$

where the last two terms represent the loss mechanisms of the nuclide j. The term $-\lambda_j N_j$ accounts for the reduction in concentration due to radioactive decay, while the term $-\phi \sigma_j N_j$ describes the depletion caused by neutron-induced transmutation reactions. The first term represents the source contribution and accounts for all the decay, transmutation, and fission reactions from other nuclides that produce the nuclide j. It can be expressed as:

$$S_{i \to j} = \left(\lambda_{i \to j} + \phi \sigma_{i \to j} + \phi \gamma_{i \to j} \sigma_{f,i}\right) N_i, \tag{2.15}$$

where the three contributions represent the production of nuclide j through radioactive decay, neutron-induced transmutation, and fission reactions, respectively [29]. Here, λ_j is the radioactive decay constant, ϕ is the neutron flux, and σ_j is the corresponding reaction cross section. In Serpent, the Bateman equation is solved using the Chebyshev Rational Approximation Method [30].

The neutron transport equation used for cross-section generation is solved under steady-state conditions. However, simulating the evolution of the fuel composition requires coupling the transport and depletion equations. The transport solution provides the neutron flux and reaction rates needed to solve the Bateman equations (Eq. 2.14). The updated isotopic densities then change the neutron spectrum, which in turn changes the reaction rates.

To handle this nonlinear feedback, the burnup evolution is divided into discrete steps. The simplest numerical approach solves the transport equation only at the beginning

of the step (BOS) and assumes constant reaction rates to deplete the fuel up to the end of the step (EOS). Because this assumption neglects continuous spectrum evolution during the interval, it introduces numerical inaccuracies, especially for large burnup steps. To improve the overall accuracy, Predictor-Corrector schemes are employed. The algorithm proceeds in two stages:

1. Predictor: The Bateman equations are solved to obtain a predicted EOS composition, assuming that the BOS reaction rates remain constant throughout the interval.

2. Corrector: A second transport calculation is performed at the EOS using the predicted composition. The final material depletion is then recalculated from BOS to EOS using an average of the BOS and EOS reaction rates.

To further improve accuracy, higher-order algorithms such as the LELI (Linear Extrapolation / Linear Interpolation) method are employed. In the LELI scheme, the constant reaction rate assumption is not used. Instead, it performs a linear extrapolation using the reaction rates computed at the previous burnup step to estimate their continuous evolution. The corrector step then applies linear interpolation between the BOS and the newly computed EOS reaction rates [31].

2.2 Core Thermal-Hydraulics

The behaviour of the coolant flowing through the reactor core is governed by the conservation equations of mass, momentum, and energy. To solve reactor thermal-hydraulics without relying on CFD codes, which discretize and solve the local Navier-Stokes equations, subchannel thermal-hydraulic codes are used. In this approach, the fluid domain is divided into axial and radial control volumes to solve the governing equations. Instead of calculating local fields, TH codes use volume-averaged properties, reducing computational cost.

To model two-phase flow at the macroscopic scale, the local conservation equations for each phase q are averaged in time and space. However, the averaged fields of the two phases are not independent. As a result, the averaging process introduces new unknown terms into the governing equations, which describe the transfer of mass, momentum, and energy between the phases. To mathematically close the problem, closure relations must be introduced. These relations are based on models developed from empirical correlations [32].

Porous medium TH codes represent a specific subcategory of thermal-hydraulics codes. In this approach, the detailed geometry of the reactor core, including fuel pins and spacer grids, is treated as a porous structure. The governing equations are spatially averaged over a representative elementary volume. As a result, the model does not resolve the exact location of the solid structures. Instead, the domain is characterized macroscopically by its porosity (ε), defined as the fluid fraction of the cell volume. This approximation allows simulations at the macroscopic scale, making it suitable for assembly- and core-level analyses. Based on the porous medium formulation, the steady-state, one-dimensional conservation equations for a generic

fluid phase q are modified to include the porosity ε [33].

The mass conservation equation balances the convective mass flux with the volumetric mass transfer rate (γ_{pq}) from phase p to phase q, and any external volumetric sources ($s_{\text{mass},q}$):

$$\nabla \cdot (\varepsilon \alpha_q \rho_q u_q) = \gamma_{pq} + s_{\text{mass},q} \tag{2.16}$$

where α_q, ρ_q, and u_q are the volume fraction, density, and axial velocity of phase q [33].

The momentum conservation equation balances the divergence of the convective momentum with the sum of the forces acting on the fluid:

$$\begin{aligned} \nabla \cdot (\varepsilon \alpha_q \rho_q u_q u_q) = {} & \nabla \cdot (\varepsilon \alpha_q \mu_{\text{eff},q} \nabla u_q) \\ & + \left[\max(\gamma_{pq}, 0)\, u_p - \max(-\gamma_{pq}, 0)\, u_q\right] - \varepsilon \alpha_q \nabla p + \varepsilon \alpha_q \rho_q g \\ & - \frac{1}{2} \varepsilon^3 \alpha_q \rho_q C\, |u_q|\, u_q - k\,(u_q - u_p) + s_{\text{mom},q} \end{aligned} \tag{2.17}$$

where $\mu_{\text{eff},q}$ is the effective viscosity, p is the pressure, and g is the gravitational acceleration. The square bracket represents the momentum transfer associated with phase change. The last three terms account for the flow resistance from solid structures via the inertial loss coefficient C, the interfacial drag characterized by the coefficient k, and any external volumetric momentum source $s_{\text{mom},q}$ [33].

Finally, the steady-state energy balance is formulated in terms of total enthalpy ($h_{0,q}$), defined as the sum of specific enthalpy, kinetic, and potential energy:

$$\begin{aligned} \nabla \cdot (\varepsilon \alpha_q \rho_q h_{0,q} u_q) - \nabla \cdot (\varepsilon \alpha_q \lambda_{\text{eff},q} \nabla T_q) = {} & \left[\max(\gamma_{pq}, 0)\, h_{0,\text{cre}} - \max(-\gamma_{pq}, 0)\, h_{0,\text{des}}\right] \\ & - \nabla \cdot (\varepsilon \alpha_q \mathbf{q}) + \nabla \cdot (\varepsilon \alpha_q \tau \cdot \mathbf{u}_q) + s_{h,q} \end{aligned} \tag{2.18}$$

where $\lambda_{\text{eff},q}$ is the thermal conductivity and T_q is the phase temperature. On the right-hand side, the square bracket accounts for the enthalpy transfer due to phase creation ($h_{0,\text{cre}}$) and destruction ($h_{0,\text{des}}$). The remaining terms represent the surface heat fluxes ($\mathbf{q}$), the work performed by viscous forces (τ), and any external volumetric energy source ($s_{h,q}$), such as direct heat deposition in the coolant from neutrons [33].

2.3 Fuel Thermomechanics

Fuel behaviour is needed to determine the fuel temperature and describe how heat is transferred from the fuel, through the gap, and to the cladding. This process depends on the thermal, mechanical, and material properties of the fuel rod components.

2.3.1 Thermal Behaviour and Heat Transfer

The equation governing the temperature distribution is the heat conduction equation, which, in its most general form in cylindrical coordinates, is given by:

$$C_v(T) \frac{\partial T}{\partial t} = \frac{1}{r} \frac{\partial}{\partial r} \left(\lambda(T) r \frac{\partial T}{\partial r} \right) + \frac{1}{r^2} \frac{\partial}{\partial \theta} \left(\lambda(T) \frac{\partial T}{\partial \theta} \right) + \frac{\partial}{\partial z} \left(\lambda(T) \frac{\partial T}{\partial z} \right) + \dot{q}, \tag{2.19}$$

where C_v is the volumetric heat capacity, λ is the thermal conductivity, T is the temperature, and $\dot{q}$ is the volumetric heat generation rate [34]. The steady-state one-dimensional heat conduction equation, along the radial direction (r) [35], is:

$$\frac{1}{r}\frac{d}{dr}\left(\lambda(T) r \frac{dT}{dr}\right) + \dot{q} = 0. \tag{2.20}$$

Boundary conditions are needed to close the problem. At the centerline of the fuel pellet, a zero heat flux condition is usually applied. At the outer surface of the fuel pellet ($r = R_f$), the heat transfer across the pellet-cladding gap is described through a gap conductance h_{gap}, evaluated as the sum of three heat transfer mechanisms [35]:

$$h_{gap} = h_{cond} + h_{rad} + h_{contact}, \tag{2.21}$$

where h_{cond} is the thermal conduction through the gap gas mixture, h_{rad} accounts for thermal radiation, and $h_{contact}$ represents the solid-to-solid contact heat transfer. The conductive heat flux leaving the pellet, given by Fourier's law, must equal the heat flux transferred across the gap:

$$q(R_f) = -\lambda(T(r)) \left.\frac{\partial T}{\partial r}\right|_{r=R_f} = h_{gap}\left[T(R_f) - T(R_{ci})\right]. \tag{2.22}$$

Assuming the gap has negligible heat capacity, energy conservation implies that the heat flux entering the inner surface of the cladding (R_{ci}) must account for the change in cylindrical surface area between R_f and R_{ci}:

$$q(R_{ci}) = \frac{R_f}{R_{ci}} q(R_f). \tag{2.23}$$

Similarly, at the outer surface of the cladding ($r = R_{co}$), the conductive flux leaving the cladding must equal the convective heat flux removed by the coolant:

$$q(R_{co}) = -\lambda(T(r)) \left.\frac{\partial T}{\partial r}\right|_{r=R_{co}} = h_{cool}\left[T(R_{co}) - T_{cool}\right], \tag{2.24}$$

where h_{cool} is the convective heat transfer coefficient between the cladding outer surface and the bulk coolant temperature T_{cool}.

2.3.2 Mechanical Behaviour

The thermal and mechanical behaviours of a fuel rod are related. The temperature distribution determines the thermal expansion of the materials, which changes the gap width. Since the gap width affects the gap conductance, mechanical deformation also affects heat transfer and, in turn, the temperature. The mechanical behaviour of the fuel rod can be described separately.

The fuel pellet undergoes dimensional changes driven by a combination of thermal, irradiation, and mechanical effects. The dominant driving force is thermal expansion, induced by high temperatures. Furthermore, the radial temperature gradient, with

the centerline being significantly hotter than the surface, generates internal thermal stresses. These stresses cause the pellet to crack. As a result, radial relocation can occur.

The fuel also changes its volume due to irradiation. At the beginning of irradiation, the fuel undergoes densification, where the pores formed during manufacturing gradually disappear, slightly reducing pellet volume. As burnup increases, fuel swelling becomes the main effect. The accumulation of solid and gaseous fission products in the fuel causes the pellet to expand and increases its volume.

The mechanical behaviour of the cladding depends not only on its thermal state but also on the pressure difference between the gas inside the rod and the external coolant pressure. To calculate the stresses generated within the cladding, the thin-wall approximation can be adopted [35]. Under this approximation, stresses, strains, and temperatures are assumed to be uniform across the cladding thickness.

Given the internal gas pressure P_i and the external coolant pressure P_o, the hoop stress σ_θ and the axial stress σ_z can be evaluated as:

$$\sigma_\theta = \frac{R_{ci}P_i - R_{co}P_o}{R_{co} - R_{ci}}, \tag{2.25}$$

$$\sigma_z = \frac{R_{ci}^2P_i - R_{co}^2P_o}{R_{co}^2 - R_{ci}^2}, \tag{2.26}$$

where R_{ci} and R_{co} are the inner and outer radii of the cladding, respectively [35].

2.4 Multiphysics Feedback

Now that the theoretical foundations of the individual physical domains have been described, it is necessary to introduce how they interact.

The main physical fields in a reactor core are coupled. The spatial distribution of the neutron flux determines the fission power generation. This thermal energy is transferred from the fuel pellet, through the cladding, to the coolant, changing the thermodynamic state of the fluid. The thermal variations in the coolant change its density, affecting its moderating capability and thus inducing changes in reactivity and in the power profile [18]. The main feedback mechanisms that require a multiphysics approach in a nuclear reactor, such as in a Pressurized Water Reactor (PWR), are:

- Doppler Effect: As the fuel temperature increases, the thermal agitation of the target nuclei also increases, leading to the broadening of the resonance peaks. This phenomenon, known as Doppler broadening, increases neutron absorption in the resonance regions of non-fissile isotopes, primarily ^{238}U, thereby introducing negative reactivity into the system [36].
- Moderator Density: Assuming nearly constant pressure, as is the case in a steady-state PWR, the coolant temperature and density are closely related [37]. In a water-moderated thermal reactor, an increase in coolant temperature leads to a decrease in coolant density, resulting in fewer hydrogen atoms per

unit volume. This reduces the moderation efficiency. As a consequence, the changes in coolant temperature and density affect the neutron spectrum and, thus, the power distribution and the overall neutron population.

- Fuel thermo-mechanics: Due to irradiation and high operating temperatures, fuel rods undergo changes in their material properties over time. Phenomena such as fuel expansion, fuel swelling, and pellet-cladding contact modify the thermal conductance of the fuel rod, thereby affecting both the fuel temperature and the wall heat flux provided to the coolant.
- Fuel Burnup and Depletion: Burnup introduces a slow, time-dependent effect on reactor behaviour. As irradiation progresses, fissile isotopes are depleted while fission products accumulate. New fissile isotopes, such as plutonium, are produced. This evolution of the isotopic composition alters the macroscopic cross sections, the neutron spectrum, core reactivity, and the spatial power distribution. In addition, burnup degrades the fuel's thermal conductivity and modifies its mechanical properties, further affecting fuel temperature and the reactor's overall thermal response.

Due to these interdependencies, standalone simulations cannot fully capture the reactor behaviour. In a coupled multiphysics framework, neutronics provides the spatial power distribution to the thermal-hydraulics and fuel behaviour solvers. In turn, the fuel behaviour solver provides the fuel temperature for the Doppler feedback, while the thermal-hydraulics solver provides the coolant temperature and density for the moderator feedback. This information exchange allows the coupled model to account for the main feedback mechanisms and provide a more realistic description of reactor core behavior.

Chapter 3

Methodology

This chapter introduces the reactor model and the Kraken computational framework used in this work. It also presents the general workflow used for the multiphysics study.

3.1 Reactor Model

SMRs have attracted interest as a future option for nuclear power generation because of their passive safety features and flexible deployment. Among the SMR designs under development, the NuScale reactor, developed by the US company NuScale Power [38], is selected as the reference model for this study, since a sufficiently detailed public design basis is available [39].

The NuScale Small Modular Reactor is an integral pressurized water reactor that uses light water as both coolant and moderator and operates through natural circulation. Under nominal conditions, the primary coolant system maintains a pressure of ~ 12.8 MPa, with coolant entering the core at ~ 531 K and exiting at ~ 587 K. Table 3.1 reports the main system design parameters.

While current designs specify a thermal output of 250 MWth per module [40], this thesis focuses on the earlier 160 MWth configuration [39]. Consequently, the geometrical and operational specifications presented in this work correspond to the 160 MWth reference design.

It must be noted that, since the NuScale SMR is a commercial design, some specifications are not publicly available. The missing proprietary data include the first fuel cycle configuration, the exact arrangement and composition of the burnable absorber pins, and the specific uranium enrichment of the axial blanket zones. To overcome this limitation and build a computational model, the core parameters are extracted from the publicly available NuScale Final Safety Analysis Report (FSAR) [39]. Missing information is taken from the existing literature. For instance, the fuel assembly layout and material compositions are based on the NuScale-like neutronic benchmark developed by Fridman et al. [41], supplemented by additional core design data from the work by Baker et al. [42].

Table 3.1: NuScale system design information [25, 26].

Parameter	Value	Units
Rated thermal power	160	MWth
Coolant/moderator	Light water	–
Primary circulation	Natural circulation	–
System pressure	12.8	MPa
Core inlet/outlet temperatures	531/587	K
Fuel type	UO_2 pellet	–
Pressure vessel height/radius	17.8/1.5	m
Reactivity control mechanisms	Control rod drive, soluble boron	–
Average cycle burnup	12	MWd/kgU

3.1.1 Core and Fuel Assembly

The reactor pressure vessel is 17.8 meters tall and has a radius of 1.5 meters. The vessel has an inner radius of 122 cm and an outer radius of 137 cm. To reduce neutron leakage, the core is surrounded by a heavy steel neutron reflector with a radius of 93.93 cm, which is itself surrounded by a water reflector with a radius of 99.06 cm [41]. The reactor vessel contains the core, which consists of 37 fuel assemblies containing uranium oxide (UOX) fuel pellets with M5 alloy cladding.

Table 3.2: NuScale core design parameters [41].

Parameter	Value	Units
Number of fuel assemblies	37	–
Fuel assembly layout	Square 17x17 array	–
Fuel pin radius	0.4058	cm
Fuel pin gap radius	0.414	cm
Fuel pin clad radius	0.475	cm
Guide tube internal radius	0.5715	cm
Guide tube external radius	0.6121	cm
Fuel pin pitch	1.2598	cm
Axial blanket enrichment	2.00	wt% ^{235}U
Fuel pin clad material	M5® Zirconium alloy	–
Guide tube clad material	Zircaloy-4	–
Lower/upper axial blanket heights	5.00	cm
Fissile fuel height	190.00	cm
Heavy reflector radius	93.93	cm

The fuel assembly has a typical 17×17 PWR fuel assembly lattice. Each assembly contains 264 fuel pins, 24 guide tubes for control rod insertion, and one central

instrumentation tube. The axial structure and dimensions of the fuel rods, guide tubes (GTs), and control rods (CRs) are presented in Figure 3.1. The CRs are shown only in the fully withdrawn position, as they are kept fixed in this configuration throughout this work.

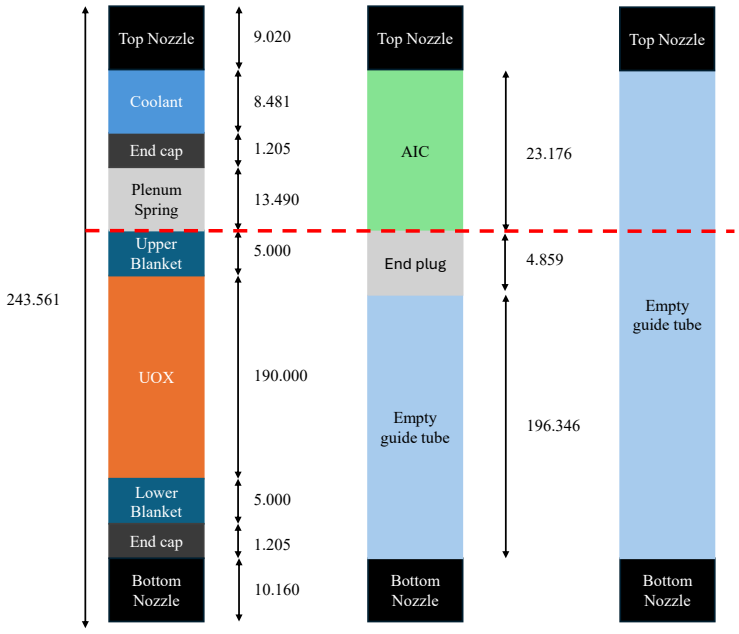


Figure 3.1: Axial structure of fuel rod and control rod (not to scale); all dimensions are in cm.

Figure 3.2 shows the radial geometry of the fuel rod, including the fuel, plenum, and end cap regions. Figure 3.3 shows the corresponding radial view of the guide tube and the control rod inserted into the guide tube.

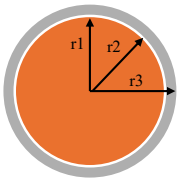
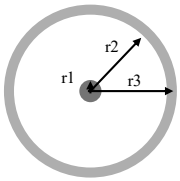
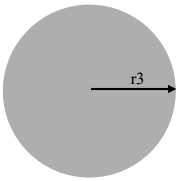
UOX/Blanket		**Fuel plenum + spring**		**Fuel end cap**	
					
Material	**r [cm]**	**Material**	**r [cm]**	**Material**	**r [cm]**
Fuel	0.4058	Inconel	0.0646	-	-
He	0.4140	He	0.4140	-	-
M5	0.4750	M5	0.4750	M5	0.4750

Figure 3.2: Radial section of the fuel rod [41].

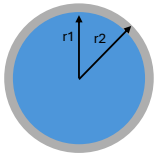
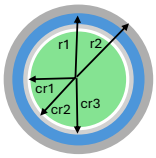
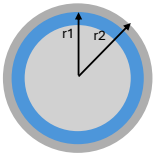
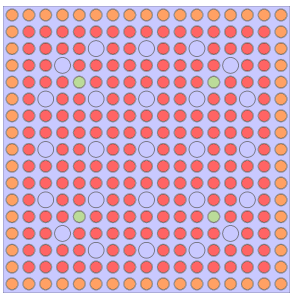
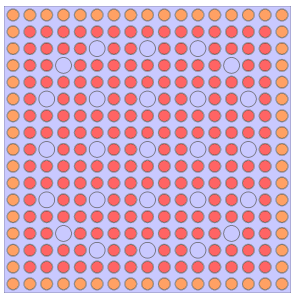
	Empty GT		GT + CR AIC		Fuel end cap	
						
Region	**Material**	**r [cm]**	**Material**	**r [cm]**	**Material**	**r [cm]**
r1	Coolant	0.5715	Coolant	0.5715	Coolant	0.5715
r2	Zr-4	0.6121	Zr-4	0.6121	Zr-4	0.6121
cr1	-	-	AIC	0.4267	-	-
cr2	-	-	He	0.4369	-	-
cr3	-	-	304 SS	0.4839	304 SS	0.4839

Figure 3.3: Radial section of the guide tube + control rod [41].

In the NuScale design, control rods, soluble boron, and burnable absorbers manage reactivity. The control rods, inserted into dedicated guide tubes, are used for start-up and daily operations. They consist of two axial sections of absorbing material: the lower section is made of a silver-indium-cadmium (Ag-In-Cd, AIC) alloy, while the upper section is made of boron carbide (B_4C). To compensate for the slow reactivity loss caused by fuel depletion and the accumulation of fission products, the soluble boron concentration in the primary coolant is adjusted throughout the cycle. Finally, to reduce the excess reactivity, gadolinium oxide (Gd2O3) is utilized as a burnable absorber. It is admixed with the fuel at a concentration of 2 wt% in selected pins of specific assemblies. The effectiveness of burnable absorbers decreases progressively over time, as the absorbing nuclides are transmuted into species with lower neutron capture cross sections [43]. Figure 3.4 illustrates the resulting pin lattice configurations for assemblies with and without gadolinium.



(a) Assembly with Gadolinium.



(b) Assembly without Gadolinium.

- Peripheral fuel pin, 20% lower enrichment
- Standard fuel pin
- Fuel pin with Gd
- Guide tube / instrumentation hole

Figure 3.4: Comparison of fuel pin layouts between the assembly with and without gadolinium fuel pins.

To maintain the structural integrity of the fuel assembly array, the fuel rods and guide

tubes are supported by spacer grids (SGs) located at specific axial elevations. The NuScale fuel assemblies utilize two different types of spacer grids: HTP™ SG made of Zircaloy-4 and HMP™ SG made of Inconel. Table 3.3 reports the axial position of the SGs. Following the NuScale-like benchmark [41], the SGs are accounted for by reducing the water channel width of the unit cell from its nominal value of 1.2598 cm down to 1.2242 cm (Figure 3.5).

Table 3.3: Axial positions of spacer grids [41].

SG	Type	Position	H [cm]
SG5	HTP	Top	223.581
		Bottom	219.136
SG4	HTP	Top	172.527
		Bottom	168.082
SG3	HTP	Top	121.473
		Bottom	117.028
SG2	HTP	Top	70.419
		Bottom	65.974
SG1	HMP	Top	19.365
		Bottom	14.920

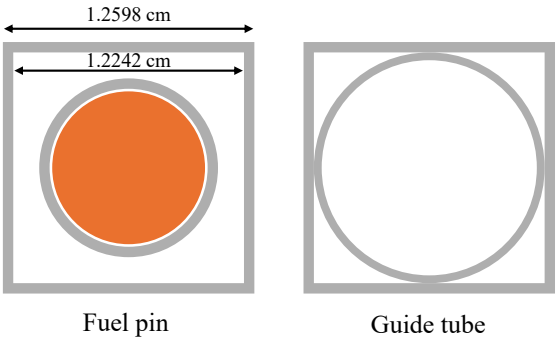


Figure 3.5: Spacer grid model [41]

3.1.2 Core Design

To improve fuel utilization, the reactor employs a 3-batch fuel management strategy. Since the reactor relies on passive cooling through natural circulation, a flat radial power distribution is needed to ensure uniform coolant flow. To flatten this radial power distribution, the core uses three types of fuel assemblies with different initial enrichments of Uranium-235. The assemblies are divided into: Type 01 (4.05 wt% ^{235}U), Type 02 (4.55 wt% ^{235}U with gadolinia pins), and Type 03 (2.60 wt% ^{235}U) [39]. In Type 01 and Type 02 assemblies, the outer fuel pins have an enrichment 20% lower than the inner pins to reduce neutron leakage [42]. Type 03, on the other hand, is a low-enrichment assembly placed at the center of the core to reduce the central power peaking.

The fuel shuffling pattern is designed to achieve this flat radial power distribution. As illustrated in the equilibrium cycle core loading pattern (Fig. 3.6), fresh fuel assemblies (Batch C) are placed in the peripheral region of the core. The once-burnt fuel assemblies (Batch B) are moved to the intermediate region, while the twice-burnt fuel assemblies (Batch A) are placed in the inner region. The central low-enriched assembly (Type 03) is discharged after every cycle.

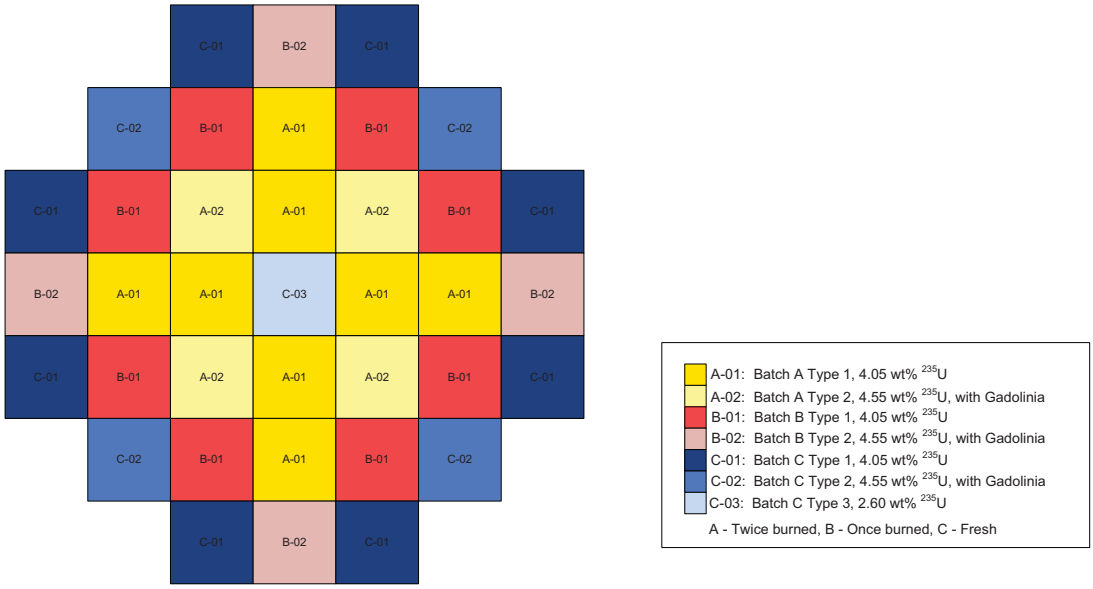


Figure 3.6: Core loading pattern with assembly batch legend.

A single fuel assembly, except the center one, reaches an average burnup of approximately 12 MWd/kgU per operating cycle. Each cycle lasts approximately 695 days, followed by a three-week outage during which refueling and fuel shuffling are performed.

Since the transient cycle information is not reported in the FSAR [39], the equilibrium cycle is obtained computationally. This is achieved by repeatedly simulating whole-core depletion, using the known shuffling pattern and starting with a core entirely composed of fresh fuel, until the equilibrium cycle pattern is reached.

3.2 The Kraken multiphysics framework

The numerical simulations in this work are performed using Kraken [18], a multiphysics reactor analysis framework developed by the VTT Technical Research Centre of Finland [44].

Figure 3.7 illustrates the architecture of the Kraken framework. Cerberus is the centralized driver. It controls solver execution and handles spatial mapping and data transfer between different meshes. Cerberus can couple three main physical domains: neutronics, thermal-hydraulics, and fuel behaviour, as well as plant-level system codes.

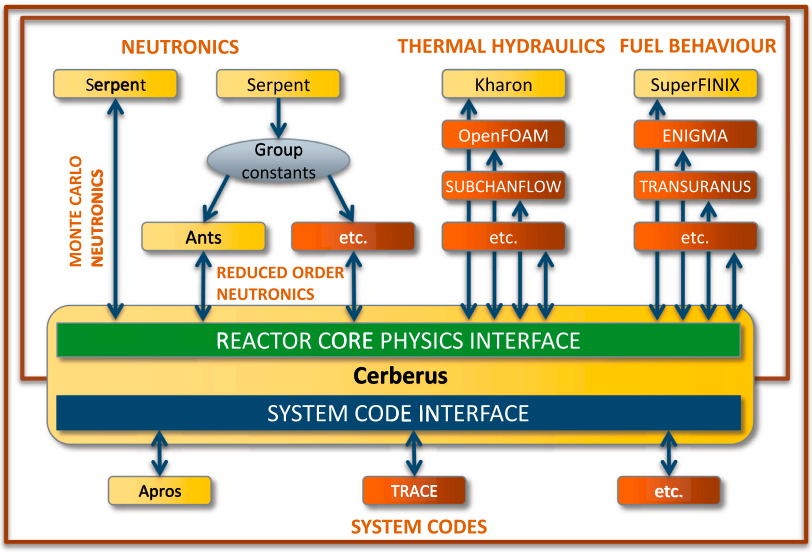


Figure 3.7: The Kraken computation framework [18]

As shown in the diagram, each domain supports several codes. The modules highlighted in yellow represent the native codes included in Kraken (such as Serpent [19], Ants [45], Kharon [18], and SuperFINIX [35]), whereas those in orange represent external third-party codes that can be coupled to the framework [18]. It is important to note that Kraken is code-agnostic. Since Cerberus manages the communication independently of the solvers' internal mechanics, the framework is not limited to the software shown in Figure 3.7, and any suitable code can be integrated.

In this work, the simulations rely on the native Kraken solvers. For neutronics calculations, the two-step approach is used. In the first step, Serpent performs the homogenization calculation, while in the second step, Ants performs the whole-core diffusion calculation, following the scheme shown in Figure 2.1. Kharon models the coolant sub-channel thermal-hydraulic conditions, and SuperFINIX models fuel behavior.

3.2.1 Neutronics

Serpent

Serpent is a Monte Carlo code developed at VTT [18]. Within the Kraken framework, Serpent can be used both as a high-fidelity neutronics solver and to generate homogenized group constants for diffusion calculations [18]. Specifically, Serpent can generate macroscopic cross sections for both infinite and critical spectra. [46].

Ants

Ants [45] is a nodal, multi-group neutron transport code that supports rectangular, hexagonal, and triangular lattice geometries. It can be used for stationary, depletion, and transient calculations [47]. The main approximations are those associated

with deterministic codes, as discussed in Section 2.1.1, and those related to the two-step approach, described in Section 2.1.2. Moreover, Ants currently cannot apply discontinuity factors at fuel-fuel interfaces (e.g. UOX–blanket interfaces) or fuel-non-active interfaces in the axial direction.

The reactor core domain is radially discretized into spatial nodes, with each node corresponding to a single fuel assembly. Under the homogeneous node assumption, the group constants are uniform within each nodal volume. In each region, the multigroup neutron diffusion equation (Eq. 2.8) is solved. Further details on the adopted solution method can be found in [48].

Serpnet generates the group constants and provides them in Ants as external inputs through the group constant library. Ants supports several group constant library formats, including HEXBU-3D/MOD5 (for hexagonal geometries), HEXBU-3D/MOD5-TRAB3D (for rectangular geometries), NEMTAB, Simple, and Polynomial, most of which rely on discrete look-up tables [45]. This work utilizes the Polynomial format. The polynomial approach is chosen because it provides a continuous mathematical representation of the cross-section variations (fuel temperature, coolant temperature, boron concentration). A full description of the polynomial library is provided in the next chapter.

3.2.2 Thermal-hydraulics: Kharon

Kharon is a macroscopic, steady-state monodimensional two-phase thermal-hydraulics solver [44]. As detailed in Section 2.2, the governing conservation equations of mass, momentum, and energy are based on the porous medium approach, which characterizes the fuel assembly macroscopically through its porosity and equivalent diameters without resolving the exact location of the solid structures.

In addition to the porous medium formulation, Kharon relies on the closed-channel approximation. The reactor core is discretized into parallel and independent hydraulic channels. Consequently, the coolant flow is assumed to occur in the axial direction, while lateral mixing between adjacent channels is neglected [18].

The porosity is defined as $\varepsilon = V_f/V_t$, where V_f is the fluid volume and V_t is the total volume of the control volume. Two equivalent diameters are used to characterize the flow channel: the hydraulic diameter $D_h = 4A_f/P_w$, based on the wetted perimeter P_w and used to evaluate the friction pressure drop, and the thermal diameter $D_{th} = 4A_f/P_h$, based on the heated perimeter P_h and used to evaluate the heat transfer coefficient [33].

The interfacial drag coefficient k, the inertial loss coefficient C, and the effective transport coefficients $\mu_{\text{eff},q}$ and $\lambda_{\text{eff},q}$ are evaluated using closure correlations. These correlations depend on D_h, the local flow regime, and the fluid properties. In particular, the frictional pressure drop is calculated using the loss coefficient $C = f/D_h$, where the friction factor f is obtained from a correlation suitable for the flow regime. Similarly, the convective heat transfer coefficient used to calculate the wall-to-coolant heat flux is obtained from a Nusselt-number correlation based on D_{th} [33].

Modelling Assumptions

The Kharon model adopted in this work relies on the following assumptions:

- Closed-channel formulation: each coolant channel is modelled independently, with no cross-flow (mass, momentum, or energy exchange) between adjacent channels.
- No form losses: pressure losses due to localized obstructions (e.g. spacer grids) are not modelled. Only distributed friction, through the loss coefficient $C = f/D_h$, is accounted for.
- Enthalpy-based diffusion: the diffusive term in the energy equation is expressed in terms of the enthalpy gradient rather than the temperature gradient; this approximation is only accurate for small enthalpy differences across the domain [33].

3.2.3 Fuel behaviour: SuperFINIX and FINIX

While FINIX is a standalone fuel performance code designed to solve the thermo-mechanical behaviour of a single fuel rod, SuperFINIX extends its application to core-level fuel behaviour simulations [18]. SuperFINIX runs multiple FINIX simulations to represent the entire reactor core [44].

SuperFINIX allows two approaches for modelling the fuel assembly geometry. A single rod type can represent the average thermal-mechanical behaviour of several equivalent fuel pins. Alternatively, different rod types can be assigned to individual pins to account for differences between pins, such as those caused by burnable absorbers like gadolinium.

Physical Scope and Solution Algorithm

The thermo-mechanical behavior of a fuel rod under irradiation is a coupled multi-physics problem. To capture this, FINIX continuously updates the material properties and tracks irradiation-induced phenomena. For instance, the thermal conductivity of the UO_2 fuel pellets is modeled as a function of local temperature, burnup, theoretical density, and the presence of burnable poisons (e.g., Gadolinia, Gd_2O_3). Furthermore, FINIX uses a fission gas release model to describe the production of fission gases (xenon and krypton) and their release into the gap. This reduces the gap thermal conductance and increases the internal rod pressure.

To resolve the feedback loop between thermal expansion, gap conductance, and temperature, FINIX divides the mathematical problem into two coupled domains solved via an iterative procedure. As detailed in Section 2.2, the thermal model evaluates the radial temperature profile by implementing the 1D radial steady-state heat conduction equation (Eq. 2.20) for each axial slice. The mechanical response couples all axial nodes through the internal gas pressure, which is calculated using the ideal gas law and the total free volume of the rod.

An outer solver loop is used to update the fuel and cladding thermal properties, the

heat conduction equation, and the plenum temperature, using the gap conductance as the convergence criterion. Within this loop, an inner mechanical loop calculates the internal pressure and the structural deformations.

Simplifying Assumptions and Limitations

FINIX is based on a cylindrical coordinate system (r, θ, z). The code relies on a few fundamental assumptions [35]:

- 1.5D Geometry: The heat conduction equation is one-dimensional and depends only on the radial coordinate. The axial coordinate is taken into account by solving the heat equation independently for each axial layer. As a result, no heat is transferred between adjacent axial layers. This assumption is valid when the axial heat transfer is negligible compared with the radial heat transfer and when the boundary conditions and the power distribution are axisymmetric. However, the mechanical model couples the axial slices globally through the internal gas pressure.
- Rigid Pellet Approximation: The fuel pellet is assumed to have an infinite elastic modulus and therefore does not deform under mechanical loading. Its dimensions only change due to thermal expansion, densification, and fuel swelling. In addition, the pellet is assumed to have a perfect cylindrical geometry. Consequently, this prevents the resolution of complex pellet-cladding mechanical interactions. For this reason, FINIX is not intended to model severe accident phenomena. Processes such as cladding ballooning, high-temperature creep, and cladding rupture cannot be modelled.
- Cladding Shell Approximation: The cladding is modeled as a cylindrical shell for which the radial variations in stress, strain, and temperature across the cladding thickness are assumed to be small and therefore constant.

3.2.4 Coupling manager: Cerberus/Cetus

The Kraken framework is based on a modular architecture, in which the different solvers exchange information with one another. The simulation starts from a set of initial conditions, such as the coolant temperature. The coupled calculation follows a Picard iteration scheme. First, the neutronics problem is solved using the initial boundary conditions. Once converged, the results are passed to the thermal-hydraulics solver as input. The converged thermal-hydraulic results are then passed to the fuel behaviour solver. The process is then repeated until global convergence is reached.

To automate this computational process and manage the user-defined inputs, Kraken relies on Cetus. Through Cetus, it is possible to define specific boundary conditions, numerical schemes, and coupling parameters for the calculation. For the simulations performed in this work, the following configurations are adopted:

- Simulation type: A criticality search based on the soluble boron concentration is performed. At each depletion step, the solver iteratively adjusts the boron

concentration to maintain criticality ($k_{\text{eff}} = 1$). It should be highlighted that this result is achieved entirely through boron letdown, without any control rod movement.

- Time integration and depletion: Macroscopic burnup steps are defined to simulate the NuScale equilibrium cycle. To evaluate the evolution of the core, the depletion calculation is performed using the linear predictor-linear corrector method.
- Equilibrium models for short-lived poisons: Rather than relying on the depletion solver for the explicit tracking of short-lived neutron poisons (Xenon-135 and Samarium-149), an equilibrium model is used. Using the equilibrium model for these isotopes yields more reliable and stable results than explicit tracking during coupled multi-physics calculations [49].
- Doppler temperature definition: In SuperFINIX, the fuel temperature provided to the neutronics solver for Doppler effect calculations is defined as an effective temperature. It is calculated as a weighted combination of 70% of the pellet surface temperature and 30% of the pellet centerline temperature.
- Numerical stability: Under-relaxation factors are applied to the thermal-hydraulic output from Kharon to prevent excessive oscillations of fluid density and temperature between coupling iterations, thereby ensuring numerical stability.
- Spatial data mapping: Depending on the geometrical resolution of the computational domains, Cetus handles data interpolation. When the meshes of two solvers are identical, a direct one-to-one mapping is performed. If the spatial resolutions differ, Cetus uses volume averaging techniques to distribute or aggregate values while preserving integral quantities.

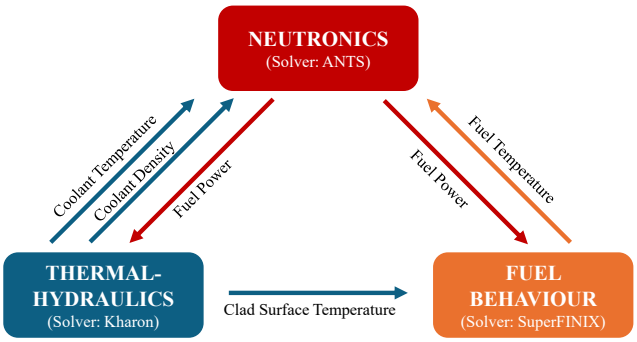


Figure 3.8: Representative multiphysics coupling mechanisms in nuclear reactors

Figure 3.8 shows the physical parameters exchanged between the different solvers and specified in Cetus. Ants provides the spatial power distribution to both Kharon and SuperFINIX. In return, Kharon feeds moderator conditions (coolant density and temperature) back to Ants and clad surface temperature to SuperFINIX. Finally, SuperFINIX evaluates the effective fuel temperature and returns it to Ants. If one of

the solvers is not included in the simulation, boundary conditions must be imposed in Cetus.

3.3 Workflow

The development of the multiphysics model for the NuScale-like core requires a multi-step approach. As shown in Figure 3.9, the idea is to start with the implementation of the neutronics model. To build the neutronics model in Ants, the two-step procedure must be followed. First, the group constants must be generated using Serpent; after that, the standalone simulation can be performed. Subsequently, the thermal-hydraulic model and, finally, the fuel behaviour model are added to the neutronics model. The resulting multiphysics model is then used to perform coupled simulations and assess the effects of the coupling between the different physics.

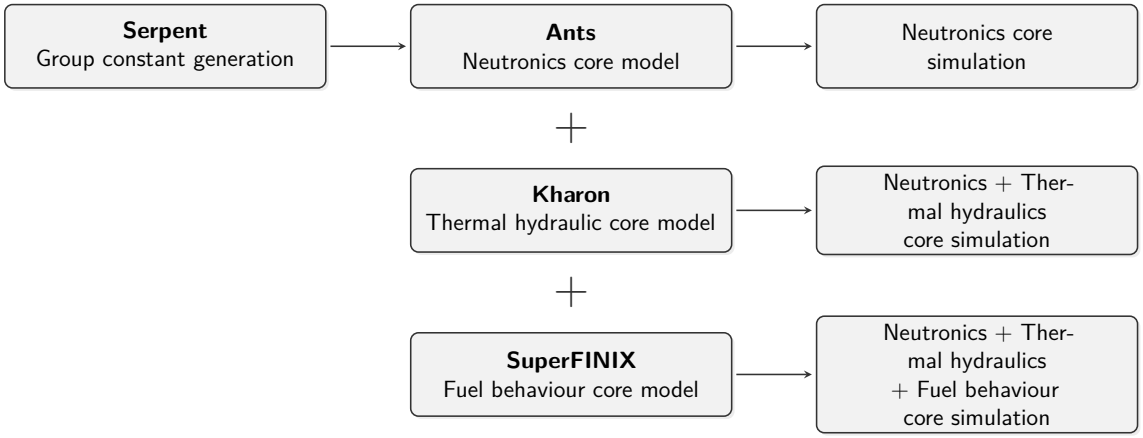


Figure 3.9: Workflow followed for the development of the multiphysics model.

It is important to emphasize that this multiphysics study is primarily neutronics-oriented. The additional thermal-hydraulic and fuel behaviour solvers are regarded as supporting models that provide the neutronics solver with the necessary information to obtain more accurate results. In particular, the primary quantity of interest considered in the multiphysics coupling is the neutronics parameter known as the critical boron concentration, which represents the amount of boron required to maintain the reactor in a critical state.

Chapter 4

Group Constant Generation

Following the methodology described in Section 3.3, this chapter presents the procedure for group constant homogenization. A verification of the generated libraries is also performed by comparing Serpent and Ants results for infinite lattice calculations.

4.1 The Polynomial Library

The final goal is to generate the polynomial library needed by Ants. The library provides group constants over a range of conditions consistent with the reactor operating conditions being simulated. It defines the homogenized parameters as a function of fuel burnup, instantaneous feedbacks, and spectral history for each homogenized region [50]. The library handles these dependencies in different ways:

- burnup dependence is handled through tabulation;
- the dependence on instantaneous conditions is modelled using a polynomial fit around the nominal operating point;
- the dependence on historical conditions is modelled using a plutonium history fit.

At any burnup point, the total macroscopic cross-section Σ is evaluated as the sum of a nominal reference value Σ_{nom}, obtained from a Serpent calculation at the reference operating conditions, and a deviation with respect to that nominal value:

$$\Sigma(\text{fb}) = \Sigma_{\text{nom}} + \Delta\Sigma(\text{fb}). \tag{4.1}$$

where $\Delta\Sigma$ represents deviations from the reference point. The instantaneous variation is represented by a polynomial fit that can account for fuel Doppler feedback, coolant density, and boron concentration:

$$\Delta\Sigma = c_1\Delta\sqrt{T_{\text{fuel}}}+c_2\left(\Delta\sqrt{T_{\text{fuel}}}\right)^2+c_3\Delta\rho_{\text{cool}}+c_4\left(\Delta\rho_{\text{cool}}\right)^2+c_5\Delta C_B+c_6\left(\Delta C_B\right)^2. \tag{4.2}$$

In addition to instantaneous variations, the operational history affects the isotopic composition of the fuel due to spectral shifts. Two nodes containing the same fuel

material but located at different core positions can have different isotopic compositions and group constants because they have experienced different neutron spectra during depletion. To account for this, a plutonium history fit uses the ^{239}Pu atomic density to describe the depletion conditions [51]. A correction factor k relates the cross section to the local ^{239}Pu atomic density:

$$k = \frac{\Sigma_{\text{off}}/\Sigma_{\text{nom}} - 1}{\sqrt{N_{\text{off}}/N_{\text{nom}}} - 1} \tag{4.3}$$

where Σ and N represent the group constant and the ^{239}Pu atomic density, evaluated respectively under nominal (nom) and off-nominal spectral (off) depletion conditions [51]. During the nodal simulation, the history-corrected group constant Σ_{his} is evaluated from the plutonium concentration N_{his} calculated by the nodal solver:

$$\Sigma_{\text{his}} = \Sigma_{\text{nom}} \left[1 + k \left(\sqrt{\frac{N_{\text{his}}}{N_{\text{nom}}}} - 1 \right) \right]. \tag{4.4}$$

Consequently, a cross section at the nodal level is reconstructed in three steps:

1. Interpolation of nominal parameters and polynomial coefficients across the burnup tabulation;
2. Evaluation of the instantaneous polynomial deviation $\Delta\Sigma$ (Eq. 4.2);
3. Application of the plutonium history correction (Eq. 4.4).

The final polynomial library includes the following parameters: group cross sections and diffusion coefficients required by the neutron diffusion equation, discontinuity factors, microscopic cross sections and yields of the main fission-product neutron poisons, point-kinetics parameters, and pin-power form factors used for power reconstruction. Table 4.1 summarizes the complete list.

Table 4.1: Node-averaged parameters present in the polynomial library.

Category	**Parameters**
Cross sections & diffusion	Σ_a, Σ_f, $\nu\Sigma_f$, $\kappa\Sigma_f$, Σ_s, D, $1/v$, χ
Discontinuity factors	ADF, DF
Fission-product poisons	γ_{I135}, γ_{Xe135}, γ_{Pm149}, γ_{Sm149}, $\sigma_{a,I135}$, $\sigma_{a,Xe135}$, $\sigma_{a,Pm149}$, $\sigma_{a,Sm149}$
Kinetics parameters	β, λ
Power reconstruction	form function

4.2 Methodology and Spatial Discretization

Because a nuclear reactor consists of distinct regions with different physical behaviors, a single homogenization region cannot be applied globally. Based on the NuScale

reactor geometry, the computational domain representing the entire reactor core must be discretized and homogenized both radially and axially.

Radially, the active core contains three different fuel assembly types (as previously detailed in Fig. 3.6). Consequently, three independent assembly homogenizations are required. Figure 4.2 illustrates the radial discretization adopted for the model.

Furthermore, each fuel assembly must be subdivided into different axial regions, including the UOX fuel, the blanket, and the inactive regions. Figure 4.1 illustrates the axial discretization of a single fuel assembly. The UOX fuel, the blanket, and the inactive regions are homogenized separately. The inactive region is subdivided into multiple axial layers to capture its material variations.

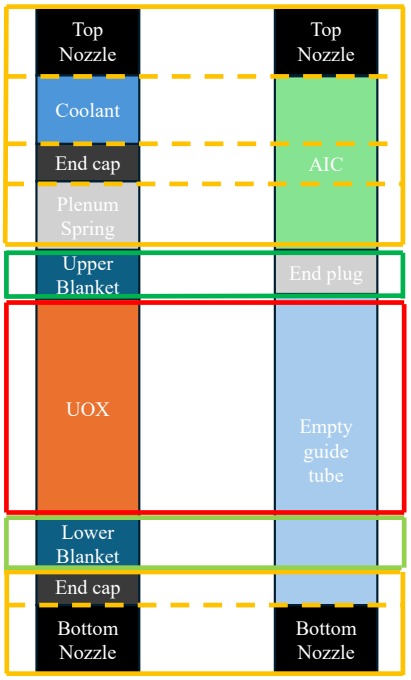


Figure 4.1: Representative axial discretization for group constant homogenization (not to scale).

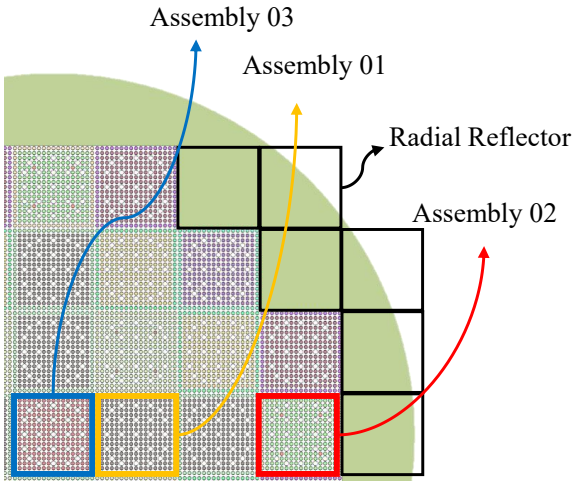


Figure 4.2: Representative radial discretization for group constant homogenization.

Figure ?? summarizes the overall workflow for generating the polynomial library. First, an infinite lattice calculation is performed with Serpent. Recalling Table 4.1, the cross sections, diffusion coefficients, fission-product poison parameters, and kinetics parameters are obtained from Serpent. Then, nodal calculations are performed with Ants to obtain the discontinuity factors and form functions. Finally, a unified polynomial library is generated for all reactor regions.

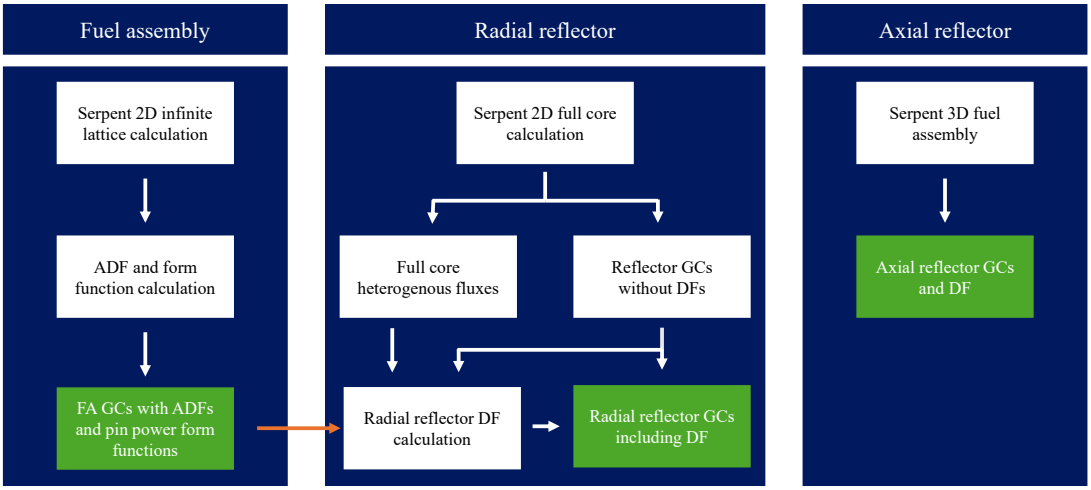


Figure 4.3: Workflow for the generation of the polynomial library [52].

4.3 Fuel assembly homogenization

Fuel group constant generation is performed using 2D single-assembly infinite-lattice models. Five independent models are developed to represent the distinct axial and radial regions of the core: three for the UOX fuel assemblies (Types 01, 02, and 03) and two for the upper and lower blankets.

The domain is a rectangular parallelepiped with a side length of 21.5036 cm and a height of 1.0 cm. For the UOX fuel and lower blanket, the guide tubes are modelled as channels filled with coolant, assuming fully withdrawn control rods. For the upper blanket, the guide tubes contain structural end plugs. The diffusion coefficient is calculated using the Cumulative Migration Method, as introduced in Section 2.1.2.

4.3.1 Serpent Setup

Serpent is chosen for this task both because it is developed by VTT and, more importantly, because it is a continuous-energy Monte Carlo reactor physics code. As previously discussed, this allows for an accurate representation of the heterogeneous fuel assemblies using their exact geometry, without introducing spatial approximations.

All Serpent simulations use the ENDF/B-VII.1 nuclear data library. The settings for the 2D infinite-lattice simulations use 100,000 neutrons per generation, with 500 active cycles and 80 inactive cycles. The number of inactive cycles is selected based on the convergence of the Shannon entropy [53]. As shown in Figure 4.4, k_{eff} and the Shannon entropy converge within 80 cycles. A standard LWR two-group energy structure is used, with the thermal energy boundary set at 0.625 eV.

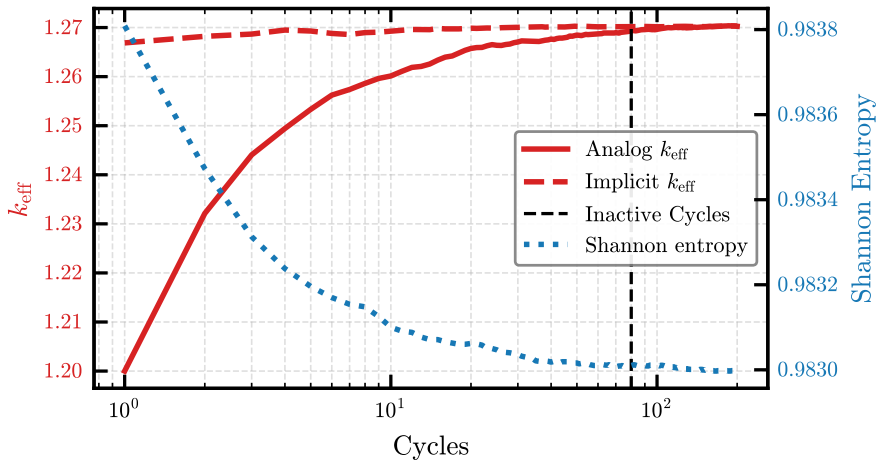


Figure 4.4: Convergence of the Shannon entropy and the eigenvalue over the initial cycles.

4.3.2 Burnup and Historical Conditions

When generating these libraries, it is important to distinguish between history and variation calculations, consistently with the polynomial library. Variations represent temporary deviations from the current operating conditions that affect neutronic parameters and are used to fit the instantaneous-condition polynomial. History describes the operating state of the reactor during the depletion calculation and is required for the plutonium history correction. Consequently, variations are always defined as perturbations with respect to the specific history being simulated [52].

To account for fuel evolution during irradiation and obtain the ^{239}Pu history model (Eq. 4.3), depletion calculations are performed for two different histories:

- Nominal history: Evaluated at the reference core and coolant temperatures and nominal soluble boron concentration;

- Off-nominal history: Evaluated under a hardened neutron spectrum, characterized by higher fuel and moderator temperatures and higher boron content.

The nominal and off-nominal history conditions are reported in Table 4.2. The depletion is simulated over 28 burnup steps, spanning from 0 to 45 MWd/kgU, using the Linear Extrapolation / Linear Interpolation predictor-corrector scheme. Since Fuel Types 01 and 02 remain in the core for three cycles and reach an average burnup of $\sim$ 12 MWd/kgU per cycle (Section 3.1.2), this range provides adequate margin. Fuel Type 03, which is discharged after a single cycle, is depleted over a reduced burnup and step count. As summarized in Table 4.2, a finer step size is adopted at the beginning of the irradiation cycle to resolve the rapid buildup of short-lived neutron poisons (e.g., Xenon and Samarium).

Table 4.2: Depletion calculation conditions.

Depletion condition	Parameter	Value
Nominal	Fuel temperature	900 K
	Boron concentration	1000 ppm
	Moderator temperature	557 K
Off-nominal	Fuel temperature	1000 K
	Boron concentration	1500 ppm
	Moderator temperature	580 K
Burnup steps (28 points), MWd/kgU		
0, 0.05, 0.1, 0.2, 0.3, 0.6, 1, 1.5, 2, 3, 4, 5, 6, 7, 8, 9, 10, 11, 12, 13, 14, 15, 18, 21, 24, 31, 37, 45		

4.3.3 Instantaneous Variations and Branching Matrix

Once the isotopic compositions are known at each burnup step, the instantaneous dependence of the cross sections on the operating conditions is evaluated to determine the coefficients in Equation 4.2. Branch variations are applied around the nominal state at each burnup point. Nominal conditions are set first. Then, moderator temperature, fuel temperature, and boron concentration are changed one at a time within the expected NuScale operating range.

Furthermore, three spacer-grid configurations (none, HTP, and HMP) are considered to account for the different spacer-grid types. However, not all spacer-grid branches are applied to the blanket regions: the lower blanket includes only the "No spacer grid" and "HMP" configurations. In contrast, the upper blanket has no spacer grid. The complete set of branch variations is summarized in Table 4.3.

Table 4.3: Branch conditions for cross-section generation.

Branch	Fuel Temp. [K]	Mod. Temp. [K]	Boron Conc. [ppm]
Nominal	900	557	1000
Moderator temperature low	900	444	1000
Moderator temperature high	900	600	1000
Fuel temperature low	600	557	1000
Fuel temperature high	1200	557	1000
Boron concentration low	900	557	0
Boron concentration high	900	557	3200
No spacer grid	–	–	–
HTP spacer grid	–	–	–
HMP spacer grid	–	–	–

The `branch` and `casematrix` features in Serpent run multiple cases and perform

depletion and branching simultaneously. After generating the isotopic compositions along the history paths, Serpent restarts from the saved compositions to evaluate the instantaneous branches [52]. Since the fuel response to temperature and boron changes varies slowly with burnup, all variations are studied at only 9 burnup points (0, 1, 4, 8, 12, 15, 21, 31, and 45 MWd/kgU). Spacer-grid variations are studied at all 28 steps.

4.3.4 Discontinuity Factors and Form Functions

The final step in the library generation process is the evaluation of the Assembly Discontinuity Factors and the Pin Power Form Functions (FFs). ADFs are needed to go from the detailed Monte Carlo model to the homogeneous nodal diffusion model. Similarly, Form Functions, defined as the ratio between the heterogeneous fission power of a single pin and the homogenized scalar flux of the assembly, are required to reconstruct the local pin power distribution lost during homogenization.

Although Serpent can provide ADF values as output, these factors are generally not used because the homogeneous solution depends on the specific nodal model adopted. Therefore, dedicated calculations are required to generate discontinuity factors consistent with the deterministic nodal formulation [52].

Kraken generates these parameters through an automated script. For each state simulated by Serpent, Kraken extracts the heterogeneous group constants and boundary currents, and performs a dedicated 2D standalone Ants simulation of the homogenized node. The ADFs are then computed using the ratio between the Serpent heterogeneous surface fluxes and the Ants homogeneous surface fluxes:

$$\mathrm{f}_{s,g} = \frac{\phi_{s,g}^{\mathrm{Serpent,2D}}}{\Phi_{s,g}^{\mathrm{Ants,2D}}}. \tag{4.5}$$

The pin-power form functions are generated by normalizing the pin fission power from Serpent to the node-averaged flux calculated by Ants.

4.4 Reflector Homogenization

Unlike the active core, the radial and axial reflectors do not contain fissile material and therefore do not undergo depletion. As a result, reflector cross sections are generated at zero burnup and have no dependence on fuel temperature ($c_1 = c_2 = 0$ in Equation 4.2). Furthermore, diffusion coefficients in reflector regions are calculated using a transport correction instead of the CMM method to account for anisotropic scattering at steel-water interfaces.

4.4.1 Radial Reflector

For the radial reflector, the whole-core simulation is necessary for the generation of the reflector's DF. This is because ADFs are generated assuming reflective boundary conditions. Thus, in heterogeneous regions with different neutron spectra, such as

the interface between the fuel and the reflector, they do not provide accurate results. Therefore, the neutron fluxes across the two regions are required to compute the discontinuity factors.

After the Serpent simulation is performed, both reflector group constants without discontinuity factors and whole-core heterogeneous fluxes and currents are available. The DFs on the reflector side are calculated as the ratio between the heterogeneous surface flux from the Serpent simulation and the homogeneous surface flux from a single node Ants calculation [52]:

$$f_{\text{refl}}^{\text{Ants}} = \frac{\phi_{\text{refl}}^{\text{Serpent2D}}}{\Phi_{\text{refl}}^{\text{Ants}}}. \tag{4.6}$$

The DFs on the fuel side are obtained following the same approach:

$$f_{\text{fuel}}^{\text{Ants}} = \frac{\phi_{\text{fuel}}^{\text{Serpent2D}}}{\Phi_{\text{fuel}}^{\text{Ants}}}. \tag{4.7}$$

However, since both the fuel and the corresponding ADF, $f_{\text{fuel}}^{\text{ADF}}$, are obtained from an infinite-lattice calculation, the direct use of $f_{\text{refl}}^{\text{Ants}}$ would introduce an inconsistency at the interface between the active core and the reflector. To enforce flux continuity in a mathematical sense, the reflector discontinuity factor is corrected as follows:

$$f_{\text{refl}} = f_{\text{refl}}^{\text{Ants}} \cdot \frac{f_{\text{fuel}}^{\text{ADF}}}{f_{\text{fuel}}^{\text{Ants}}}. \tag{4.8}$$

4.4.2 Axial Reflector

For the non-active axial portion of the assembly, a 3D single-assembly simulation is performed, assuming reflective boundary conditions in the radial direction. According to Figure 3.1, a separate cross section has been created for each non-active region: bottom nozzle, end cap (with empty guide tube), plenum spring, end cap (with AIC in the guide tube), coolant (with AIC in the guide tube), and top nozzle. The DFs are calculated using the same approach as for the radial DFs, by performing single-node simulations in Ants 3D and computing the ratio between heterogeneous fluxes from Serpent and homogeneous fluxes from Ants. However, due to the current limitations of Ants, no correction based on fuel ADFs is applied in the axial regions.

4.5 Infinite-Lattice Comparison

Before constructing the whole-core neutronics model in the deterministic code, a verification is carried out to ensure the correctness of the generated polynomial library. This consists of comparing the results of a single fuel element simulated with both Serpent and Ants in an infinite-lattice configuration with reflective boundary conditions. In this case, Serpent is considered the reference solution.

The simulations are performed under nominal conditions, i.e., imposing a fuel temperature of 900 K, a coolant temperature of 557 K, and a boron concentration

of 1000 ppm. This verification does not assess the accuracy of the polynomial under different operating conditions. It only checks whether the generated library gives correct results under nominal conditions. The verification also checks whether depletion is handled correctly simulating multiple burnup steps.

Table 4.4: Comparison of infinite multiplication factor k_∞ computed with Serpent and Ants at nominal conditions and burnup 0.0 MWd/kgU.

Fuel	**SERPENT** k_∞	**ANTS** k_∞	**Difference [pcm]**
01	1.27019 ± 0.00008	1.27018	1
02	1.26433 ± 0.00008	1.26432	1
03	1.15800 ± 0.00007	1.15799	1
upper blanket	1.00679 ± 0.00007	1.00678	1
lower blanket	1.07174 ± 0.00007	1.07173	1

Note: SERPENT uncertainties are reported as $\pm 1\sigma$
(one standard deviation, statistical uncertainty from the Monte Carlo simulation).

At zero burnup (Table 4.4), there is excellent agreement between the reference Monte Carlo code and the deterministic solver, with the differences being within the statistical uncertainty of the Serpent calculation. However, in this case, it is important to evaluate how the library behaves as a function of burnup. Figure 4.5 shows the comparison between Ants and Serpent of k_∞ as a function of burnup for the fuel regions.

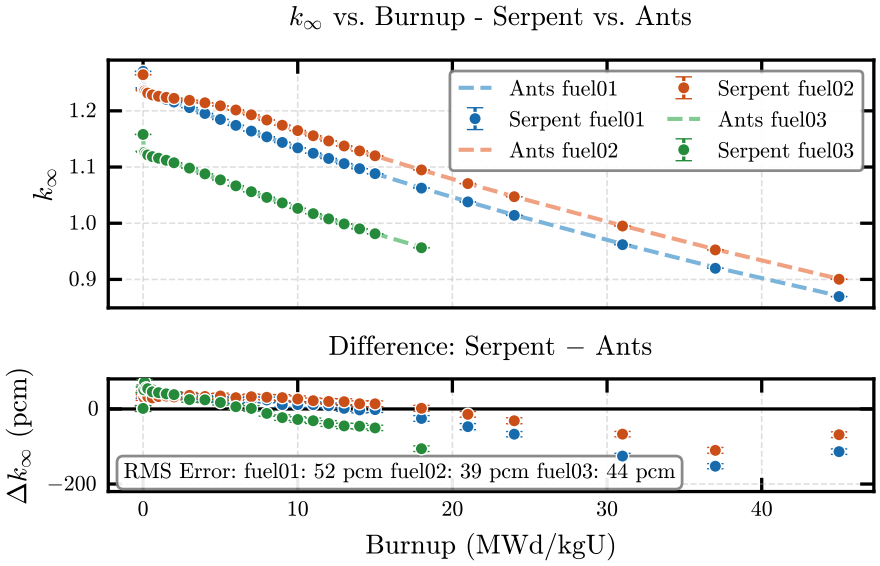


Figure 4.5: Comparison of infinite multiplication factor k_∞ computed with Serpent and Ants at nominal conditions for fuel UOX.

The lower the enrichment, the lower the infinite multiplication factor. However,

Fuel Type 01 initially exhibits a higher k_∞ than Fuel Type 02, despite its lower enrichment. This is because Fuel Type 02 contains gadolinium. The ^{155}Gd and ^{157}Gd isotopes have high microscopic absorption cross sections, which reduce initial reactivity. As the gadolinium depletes, its effect on reactivity decreases, allowing Fuel Type 02 to overtake Type 01. Fuel Type 03 shows a steeper decline because its lower initial ^{235}U inventory is depleted faster.

Regarding the blanket regions (Figure 4.6), the upper blanket exhibits a lower initial k_∞ than the lower blanket, despite having the same fuel composition. This occurs because the upper blanket guide tubes contain stainless steel instead of water, which reduces moderation and increases the macroscopic absorption cross section. This leads to a harder neutron spectrum, which increases the production of ^{239}Pu through neutron capture in ^{238}U. The increasing ^{239}Pu inventory partially compensates for ^{235}U depletion. As a result, the k_∞ decrease becomes less pronounced, and the upper and lower blanket curves become closer at higher burnup.

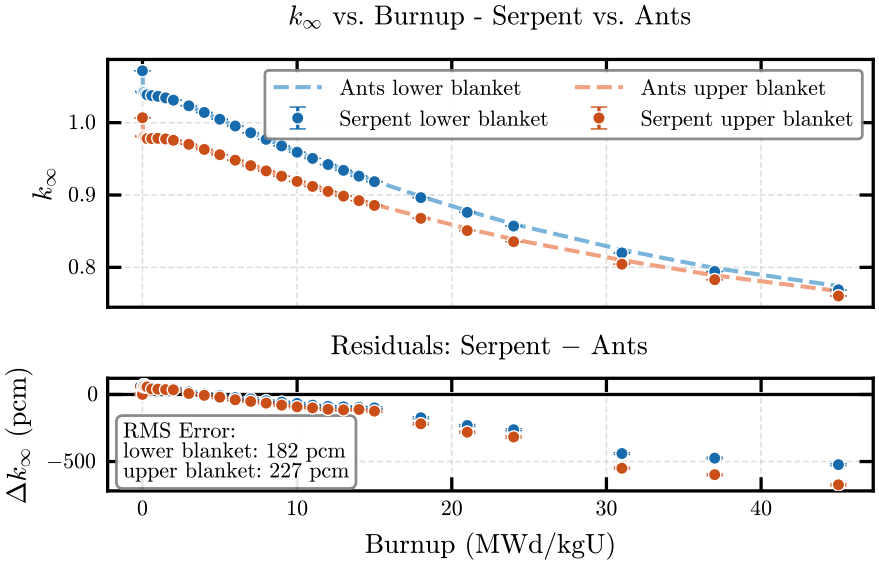


Figure 4.6: Comparison of infinite multiplication factor k_∞ computed with Serpent and Ants at nominal conditions for the fuel blanket.

Comparing the deterministic and stochastic solvers, Ants captures the main depletion behaviour, including the initial reactivity drop caused by ^{135}Xe buildup. However, differences between the two solvers increase with burnup. For the UOX assemblies, Ants overestimates k_∞ by approximately 150 pcm at higher burnups. This overestimation becomes more pronounced in the blanket regions, exceeding 500 pcm at the end of the cycle. The following section presents a detailed assessment of whether these differences are acceptable for whole-core calculations.

Furthermore, the results show that the numerical difference is larger for lower initial fuel enrichment. Low-fissile regions, such as Fuel Type 03 and the 2% enriched blankets, show the largest differences. This suggests that, in low-fissile regions, the

macroscopic cross sections used by the deterministic solver are more affected by approximations in the isotopic inventory calculation.

4.5.1 Isotopic inventory and burnup step sensitivity

The discrepancies in k_∞ between Ants and Serpent are driven by two main factors: short-lived neutron poisons at the beginning of the cycle, and the evolution of the fissile inventory at high burnup. The following discussion focuses on the upper blanket, as it shows the largest error. The same physical behaviour is expected in the other regions.

At the beginning of the depletion, Ants slightly underestimates k_∞. This is caused by an overestimation of neutron poisons (^{135}Xe and ^{149}Sm), reducing the multiplication factor. Further details can be found in Appendix B. This limitation in accurately describing the transient behavior of these poisons is one reason why deterministic nodal solvers often use equilibrium models for Xenon and Samarium.

As depletion proceeds, however, the trend reverses and Ants progressively overestimates k_∞ by over 500 pcm. Neutron poisons cannot explain this high-burnup discrepancy; instead, it is caused by the fissile inventory. Figure 4.7 shows that Ants overestimates the ^{239}Pu concentration compared to Serpent. This leads to an overestimation of the macroscopic fission cross section and k_∞.

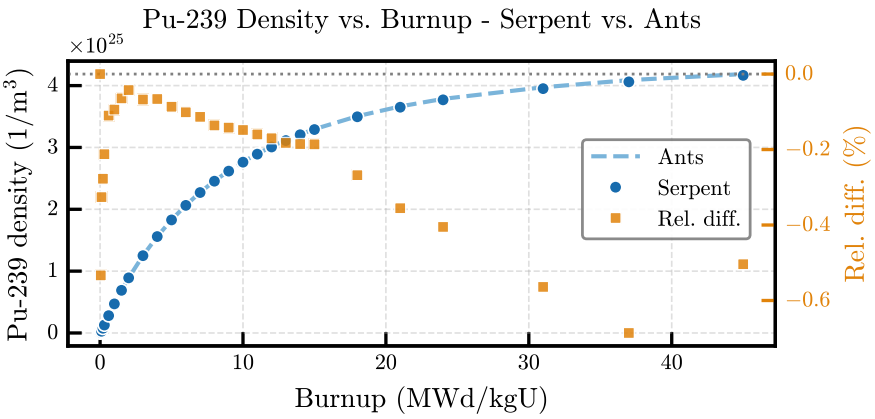


Figure 4.7: Plutonium-239 concentration: comparison between Serpent and Ants.

This sensitivity to the plutonium inventory explains why lower-enriched materials exhibit larger errors. With a lower initial ^{235}U content, the neutron balance becomes dependent on ^{239}Pu earlier in the cycle. Consequently, even a small error in the predicted Pu inventory impacts k_∞. This also explains the larger discrepancy in the upper blanket compared to the lower blanket: its harder neutron spectrum breeds more ^{239}Pu, thus amplifying the error.

To further investigate this behavior, a dedicated Serpent simulation with 52 burnup steps is performed for the upper blanket. As shown in Figure 4.8, increasing the number of burnup steps reduces the root mean square (RMS) error from 227 pcm to

102 pcm, improving the agreement between the deterministic and Monte Carlo results. The finer time steps allow for a more precise solution of the Bateman equations and a more accurate evaluation of the isotope inventory, resulting in a more precise polynomial library and, consequently, a more accurate k_∞.

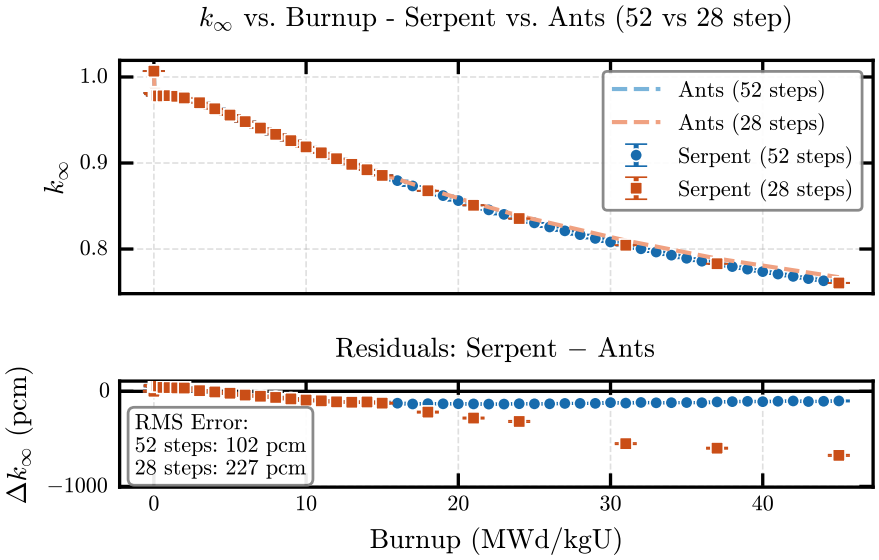


Figure 4.8: Comparison of infinite multiplication factor k_∞ with 28 and 52 burnup steps in the upper blanket.

It is interesting to note that the 52-step simulation does not improve the estimation of the poison concentrations. A comparison of the poisons for the 28- and 52-step cases is provided in Appendix B. This is because the Xenon and Samarium concentrations are sensitive to the first few burnup steps. Since the extra steps in the 52-step model are at higher burnups, they do not improve the initial overestimation.

In conclusion, the differences between the stochastic and deterministic codes are mainly due to the discretization used to generate the cross sections. Increasing the number of depletion steps improves the accuracy of the isotopic evolution. However, the polynomial library used in the following sections is based on the 28-step discretization. This choice is a compromise between accuracy and the computational cost of generating the library.

Although future studies could consider a finer burnup mesh, the error introduced by using 28 steps in the whole-core calculations is sufficiently small, as shown in Chapter 5. As demonstrated, the largest discrepancies occur in the blanket regions at very high burnups. In the core, these peripheral regions experience lower neutron fluxes than the active fuel and do not reach such high burnup levels during a single cycle. Therefore, the 28-step library is considered adequate.

Chapter 5

Multiphysics Coupling

Once the polynomial library for the nodal code has been generated and verified, the next step is to perform a whole-core simulation. The main objective is to obtain the equilibrium cycle and to determine the critical boron concentration (CBC). The coupling is introduced gradually. First, a standalone neutronic simulation is performed. Then, the thermal-hydraulic module is added, followed by the fuel behavior module.

In the simulation using only the neutronic module, the results are compared with those from a whole-core Serpent simulation. This comparison helps identify the accuracy of the deterministic solver and its library at the whole-core level. Subsequently, by adding the multiphysics solvers, the objective is to evaluate how the results change when the individual solvers are progressively introduced. Additionally, the coupled neutronics and thermal-hydraulics results are compared with those reported in the FSAR [39], since the FSAR results were obtained using a coupled N-TH simulation.

5.1 Standalone neutronics simulation

The whole-core simulation is performed at the nominal reactor power of 160 MWth, which is kept constant throughout the simulation. Each fuel cycle lasts 695 days and is followed by a three-week fuel shuffling outage. Xenon depletion is considered during the first fuel cycle, while equilibrium xenon conditions are assumed for the subsequent cycles.

In the Ants model, the reactor core is divided according to the homogenization scheme described in Section 4.2. Radially, each fuel assembly forms a homogenized region, while the radial reflector is divided into 32 nodes. Axially, the core is discretized into 32 nodes, defined based on the homogenized fuel-assembly regions and spacer-grid locations, as shown in Table 5.1.

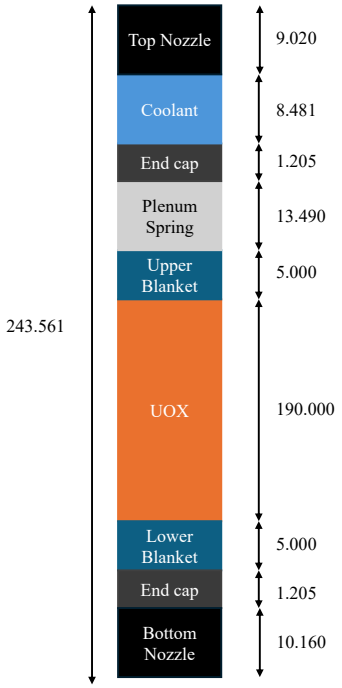


Figure 5.1: Axial structure of fuel rod (not to scale), all dimensions are in cm.

Region	N. nodes	Height (cm)
Bottom nozzle	1	10.160
End cap	1	1.205
Lower blanket	1	3.555
Lower blanket + SG1	1	1.445
UOX + SG1	1	3.000
UOX	5	9.322
UOX + SG2	1	4.445
UOX	5	9.322
UOX + SG3	1	4.445
UOX	5	9.322
UOX + SG4	1	4.445
UOX	4	8.459
Upper blanket	1	5.000
Plenum spring	1	13.490
End cap	1	1.205
Coolant	1	8.481
Top nozzle	1	9.020

Table 5.1: Axial mesh discretization and node heights for the whole-core Ants model.

5.1.1 Equilibrium Cycle Search

The first objective is to identify the equilibrium cycle, defined as the cycle in which the main reactor parameters show no significant variations between consecutive cycles. Nine fuel cycles are simulated for this purpose. Since each fuel assembly remains in the core for three fuel cycles, the equilibrium is expected around the 7th–8th cycle [54].

Figure 5.2 shows the evolution of the critical boron concentration over the nine fuel cycles, as calculated by Serpent and Ants. During the first fuel cycle, all fuel assemblies contain fresh fuel; therefore, a relatively large amount of boron is required to compensate for the excess reactivity. However, the critical boron concentration in the first cycle decreases rapidly, by approximately 500 ppm, due to the buildup of neutron poisons. Once the concentration of these fission products reaches equilibrium, the critical boron concentration decreases almost linearly due to fuel depletion.

As the number of fuel cycles increases, the results converge towards the equilibrium cycle. Figure 5.3 shows that the equilibrium cycle is reached at the 8th fuel cycle. The difference in critical boron concentration between the 7th and 8th cycles is approximately 3 ppm, indicating that the core has reached a stable condition.

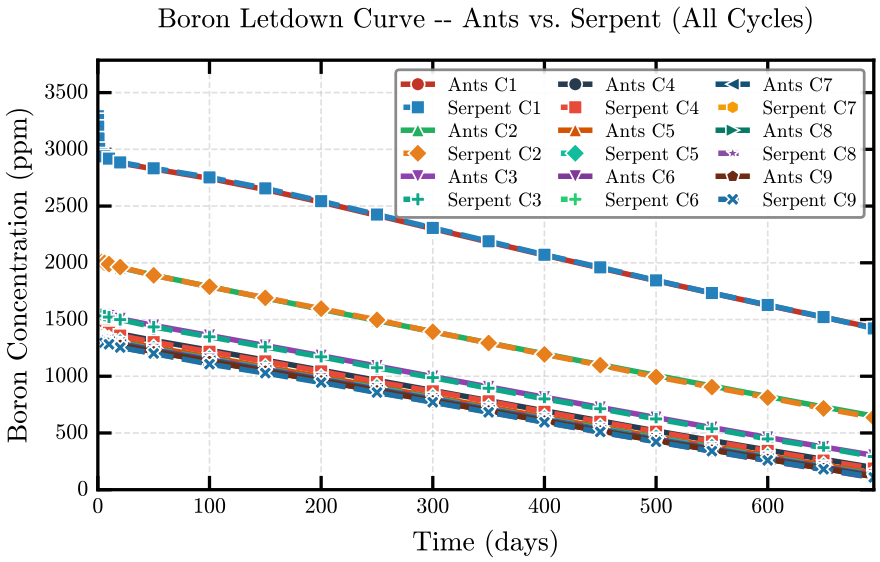


Figure 5.2: Critical boron concentration over nine fuel cycles: comparison between Ants and Serpent.

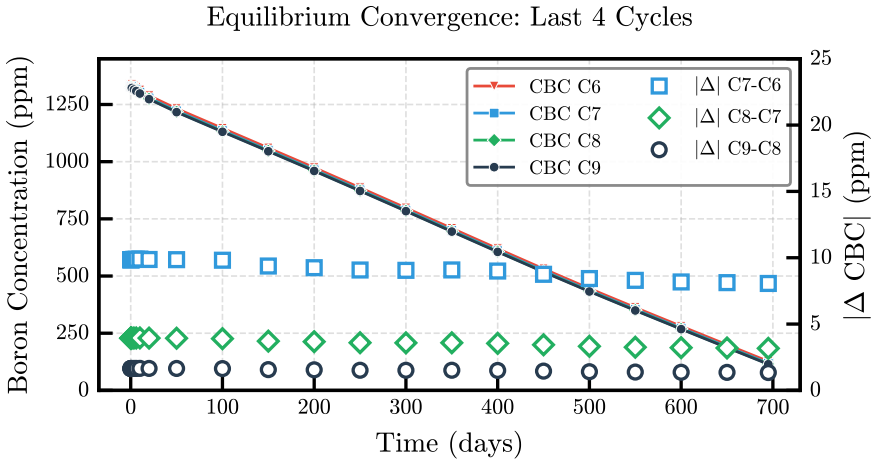


Figure 5.3: Equilibrium cycle convergence (cycles 6–9). Critical boron concentration (solid lines, left axis) and absolute difference between consecutive cycles (scatter markers, right axis).

5.1.2 Code Verification at Equilibrium

Having identified the 8th cycle as the equilibrium cycle, a comparison between Ants and Serpent is performed to verify the accuracy of the deterministic whole-core model. Figure 5.4 presents the comparison between Serpent and Ants for the critical boron concentration at the equilibrium cycle.

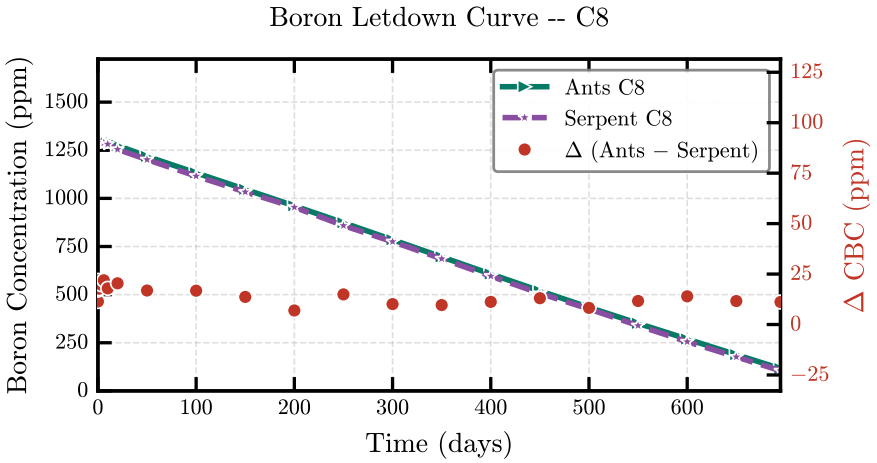


Figure 5.4: Critical boron concentration at the equilibrium cycle: comparison between Ants and Serpent.

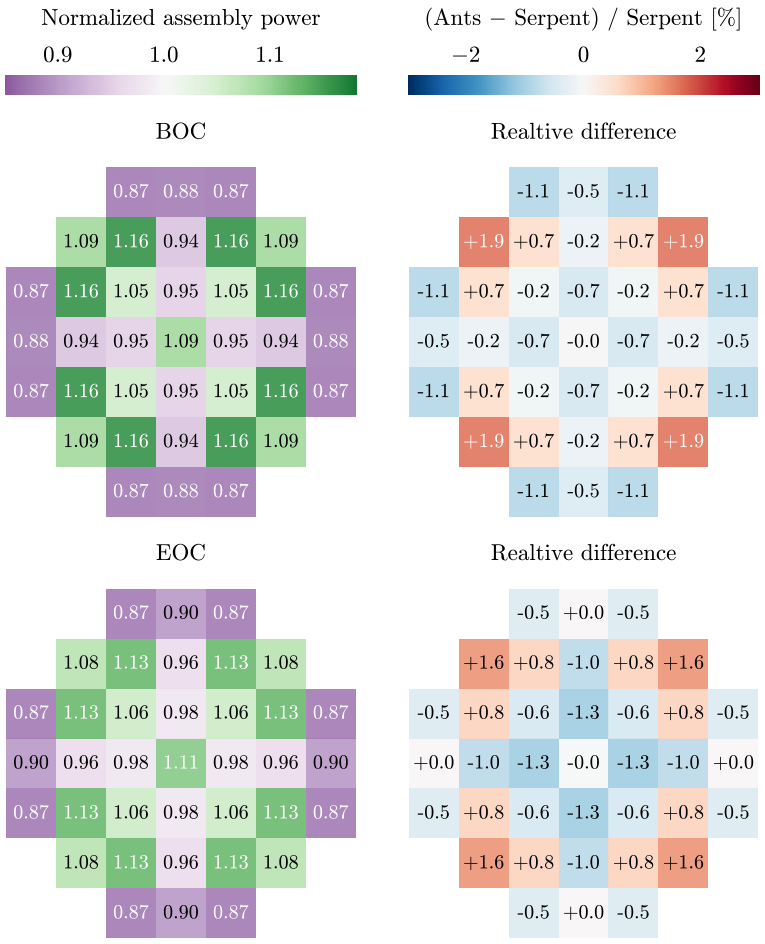


Figure 5.5: Comparison of radial power distributions at BOC and EOC. The left column shows the normalized assembly power calculated by Ants, while the right column shows the relativ difference compared to the Serpent reference.

Figure 5.5 shows the relative radial assembly power distribution at the beginning of cycle (BOC) and the end of cycle (EOC) for the equilibrium cycle. The calculated power distributions are compared with the Serpent results, which have a radial power uncertainty of approximately 0.2%. The maximum discrepancy is below 2% and occurs in the freshly loaded fuel assemblies containing gadolinium. This is mainly due to the limitations of the two-step approach. In particular, these assemblies are surrounded by neighboring assemblies with different neutron spectra, resulting in a mismatch between the actual local conditions and those used to generate the homogenized cross sections.

Overall, the whole-core simulations show good agreement between Ants and Serpent. The critical boron concentration at the equilibrium cycle shows a discrepancy of less than 20 ppm, while the assembly power distribution is also reproduced with sufficient accuracy.

5.1.3 Standalone Model Characteristics

Once the model is verified, the main core characteristics are calculated. These uncoupled neutronic results are used as a reference to evaluate the effects of thermal-hydraulic and fuel behavior feedbacks in the following sections.

Figure 5.6 shows the average axial power distribution within the active core at the beginning and end of the equilibrium cycle. The spacer grids cause local depressions in the axial power profile. Moreover, the power distribution is nearly symmetric. This is expected primarily because the control rods are fully withdrawn. Additionally, the standalone simulations impose a uniform moderator temperature, neglecting axial density variations.

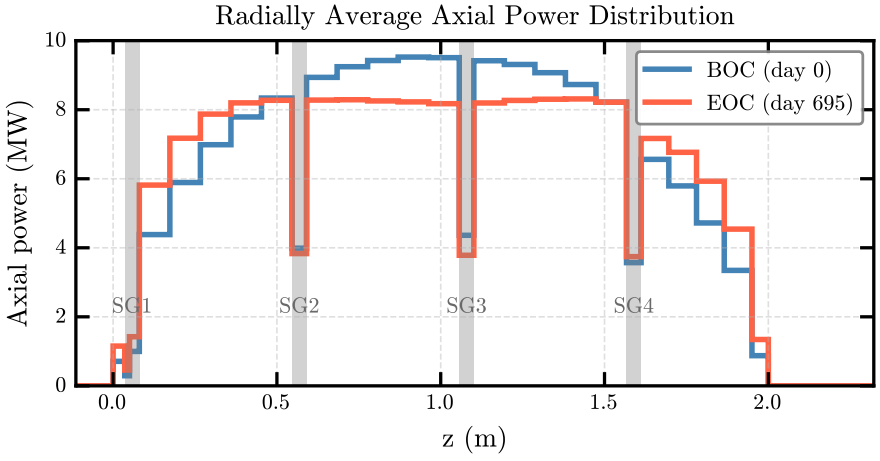


Figure 5.6: Average axial power distribution at BOC and EOC.

The axial power profile becomes flatter at the end of the cycle. At BOC, the power distribution reaches its maximum at the core mid-plane due to the higher neutron flux in the central region. Since the central region operates at a higher power, the fuel depletes more rapidly than in the upper and lower regions. As burnup progresses,

this greater depletion of fissile material in the central region reduces local power. At the same time, the less depleted fuel near the axial ends contributes a larger fraction of the total power.

Figure 5.7 shows the average assembly burnup at BOC and the EOC for the equilibrium cycle. The maximum average assembly burnup reaches approximately 36.2 MWd/kgU. This value confirms that generating homogenized cross sections up to a burnup of 45 MWd/kgU provides a sufficient burnup range for the present analysis and covers all operating conditions considered during reactor operation.

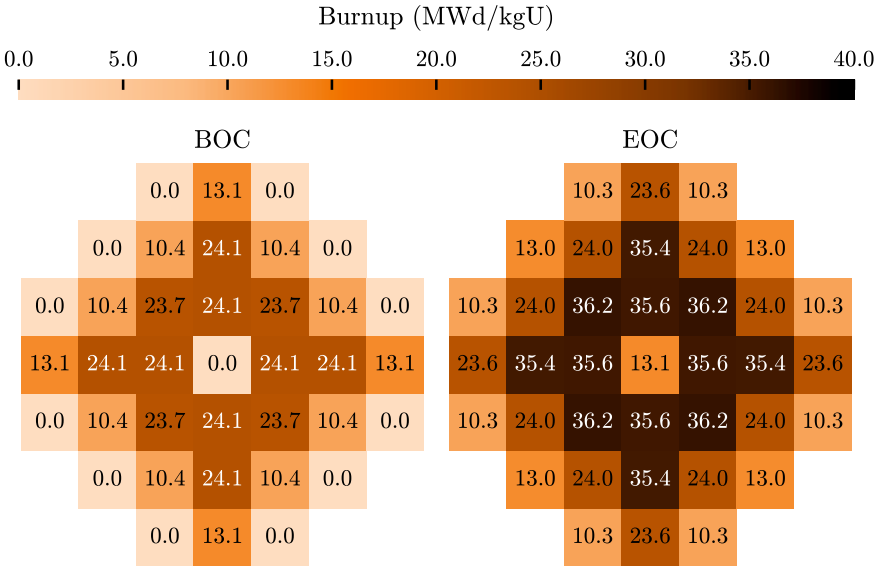


Figure 5.7: Burnup maps at BOC and EOC.

Table 5.2: Reactivity parameters and coefficients.

Parameter	State	Value	VERA	FSAR	Unit of measurement
DTC	BOC	-2.65	-2.69	-1.63	pcm/K
	EOC	-2.87	-2.92	-2.07	pcm/K
MTC	BOC	-6.72 to -24.60	-4.34 to -22.72	0.00 to -32.50	pcm/K
Boron Coeff.	BOC	-7.73	-	-7.6 to -13.7	pcm/ppm
	MOC	-8.08	-		pcm/ppm
	EOC	-8.62	-		pcm/ppm

Table 5.2 shows the feedback coefficients: the Doppler temperature coefficient (DTC), moderator temperature coefficient (MTC), and boron coefficient. In particular, the table shows the DTC at both BOC and EOC. It is obtained by performing three simulations at different fuel temperatures and fitting the three resulting points to obtain the slope. Good agreement is observed with VERA [42]. The same approach

is used for the boron coefficient by varying the boron concentration. The coefficient is also reported at the Middle of Cycle (MOC), and the comparison is possible only with the FSAR. For the MTC, only the BOC values are shown. In this case, a range of values is reported by varying the moderator temperature and fitting the resulting points.

5.2 Neutronics and thermal-hydraulics

To overcome the limitations of standalone neutronic simulations, which rely on fixed, spatially uniform temperatures, the neutronic and thermal-hydraulic codes are coupled: Ants provides Kharon with the power distribution, while Kharon returns the local coolant temperature and density to Ants. This coupling accounts for moderator feedback.

The NuScale reactor operates under natural circulation, with the coolant flow rate determined by the balance between buoyancy and pressure losses along the primary loop, including the steam generators. Modeling this behavior would require a full-loop system code, which is beyond the scope of this work. Kharon therefore models only the active core region, with a fixed inlet mass flow rate imposed as a boundary condition; the nozzle and other non-active regions are included in the model geometry but are not the focus of the analysis.

5.2.1 Thermal-Hydraulics model

The thermal-hydraulic model uses the same radial and axial discretization as the neutronic model, with a one-to-one correspondence between Kharon and Ants nodes. Therefore, the model can be described as an assembly-level solver with axial discretization.

Ants provides the power, which is used as the thermal-hydraulic boundary condition for Kharon. Since the primary loop is not resolved, the coolant boundary conditions are imposed directly at the core inlet. The mass flow rate, temperature, and outlet pressure are taken from the NuScale FSAR and are set to 14.52 kg/s, 531.5 K, and 12.85 MPa, respectively [39]. As detailed in Section 3.2.2, each axial node is characterized macroscopically by its porosity, hydraulic diameter, and thermal diameter.

Recalling the modeling assumptions introduced in Section 3.2.2, Kharon models only distributed pressure losses based on the hydraulic diameter and does not account for concentrated losses. In addition, some geometrical data, especially for the nozzles, are unavailable, so their hydraulic diameter must be approximated. Together with the fixed inlet flow rate used instead of a full-loop model, these limitations mean that the pressure losses calculated by Kharon may not accurately represent the real system.

However, since the flow rate is imposed as a boundary condition rather than calculated from the pressure balance, inaccuracies in the pressure losses do not affect the flow rate. They can, however, affect the pressure field: since the outlet pressure is

prescribed, the pressure in each cell is calculated backward from the outlet. Therefore, underestimated pressure losses lead to lower in-core pressure and may affect the coolant density and temperature, which in turn feed back into the neutronics.

In practice, this effect is expected to be small. At the operating pressure of 12.85 MPa, the subcooled liquid coolant is incompressible. Therefore, these pressure variations have a negligible effect on the coolant density and temperature, unless they are large enough to cause local boiling. The sensitivity analysis in Appendix C, which varies the nozzle hydraulic diameter and the axial extent of the non-active region, shows that these approximations have little effect on the pressure drop and coolant properties.

Another assumption of the Kharon model is the closed-channel approximation, which does not allow lateral cross-flow or enthalpy exchange between adjacent assemblies. This is a limitation for open-lattice cores such as the NuScale design, but it is still a reasonable approximation for this macroscopic multiphysics study. The NuScale reactor operates under natural circulation, with low axial velocities and small pressure differences. This results in small radial pressure gradients [55]. Moreover, the thermal-hydraulic module does not model local fluid dynamics in detail; it provides the neutronic code with reliable macroscopic feedback parameters. For this purpose, treating the channels separately should be sufficient.

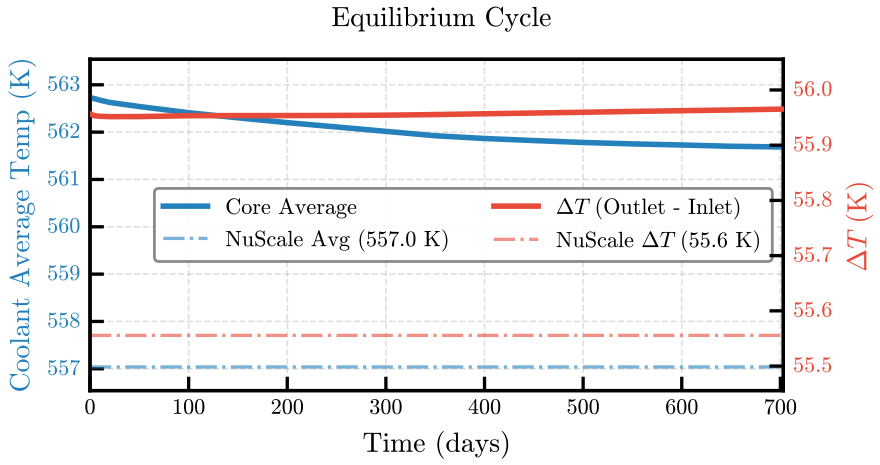


Figure 5.8: Average coolant temperature and average temperature difference between inlet and outlet at equilibrium cycle.

Figure 5.8 shows the average core coolant temperature and the inlet–outlet temperature rise at the equilibrium cycle, both in good agreement with the NuScale reference under nominal conditions (about 1% differences).

5.2.2 Results of neutronics and thermal-hydraulics coupling

Coupling the thermal-hydraulic solver provides the coolant temperature distribution in both the axial and radial directions. Figure 5.9 shows the variation of the average

coolant temperature among the fuel assemblies. This variation depends on each assembly's enrichment, burnup, and proximity to the core center.

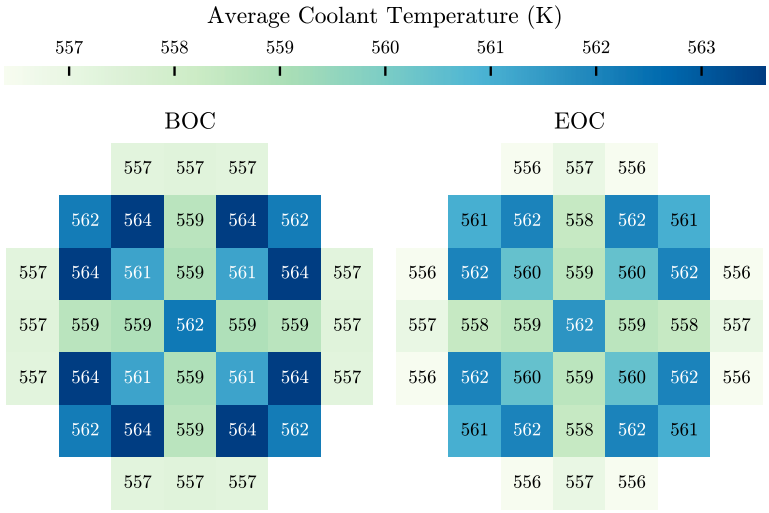


Figure 5.9: Radial coolant temperature distribution at equilibrium cycle at assembly level.

The introduction of the moderator density feedback affects the axial power shape. Figure 5.10 shows the average axial power and coolant distribution at BOC and EOC during the equilibrium cycle. The power distribution is no longer symmetric because the coolant temperature is not uniform. At BOC, the lower coolant temperature in the bottom axial region results in a higher density and therefore better neutron moderation, leading to higher power in this region. As the cycle progresses, the lower region depletes faster than the upper region, shifting the power toward the upper core. By EOC, the axial power profile becomes more top skewed. The similarity between the coupled N+TH and standalone N results at EOC is probably a coincidence.

Multiphysics coupling also affects global reactivity. Figure 5.11 shows the comparison between the standalone neutronics simulation and the coupled simulation of the critical boron concentration at the equilibrium cycle. Throughout the cycle, the N and TH model requires less soluble boron to maintain criticality. The maximum difference occurs at BOC (ΔCBC $\approx$ 33 ppm).

Instead of the constant and uniform coolant temperature of 557 K assumed in the standalone neutronics calculation, the coolant temperature now varies. As shown in Figure 5.8, the resulting average coolant temperature is approximately 562 K, slightly higher than the value imposed in the standalone simulation. A higher coolant temperature reduces coolant moderation, in accordance with the MTC (Table 5.2), resulting in lower excess reactivity in a thermal reactor. At BOC, the boron worth is approximately -7.7 pcm/ppm, so the 33 ppm difference translates to a reactivity decrease of roughly 255 pcm.

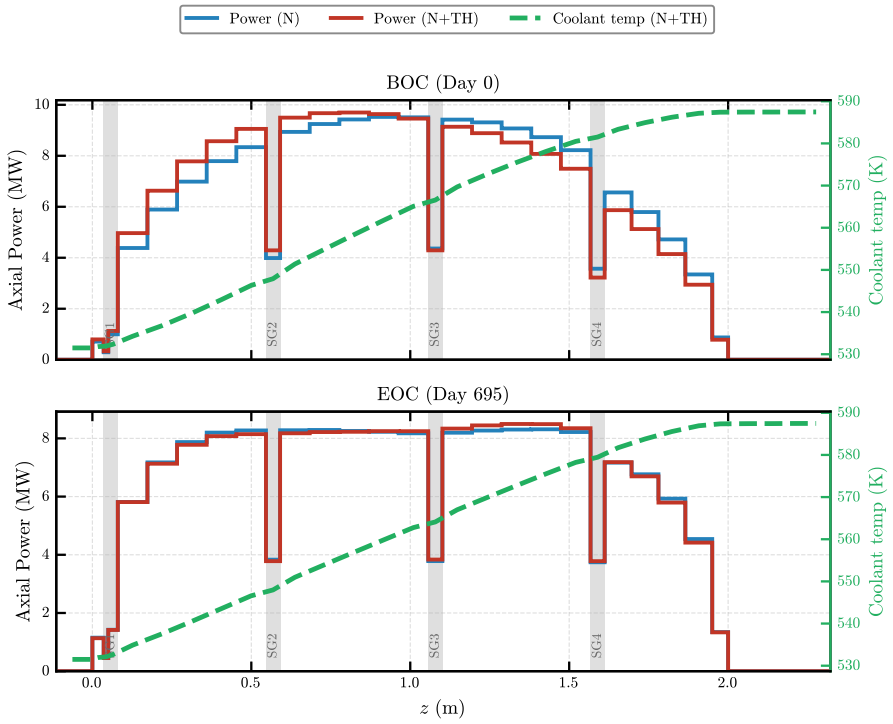


Figure 5.10: Axial power and coolant distribution at equilibrium cycle at the beginning and end of the cycle.

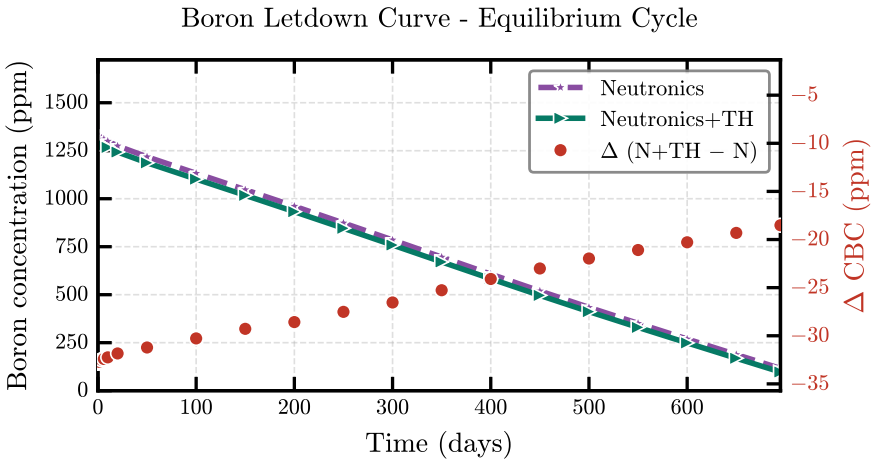


Figure 5.11: Critical boron concentration at equilibrium cycle: comparison between standalone N and coupled N+TH calculations.

As fuel depletion progresses, the absolute ΔCBC decreases, reaching approximately 20 ppm at EOC. However, this difference becomes more significant relative to the total boron concentration. At EOC, the soluble boron concentration is about 90 ppm, so a 20 ppm difference represents more than 20% of the total concentration.

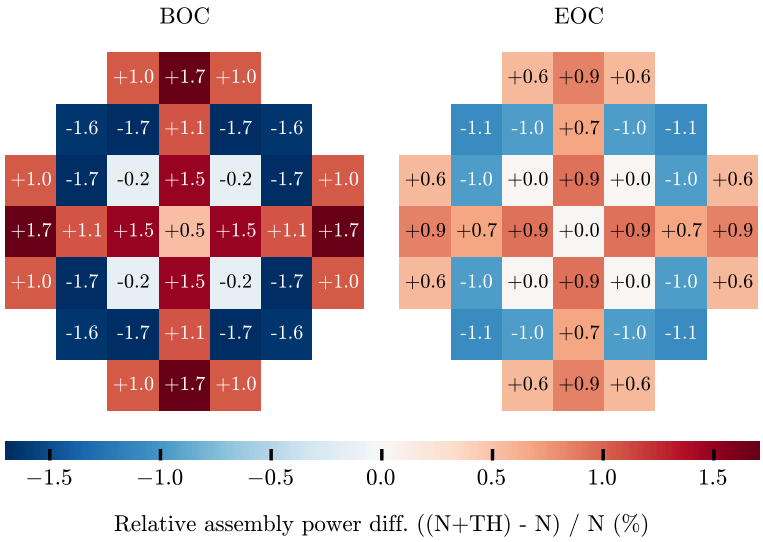


Figure 5.12: Assembly power relative difference (%) between N+TH and N, at BOC (left) and EOC (right).

Figure 5.12 shows the power difference between the N+TH and N cases at BOC and EOC. The power distribution changes only slightly, especially at EOC. Since both simulations use the same total core power of 160 MWth, the total power remains constant. Therefore, a correlation between coolant temperature and assembly power cannot be clearly established. In general, assemblies with higher coolant temperatures tend to show lower power. However, exceptions occur because the surrounding assemblies also affect the power distribution.

The spatial power difference pattern remains similar throughout the cycle, but its magnitude decreases towards EOC. This is mainly due to burnup, which makes the radial power distribution more uniform. As a result, the assemblies become more similar to each other, leading to smaller differences in coolant temperature and, consequently, weaker moderator feedback. This shows that the differences between the standalone neutronic model and the coupled N+TH model are larger at the beginning of the cycle and decrease as irradiation progresses.

Although comparison with the FSAR reference [39] is not the main objective of this work, the assembly and relative pin power results are compared with the reference in Appendix D. Overall, the results show good agreement, considering that the model is not intended to reproduce the NuScale design in detail.

5.3 Neutronics, themal-hydraulics and fuel behaviour

The final step consists of coupling neutronics, thermal-hydraulics, and fuel behavior. In this configuration, SuperFINIX calculates the fuel temperature, gap conductance, and material thermal conductivities, replacing the fixed 900 K assumption used in

the previous steps. This allows the Doppler effect to be taken into account.

5.3.1 Fuel behaviour model

The fuel behaviour model uses the same radial and axial discretization as the neutronic and thermal-hydraulic models, allowing a one-to-one data transfer between the three solvers. To maintain computational efficiency, each fuel assembly is represented by a single average fuel pin. Consequently, the distinct gadolinium-bearing pins present in Type 02 assemblies are not modeled explicitly. However, the sensitivity study in Appendix E shows that this simplification has a negligible effect on the assembly's average fuel temperature. For this reason, the simplified model without explicit gadolinium is adopted for the whole-core simulations.

In the definition of the pellet properties, an internal gas pressure of 12.8 MPa is assumed, together with a gap gas composition entirely consisting of helium. Moreover, a pellet density of 95.1% is considered [40].

5.3.2 Results of neutronics, thermal-hydraulics and fuel behaviour coupling

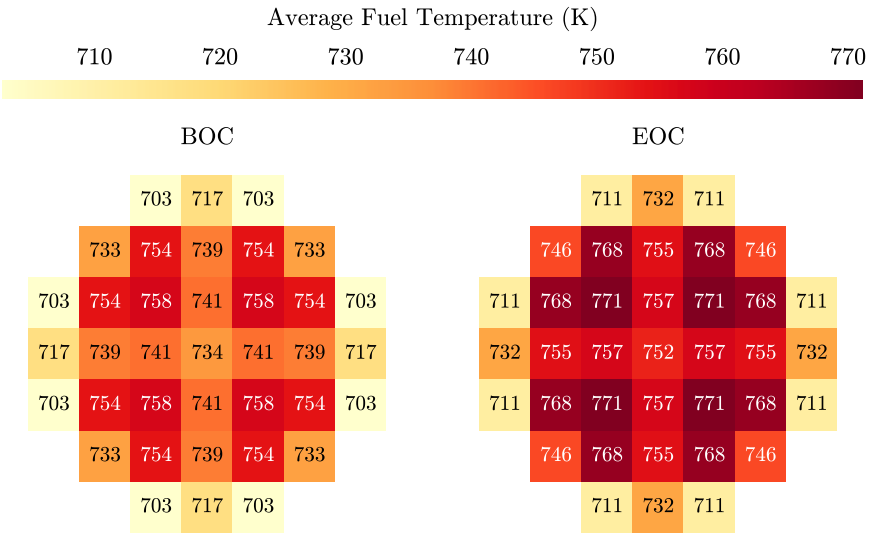


Figure 5.13: Radial fuel temperature distribution at equilibrium cycle.

Figure 5.13 shows the radial distribution of the assembly-averaged fuel temperature at BOC and EOC under equilibrium cycle conditions. As expected, the fuel temperature increases from BOC to EOC, mainly due to the degradation of the fuel thermal conductivity. Although the reported temperatures appear relatively low, it should be noted that they represent fuel temperatures averaged over the entire active assembly, both axially and radially.

Figure 5.14 shows the average axial power distribution for the three simulations. Adding the fuel behaviour model does not significantly change the axial power profile.

This shows that moderator density feedback has the largest effect on the axial power distribution, while Doppler feedback has only a negligible effect.

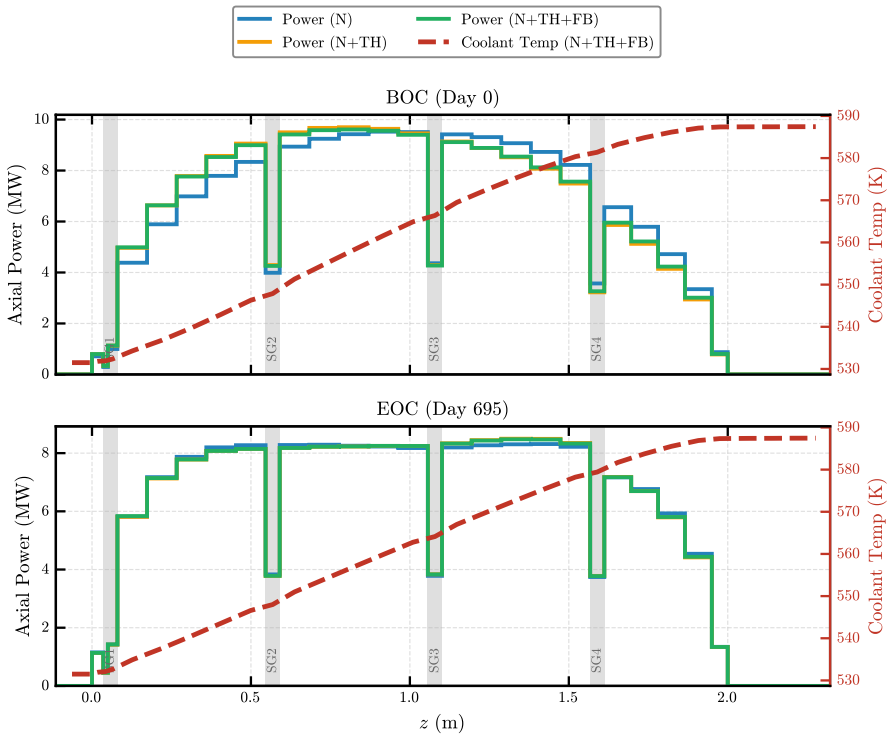


Figure 5.14: Axial power and coolant distribution at equilibrium cycle at the beginning and end of the cycle.

The most significant impact of the fully coupled multiphysics model is observed on the reactivity. Figure 5.15 compares the critical boron concentration over the equilibrium cycle for the three simulation configurations: standalone neutronics, coupled neutronics and thermal hydraulics, and the fully coupled neutronics, thermal hydraulics, and fuel behavior model.

The simulation including the fuel behavior model produces a critical boron concentration trend that is very similar to the standalone neutronics case. Compared with the coupled neutronics and thermal-hydraulics simulation, a higher boron concentration is required to maintain criticality. This behavior is mainly due to the lower fuel temperatures predicted by the fuel behaviour solver. As discussed above, the assembly-averaged fuel temperature is lower than the constant value of 900 K. Lower fuel temperatures reduce Doppler broadening and therefore weaken the Doppler feedback. As a result, fewer neutrons are absorbed by resonance reactions and more neutrons reach thermal energies, increasing the reactivity, in accordance with the DTC. A higher boron concentration is therefore required to maintain critical conditions.

The similar trend between the standalone neutronics and fully coupled simulations is due to two compensating effects. In the standalone case, the fuel temperature is higher than in the fully coupled simulation. This results in stronger Doppler feedback

and lower reactivity. However, the prescribed coolant temperature is lower, which increases the coolant density and improves neutron moderation, leading to higher reactivity. These two effects partially compensate each other, resulting in a critical boron concentration close to that of the fully coupled case.

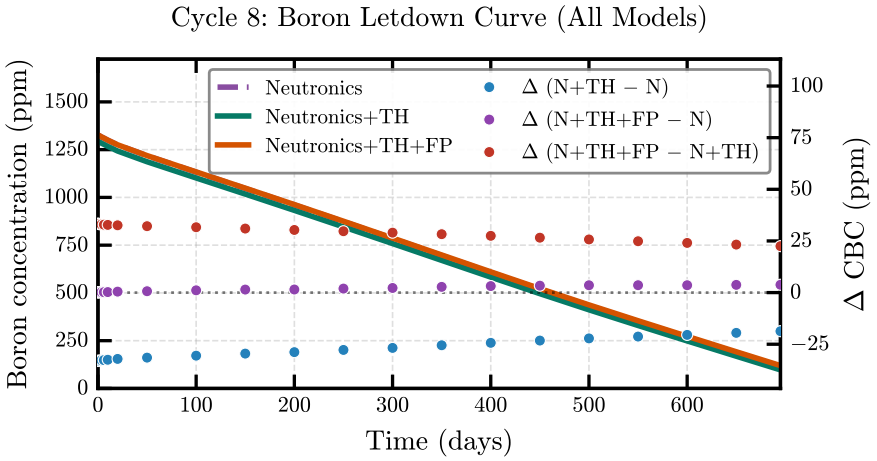


Figure 5.15: Critical boron concentration comparison at equilibrium cycle.

It should be noted that this comparison depends on the boundary conditions assumed in the standalone and coupled simulations. Different prescribed fuel and coolant temperatures would lead to different results. The main advantage of the multiphysics approach is that these quantities are not prescribed but calculated through coupling the different physical models. This allows the evolution of fuel and coolant temperatures, burnup, and radial and axial power distributions to be consistently calculated and their mutual effects to be captured.

Figure 5.16 shows the absolute radial assembly power distribution for the fully coupled case, alongside the relative percentage difference compared to the standalone neutronic simulation. Consistent with the N+TH analysis, the spatial power distribution changes are relatively small but correlated with the local feedback mechanisms. At BOC, the peripheral assemblies (which operate at lower temperatures) exhibit a power increase of up to 2.2% compared to the standalone case. This outward power shift occurs because these cooler regions experience a weaker Doppler feedback, leading to a localized increase in reactivity. Similarly to what is observed in the N+TH case, the magnitude of these spatial discrepancies decreases by EOC (maximum difference of +1.2%). Fuel depletion drives this reduction.

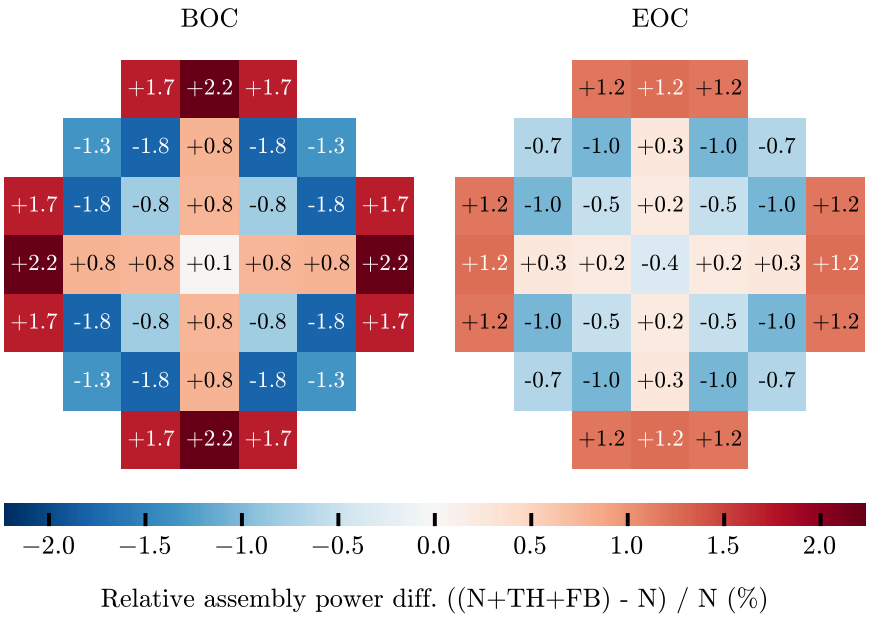


Figure 5.16: Assembly power relative difference (%) between N+TH+FB and N, at BOC (left) and EOC (right).

Chapter 6

Uncertainty quantification

This chapter presents the uncertainty quantification of the first depletion cycle. The main objective is to identify the most important sources of input uncertainty and evaluate their effect on the simulation results. The analysis follows the Best Estimate Plus Uncertainty approach, which aims to reduce unnecessary conservatism in safety margins by providing a more accurate estimate of the results together with their associated uncertainties.

The main sources of uncertainty, which most studies have focused on, are nuclear data, manufacturing tolerances, and thermal-hydraulic input parameters [56, 57, 15]. However, propagating nuclear data uncertainties requires high computational effort. For this reason, this chapter focuses on uncertainty in the most relevant input parameters used by the Ants and Kharon solvers. Specifically, core power, coolant flow rate, system pressure, and inlet temperature are perturbed to evaluate the sensitivity of the coupled model.

To propagate the input uncertainties to the final results, Random Sampling (RS) is adopted. Assuming that the uncertainty associated with each input quantity is characterized by a known standard deviation and probability distribution, RS consists of generating a large set of (N) samples for each input quantity and performing (N) simulations [57]. Finally, the sample average $(\bar{x})$ and the variance (σ^2) of the output quantity are calculated from the resulting samples:

$$\sigma^2 = \frac{1}{N-1}\sum_{i=1}^{N}(x_i - \bar{x})^2 \tag{6.1}$$

where x_i represents the output response of the $i-th$ simulation. The standard deviation, i.e. the uncertainty, is then obtained as the square root of the variance.

Table 6.1 reports the perturbed input parameters and their associated uncertainties. The uncertainty values assigned to each parameter are based on previous analyses reported in the literature [58]. When no uncertainty information is available, a relative standard deviation of 1.0% with a normal distribution is assumed for the input perturbation [15].

Table 6.1: The Uncertain Parameters and their Statistical Information.

Parameters	Distribution	Nominal	Range
Core power	Normal	160 MW	[0.98, 1.02]
Mass Flow rate	Normal	587.15 kg/s	[0.96, 1.04]
Outlet pressure	Normal	12.814 MPa	[0.98, 1.02]
Inlet coolant temperature	Normal	531.5 K	[0.99, 1.01]

To assess the impact of the selected input uncertainties, the parameters in Table 6.1 are perturbed both individually, to evaluate their separate effects, and simultaneously, to assess their combined impact. For each case, 300 samples are generated, resulting in 300 coupled neutronics and thermal-hydraulics simulations. It is important to note that the variation ranges specified in Table 6.1 correspond to a $\pm 2\sigma$ interval. Furthermore, to prevent sampling physically infeasible conditions, the normal distributions are truncated. Figure 6.1 shows the distributions of the uncertain input variables.

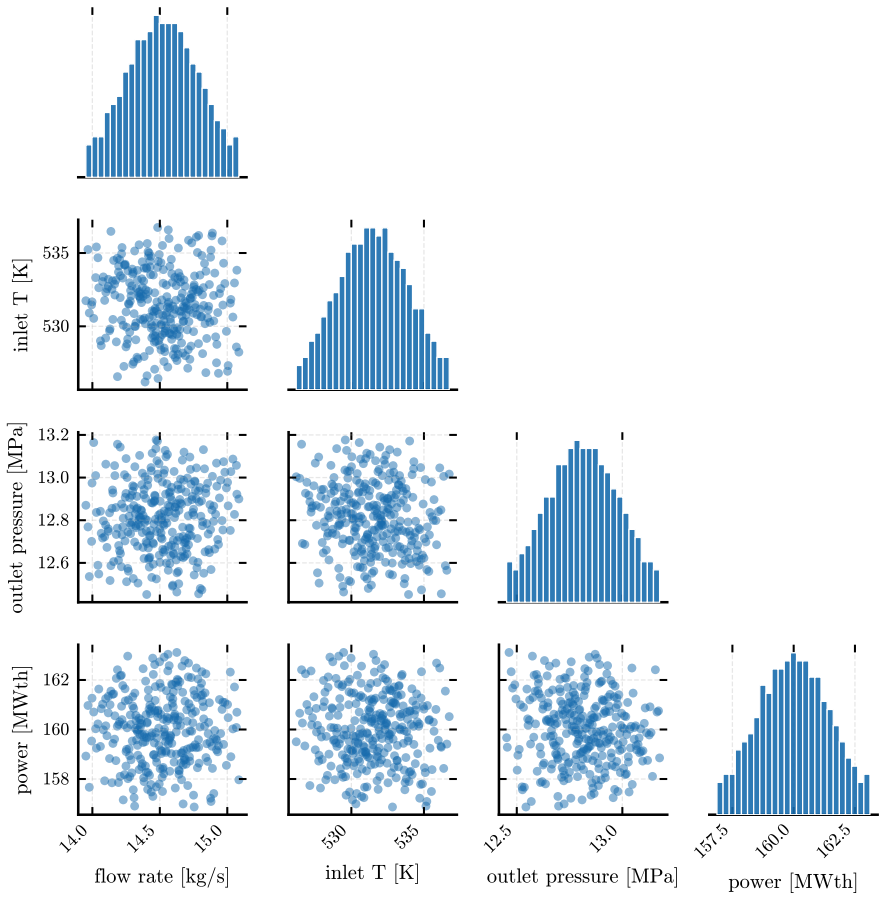


Figure 6.1: Corner plot of the sampled input parameters for the uncertainty quantification analysis.

Figure 6.2 shows the sample standard deviation of the critical boron concentration

at the last burnup step (day 695) as a function of the number of realizations for the four uncertainty cases. The standard deviation becomes stable before $N = 300$, while the percentile realtive standard deviation of the sample mean remains below 1% in all cases. Therefore, 300 realizations are sufficient for statistical convergence.

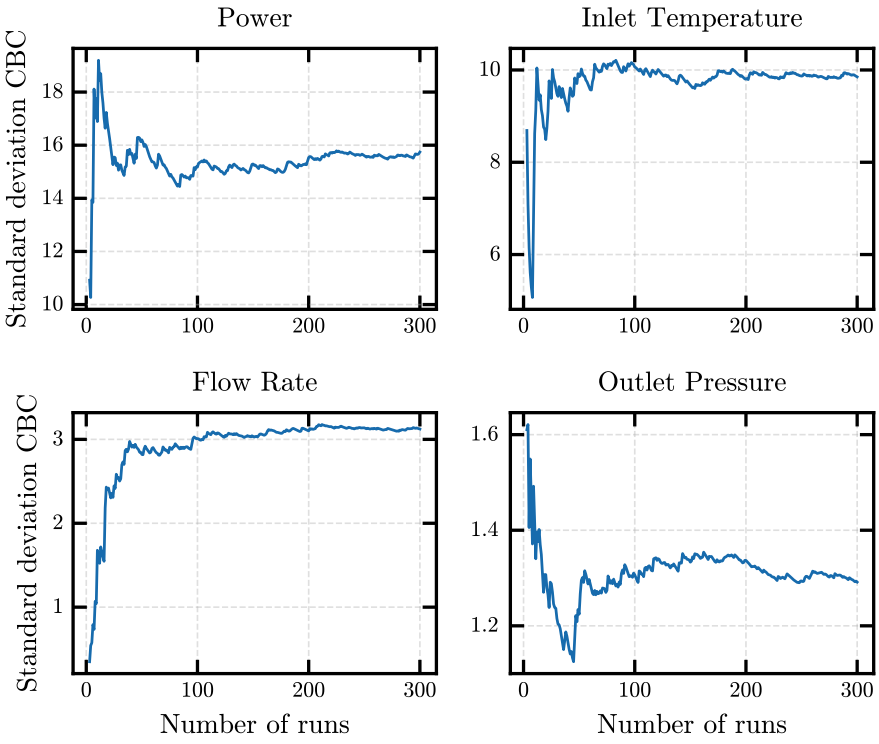


Figure 6.2: Standard deviation convergence at day 695.

6.1 UQ Results

Table 6.2 reports the standard deviation of the critical boron concentration as a function of burnup for each of the four input parameters, considered separately.

For the power uncertainty, the standard deviation starts at about 3 pcm and increases with burnup. When only the neutronics model is considered, the standard deviation is zero. This indicates that the initial spread is mainly caused by the moderator density feedback. It should be noted that the Doppler feedback is not included in this case, since the analysis uses a coupled neutronics and thermal-hydraulics simulation. After Day 0, the standard deviation increases with burnup. Different power levels lead to different fuel depletion rates, causing the isotopic inventories to diverge between realizations, mainly due to U-235 consumption and Pu-239 production.

Table 6.2: Sample standard deviation of the critical boron concentration [ppm] as a function of burnup, for each uncertainty propagation case.

Day	Std. dev. of boron concentration [ppm]			
	Power	Inlet Temp.	Flow Rate	Outlet Press.
0	3.36	16.02	6.22	3.15
100	5.70	14.32	5.48	2.73
200	7.93	13.82	5.16	2.52
300	9.83	12.87	4.58	2.15
400	11.54	11.93	4.07	1.84
500	13.07	11.14	3.68	1.61
600	14.47	10.45	3.37	1.43
695	15.74	9.85	3.12	1.29

Figure 6.3 shows the relationship between thermal power and critical boron concentration at Day 0 and Day 695. In both cases, the relationship is linear, with a Pearson correlation coefficient of $r = -1.0$. At Day 0, higher power increases the coolant temperature, reducing moderator density and reactivity. Therefore, less boron is needed to compensate for the reactivity loss. At Day 695, the same moderator feedback is combined with the effect of fuel depletion: higher power causes faster burnup and a lower residual fissile inventory, further reducing the critical boron concentration.

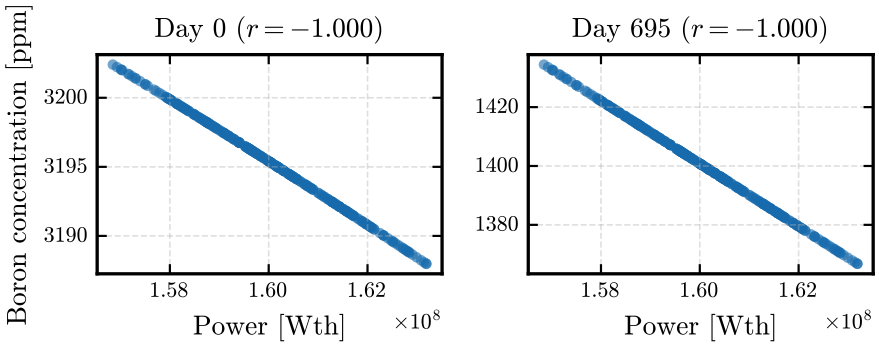


Figure 6.3: Critical boron concentration versus thermal power across the 300 realizations of the power uncertainty propagation case, evaluated at BOC and EOC.

The outlet pressure, inlet temperature, and flow rate directly affect the moderator density feedback. Figure 6.4 shows the critical boron concentration at BOC, where the standard deviation is highest, as a function of inlet temperature, flow rate, and outlet pressure, with each parameter perturbed separately. Higher inlet temperature reduces moderator density and therefore requires less boron, resulting in a negative correlation. Higher flow rate improves heat removal, reducing coolant temperature and increasing the required boron concentration. Finally, higher pressure increases

coolant density, leading to a higher boron concentration. The latter two effects therefore show a positive correlation.

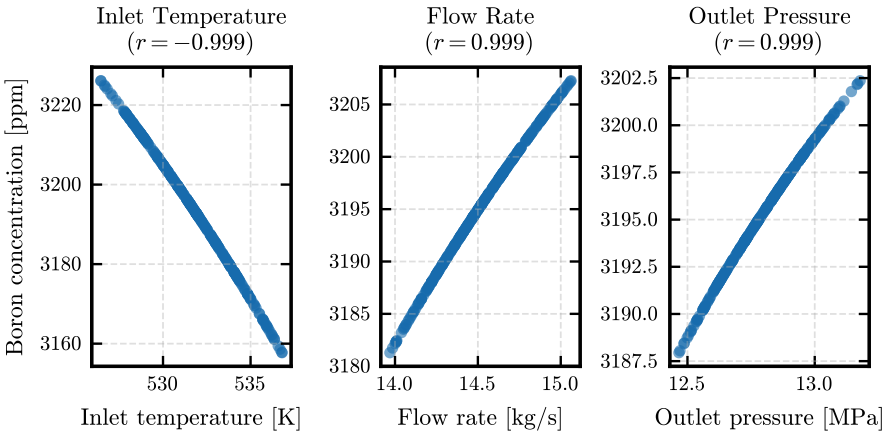


Figure 6.4: Critical boron concentration at Day 0 versus inlet temperature, flow rate, and outlet pressure, across the 300 realizations of the respective uncertainty propagation cases.

For pressure, the standard deviation is low because, in a PWR, coolant density is only weakly affected by pressure variations. Since the moderator density feedback depends on coolant density, a pressure perturbation causes only a small change in density and, consequently, in reactivity. In contrast, flow rate, and especially temperature, have a stronger effect on coolant density and therefore result in a larger standard deviation.

The decrease in standard deviation with burnup in all three cases is likely due to fuel depletion. At the beginning of the cycle, reactivity is mainly affected by moderator feedback, making its contribution more significant. As burnup increases, fuel depletion also affects reactivity, reducing the relative importance of moderator feedback and, consequently, the associated uncertainty.

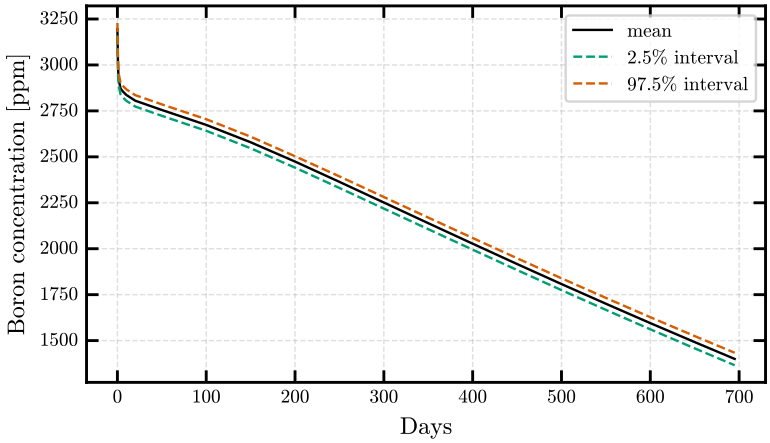


Figure 6.5: Evaluation of the critical boron concentration and its uncertainty.

Figure 6.5 shows the mean critical boron concentration and its 95% confidence interval when all four input parameters are perturbed simultaneously. Table 6.3 compares the standard deviation obtained from the independent simulations, where one parameter is perturbed at a time, with the standard deviation obtained from the simultaneous perturbation of all parameters. The total standard deviation of the independent perturbation is calculated as the root-sum-square of the standard deviations obtained from the four single-parameter simulations.

Table 6.3: Comparison between the standard deviations obtained from the independent perturbation simulations and the standard deviation obtained from the simultaneous perturbation case.

Day	Indipendent perturbation [ppm]	Simultaneous perturbation [ppm]
0	17.79	18.10
100	16.58	16.67
200	16.94	16.82
300	16.97	16.63
400	17.19	16.66
500	17.63	16.94
600	18.22	17.40
695	18.87	17.96

Chapter 7

Conclusion

This thesis presented the analysis of a 3D whole-core multiphysics model for a NuScale-like Small Modular Reactor within the Kraken computational framework. The primary objective was to investigate the effect of progressively coupling the thermal-hydraulics (Kharon) and fuel thermo-mechanical (SuperFINIX) models with the neutronics (Ants) model. The impact on the core neutronic behaviour and the critical boron concentration letdown curve was then evaluated. An uncertainty quantification (UQ) analysis was also performed using the Best Estimate Plus Uncertainty approach.

7.1 Key Findings

First, two-group macroscopic cross-section libraries were generated with the Monte Carlo code Serpent2. The results were verified at the single-assembly infinite-lattice level. Agreement was good at zero burnup, while larger differences appeared at higher burnup, especially in the blanket regions. These differences are mainly due to the burnup discretization used in the Serpent simulation. At the whole-core level, standalone Ants simulations reproduced the 3-batch equilibrium cycle after eight depletion cycles. Comparison with a whole-core Serpent calculation showed a CBC difference below 20 ppm and a maximum assembly power error below 2%.

The thermal-hydraulic coupling was then introduced using Kharon. This replaced the uniform moderator conditions. At BOC, this resulted in a reactivity decrease of about 255 pcm (ΔCBC $\approx$ 33 ppm). This was mainly caused by the higher average coolant temperature in the core. The axial power distribution also changed, with a power peak in the lower core at BOC due to higher water density in the lower plenum.

SuperFINIX was then added to calculate the fuel temperature distribution and gap conductance. The assembly-averaged fuel temperature in the active core was about 700–770 K, which is lower than the uniform 900 K assumed in the standalone neutronics model. The lower fuel temperature reduced the Doppler effect and introduced a positive reactivity feedback. This partially compensated for the negative

moderator density feedback. As a result, the CBC letdown curve of the fully coupled model remained close to that of the standalone neutronics model. This shows that the effects of the different physical models can partly compensate for each other. Despite this, the results show the importance of multiphysics simulations, which reduce the need for approximate assumptions.

Finally, an uncertainty quantification analysis was performed using 300 random samples. The analysis considered uncertainties in core power, flow rate, inlet temperature, and outlet pressure and evaluated their effect on the CBC. The inlet coolant temperature and thermal power had the largest effect on the results. The overall standard deviation was about 18 ppm at both BOC and EOC.

7.2 Future Work

Several aspects of the modelling can be further developed in future studies. In particular, the current thermal-hydraulic model uses a fixed inlet mass flow rate. Coupling the core model with a plant system code would allow the natural circulation flow rate and pressure losses in the primary loop to be calculated based on the operating conditions of the system. Another possible improvement is the use of an open-lattice subchannel model. Kharon currently uses a closed-channel model. An open-lattice subchannel solver could improve the modelling of local thermal-hydraulic conditions.

Further work could also consider pin-by-pin power reconstruction and more detailed modelling of gadolinia-bearing pins in SuperFINIX. Although the assembly-averaged model was found to be adequate, these approaches could be useful for more detailed safety analyses.

In addition, although the Serpent-Ants comparison already shows good agreement, using a finer burnup discretization in the two-step calculation could further improve the accuracy.

Finally, the BEPU analysis could be extended to include nuclear data and geometric uncertainties, in addition to uncertainties in the operational parameters. However, the computational cost should also be considered. To propagate these uncertainties while keeping the two-step approach, at least 300 Serpent simulations would be required for each homogenized region, making the calculation computationally expensive.

Appendix A

Material compositions

The material compositions used in the Nuscale-like model are reported.

Table A.1: Nuclide compositions of all fuel types [atoms/barn-cm].

	Assembly 01		Assembly 02			Assembly 03
Nuclide	4.05 wt%	3.24 wt%	4.55 wt%	3.64 wt%	4.55 wt% + Gd	2.60 wt%
U-235	9.62361E-04	7.69898E-04	1.08116E-03	8.64942E-04	1.05327E-03	6.17826E-04
U-238	2.25117E-02	2.27020E-02	2.23942E-02	2.26080E-02	2.18164E-02	2.28524E-02
O-16	4.69438E-02	4.69438E-02	4.69507E-02	4.69459E-02	4.67818E-02	4.69404E-02
Gd-152	–	–	–	–	1.39006E-06	–
Gd-154	–	–	–	–	1.51516E-05	–
Gd-155	–	–	–	–	1.02864E-04	–
Gd-156	–	–	–	–	1.42272E-04	–
Gd-157	–	–	–	–	1.08772E-04	–
Gd-158	–	–	–	–	1.72645E-04	–
Gd-160	–	–	–	–	1.51933E-04	–

Table A.2: Volume fractions of the homogeneous mixtures [41].

Homogeneous mixture	**Constituent**	**Volume fraction**
Heavy reflector	304L SS	0.956
	Coolant	0.044
Bottom nozzle	304L SS	0.172
	Coolant	0.828
Top nozzle	304L SS	0.177
	Coolant	0.823

Table A.3: Nuclide compositions of structural materials, control rod absorber material, and fill gas. Number densities are given in units of 1/(barn·cm) [41].

Zr-4		**Inconel**		**304L SS**	
Nuclide	ND	Nuclide	ND	Nuclide	ND
Cr-50	3.29620E-06	Cr-50	7.82390E-04	Cr-50	7.67780E-04
Cr-52	6.35640E-05	Cr-52	1.50880E-02	Cr-52	1.48060E-02
Cr-53	7.20760E-06	Cr-53	1.71080E-03	Cr-53	1.67890E-03
Cr-54	1.79410E-06	Cr-54	4.25860E-04	Cr-54	4.17910E-04
Fe-54	8.66980E-06	Fe-54	1.47970E-03	Fe-54	3.46200E-03
Fe-56	1.36100E-04	Fe-56	2.32290E-02	Fe-56	5.43450E-02
Fe-57	3.14310E-06	Fe-57	5.36450E-04	Fe-57	1.25510E-03
Fe-58	4.18290E-07	Fe-58	7.13920E-05	Fe-58	1.67030E-04
O-16	3.07440E-04	Mn-55	7.82010E-04	Mn-55	1.76040E-03
O-17	1.16800E-07	Ni-58	2.93200E-02	Ni-58	5.60890E-03
Sn-112	4.67350E-06	Ni-60	1.12940E-02	Ni-60	2.16050E-03
Sn-114	3.17990E-06	Ni-61	4.90940E-04	Ni-61	9.39170E-05
Sn-115	1.63810E-06	Ni-62	1.56530E-03	Ni-62	2.99450E-04
Sn-116	7.00550E-05	Ni-64	3.98640E-04	Ni-64	7.62610E-05
Sn-117	3.70030E-05	Si-28	5.67570E-04	Si-28	9.52810E-04
Sn-118	1.16690E-04	Si-29	2.88200E-05	Si-29	4.83810E-05
Sn-119	4.13870E-05	Si-30	1.89980E-05	Si-30	3.18930E-05
Sn-120	1.56970E-04				
Sn-122	2.23080E-05				
Sn-124	2.78970E-05				
Zr-90	2.18280E-02				
Zr-91	4.76010E-03				
Zr-92	7.27590E-03				
Zr-94	7.37340E-03				
Zr-96	1.18790E-03				
AIC (80–15–5)		**Helium**		**M5R**	
Nuclide	ND	Nuclide	ND	Nuclide	ND
Ag-107	2.35230E-02	He-3	4.80890E-10	O-16	7.36780E-03
Ag-109	2.18540E-02	He-4	2.40440E-04	Zr-90	5.12902E-01
Cd-106	3.38820E-05			Zr-91	1.10620E-01
Cd-108	2.41660E-05			Zr-92	1.67246E-01
Cd-110	3.39360E-04			Zr-94	1.65877E-01
Cd-111	3.48210E-04			Zr-96	2.61658E-02
Cd-112	6.56110E-04			S-32	6.05612E-05
Cd-113	3.32750E-04			S-33	4.70154E-07
Cd-114	7.82520E-04			S-34	2.57600E-06
Cd-116	2.04430E-04			S-36	1.13419E-08
In-113	3.42190E-04			Nb-93	9.75767E-03
In-115	7.65110E-03				

Appendix B

Evolution of Neutron Poisons

This appendix provides a comparison of the short-lived neutron poisons (^{135}Xe and ^{149}Sm) evaluated by Serpent and Ants for the upper blanket region. The plots include results from both the standard 28-step simulation and the refined 52-step simulation discussed in Section 4.5.

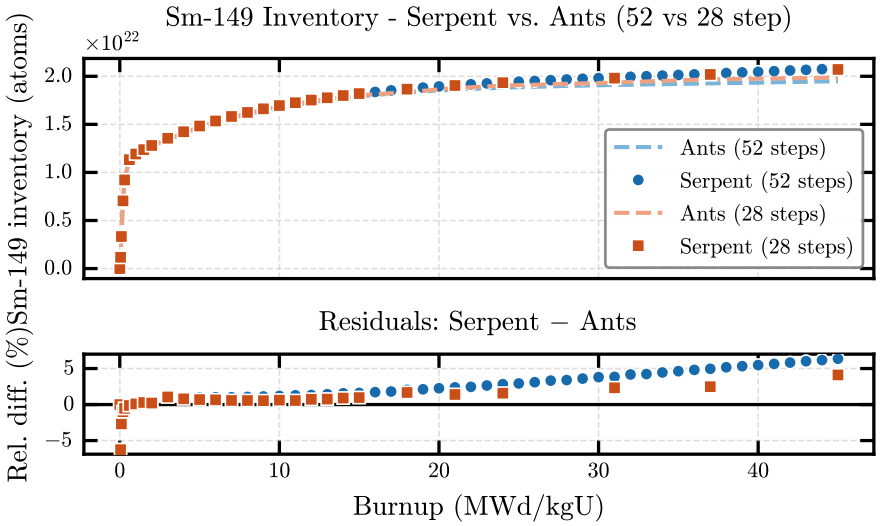


Figure B.1: Evolution of Samarium-149 number density in the upper blanket during depletion. The plot compares the reference Monte Carlo solution (Serpent) against the deterministic nodal solver (Ants) using two different temporal discretizations (28 and 52 burnup steps). The relative difference in the bottom panel is computed as $\frac{\text{Serpent}-\text{ANTS}}{\text{Serpent}}$.

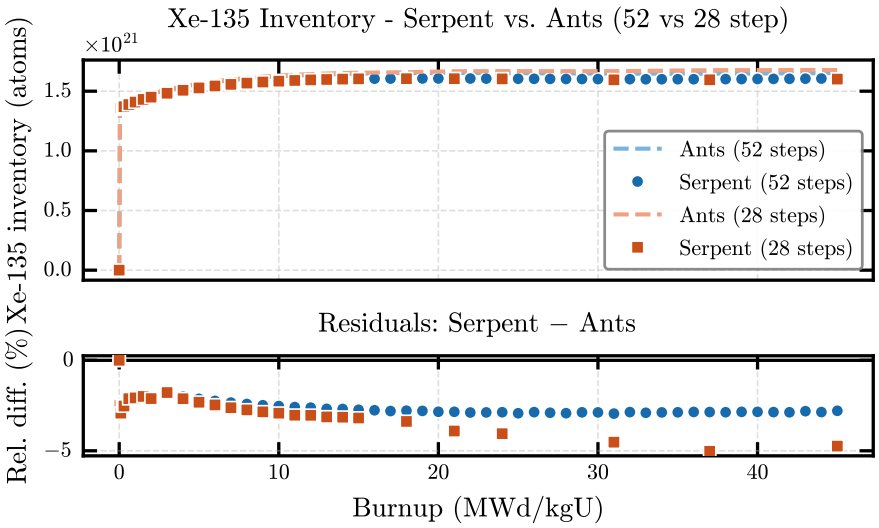


Figure B.2: Evolution of Xenon-135 number density in the upper blanket during depletion. The plot compares the reference Monte Carlo solution (Serpent) against the deterministic nodal solver (Ants) using two different temporal discretizations (28 and 52 burnup steps). The relative difference in the bottom panel is computed as $\frac{\text{Serpent}-\text{ANTS}}{\text{Serpent}}$.

Figures B.1 and B.2 highlight that increasing the number of burnup steps at higher burnups does not significantly alter the predicted poison concentrations.

As expected, the ^{135}Xe concentration (Figure B.2) increases rapidly during the first burnup steps until equilibrium is reached. Both the 28-step and 52-step Ants models consistently overestimate the Xenon concentration throughout the entire depletion cycle compared to Serpent.

Similarly, for ^{149}Sm (Figure B.1), Ants initially overestimates the concentration. As depletion progresses, the trend reverses, leading to a slight underestimation of Samarium at higher burnups.

As discussed in the main text, since these strong neutron absorbers are only sensitive to the temporal discretization of the very first few burnup steps, adding refinement at later depletion stages (the 52-step model) fails to correct their initial overestimation, which remains the primary cause of the initial k_∞ underestimation.

Appendix C

Sensitivity of the thermal-hydraulic model

To assess the influence of the nozzle hydraulic diameter and of the associated pressure drop on the core flow parameters, two sets of simulations are performed: in the first, the nozzle hydraulic diameter is varied by one order of magnitude; in the second, the axial length of the inactive region is modified to tune the pressure drop.

Table C.1: Sensitivity of the pressure drop to the axial dimension treatment.

True axial dimension	**Dh [m]**	Δp **[Pa]**	**Variation [Pa]**
reference	0.0111	17907	-
yes	1	17860	-47
yes	0.005	17959	+52
no	0.0111	17386	-521
no	0.0111	18714	+807

Varying the nozzle hydraulic diameter by one order of magnitude changes the inlet–outlet pressure drop by only $\sim$50 Pa, with coolant temperature and density profiles remaining essentially unchanged (Figure C.1). Similarly, changing the axial length of the non-active region changes the pressure drop by only a few hundred pascals (Table C.1), with no significant effect on the coolant properties(Figure C.2). This confirms that, for a fixed inlet flow rate and outlet pressure, the geometrical approximations in the nozzle and non-active regions have little effect on the core thermal-hydraulic results.

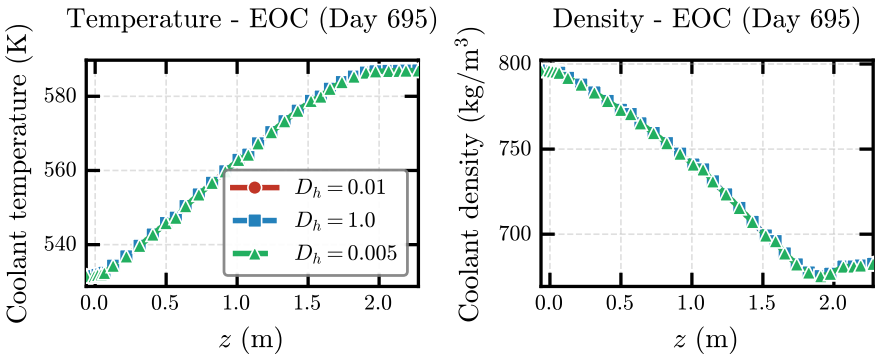


Figure C.1: Comparison of axial coolant density and temperature profile at EOC with different D_h.

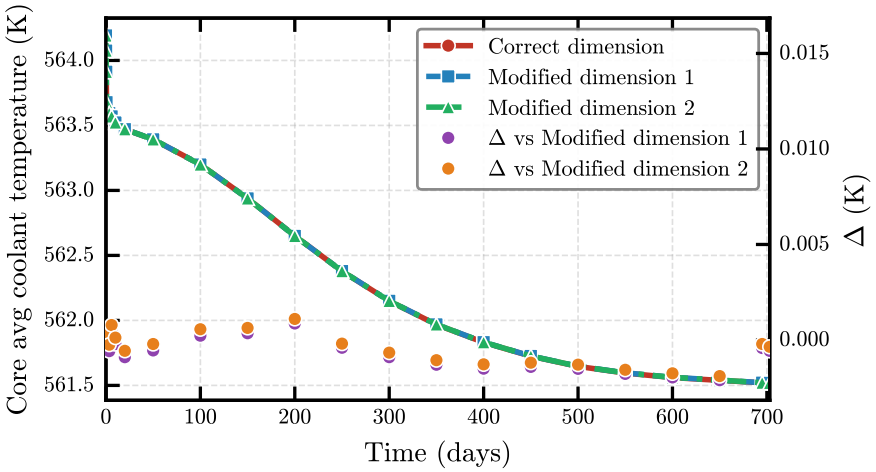


Figure C.2: Comparison of the average coolant temperature with modified axial dimensions.

Appendix D

Comparison with NuScale FSAR: Relative Assembly Power Distribution

Figure D.1 shows the comparison of the radial relative power distribution at BOC and EOC with the FSAR reference [39]. Overall, good agreement is observed. The largest differences occur in the assemblies containing gadolinium.

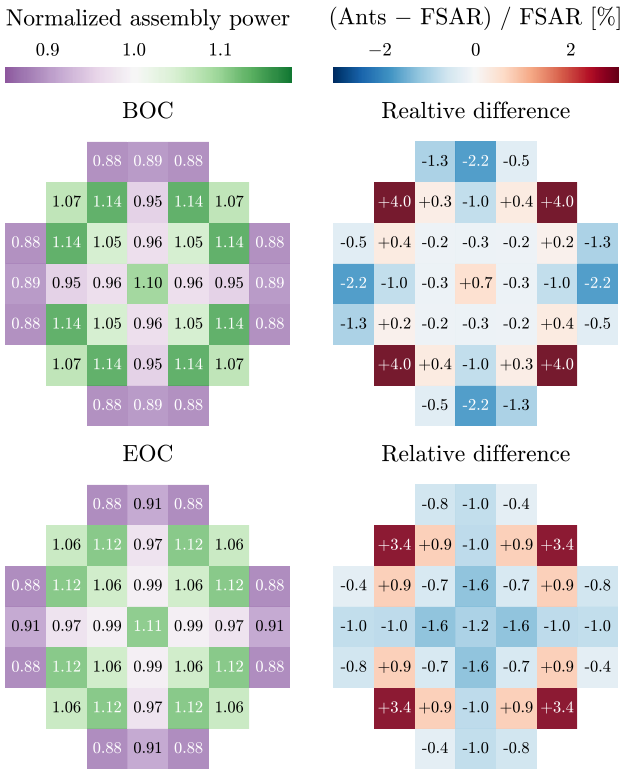


Figure D.1: Comparison of radial relative power distributions at BOC and EOC with the NuScale FSAR reference.

Appendix E

Sensitivity of fuel behaviour to gadolinium homogenization

The fuel behaviour model described in Section 5.3.1 represents each fuel assembly using a single average fuel pin. As a result, the gadolinium concentration is assumed to be zero. A more detailed approach could model each pin individually, allowing the pins with gadolinium to be explicitly represented. However, this would significantly increase the computational cost and is therefore not adopted in the present work.

To verify that this simplification does not compromise the accuracy of the assembly-averaged fuel temperature, three simulations are performed:

- GD_0.0_all: reference case without Gd.
- GD_0.02_4: actual geometry and composition, Gd present only in the four Gd-bearing pins at the nominal weight fraction of 2%.
- GD_0.8_4: Gd included only in the four Gd-bearing pins, at an artificially high weight fraction of 80%, to stress-test the local thermal effect.

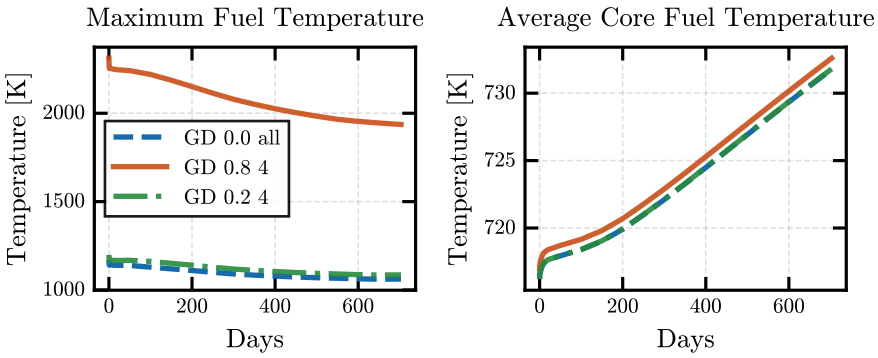


Figure E.1: Max and average fuel temperature comparison.

Figure E.1 compares the maximum and average fuel temperature during the first cycle. The maximum fuel temperature is evaluated at the centerline of an individual

fuel pin. As expected, the unrealistic 80%-in-all-pins case shows a large increase in maximum temperature, due to the lower thermal conductivity of Gd-bearing fuel, which reduces heat removal from the pellet. For the nominal case (2% in 4 pins), this effect is much smaller. The average fuel temperature is instead almost unchanged compared to the no-Gd case, even for the 80%-in-4-pins case, since Gd is present only in a small fraction of the total fuel volume.

The quantity used for the multiphysics coupling is the assembly-averaged fuel temperature passed from SuperFINIX to Ants. Figure E.2 shows the difference in this temperature between the no-Gd case and the nominal Gd case (GD_0.02_4). The difference is negligible across the core, confirming that Ants receives essentially the same fuel temperature field in both cases.

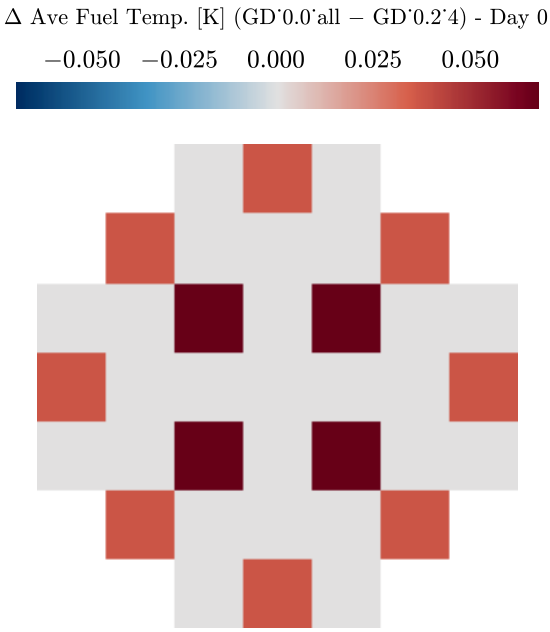


Figure E.2: Max assembly fuel temperature difference.

Since the objective of the full-core multiphysics simulation is the prediction of whole level and assembly-level quantities rather than the detailed thermal behaviour of individual fuel pins, this negligible sensitivity justifies neglecting the explicit representation of gadolinium pins in the fuel behaviour model, as adopted in Section 5.3.1.

Bibliography

[1] ANSYS, Inc. *What is Multiphysics?* URL: https://www.ansys.com/simulation-topics/what-is-multiphysics (visited on 03/18/2026) (cit. on p. 1).

[2] Gregory K. Delipei, Quentin Faure, Maria Avramova, and Kostadin Ivanov. «High-fidelity multi-physics guidelines for model validation and uncertainty quantification». In: *Frontiers in Nuclear Engineering* 4 (2026), p. 1720142. DOI: 10.3389/fnuen.2025.1720142. URL: https://doi.org/10.3389/fnuen.2025.1720142 (cit. on p. 1).

[3] Yugao Ma, Shichang Liu, Zhen Luo, Shanfang Huang, Kaiwen Li, Kan Wang, Ganglin Yu, and Hongxing Yu. «RMC/CTF multiphysics solutions to VERA core physics benchmark problem 9». In: *Annals of Nuclear Energy* 133 (2019), pp. 837–852. DOI: 10.1016/j.anucene.2019.07.033 (cit. on p. 1).

[4] Jason Hou, Maria Avramova, and Kostadin Ivanov. «Best-Estimate Plus Uncertainty Framework for Multiscale, Multiphysics Light Water Reactor Core Analysis». In: *Science and Technology of Nuclear Installations* 2020 (2020), p. 7526864. DOI: 10.1155/2020/7526864 (cit. on pp. 1, 3).

[5] F. D'Auria. «Best Estimate Plus Uncertainty (BEPU): Status and perspectives». In: *Nuclear Engineering and Design* 352 (2019), p. 110190. DOI: 10.1016/j.nucengdes.2019.110190 (cit. on p. 1).

[6] Pouria Kakaei, Mahdi Zangian, and M. Abbasi. «Multi-physics core analysis and verification of NuScale reactor with coupling PARCS/RELAP». In: *Annals of Nuclear Energy* 193 (2023), p. 110021. DOI: 10.1016/j.anucene.2023.110021 (cit. on pp. 2, 3).

[7] Taesuk Oh, Yunseok Jeong, Husam Khalefih, and Yonghee Kim. «Development and validation of multiphysics PWR core simulator KANT». In: *Nuclear Engineering and Technology* 55 (2023), pp. 2230–2245. DOI: 10.1016/j.net.2023.02.025 (cit. on p. 2).

[8] Yan Liu, Guolian Wang, Hui He, Tengfei Zhang, and Xiaojing Liu. «Pressurized water reactor fuel corrosion-related unidentified deposit and its related safety issues – III. N-TH-M coupled CIPS prediction». In: *Annals of Nuclear Energy* 208 (2024), p. 110800. DOI: 10.1016/j.anucene.2024.110800 (cit. on pp. 2, 3).

[9] Minghui Weng, Shichang Liu, Zhenhai Liu, Feipeng Qi, Yi Zhou, and Yixue Chen. «Development and application of Monte Carlo and COMSOL coupling code for neutronics/thermohydraulics coupled analysis». In: *Annals of Nuclear Energy* 161 (2021), p. 108459. DOI: 10.1016/j.anucene.2021.108459 (cit. on p. 2).

[10] Shanfang Huang et al. «A review of Monte Carlo-based multiphysics coupling in nuclear reactor analysis». In: *Progress in Nuclear Energy* 192 (2026), p. 106178. DOI: 10.1016/j.pnucene.2025.106178 (cit. on p. 3).

[11] Juan Carlos Almachi, Victor Sánchez-Espinoza, Uwe Imke, Robert Stieglitz, and Marat Margulis. «Validation of the dynamic simulation capabilities of Serpent2/Subchanflow using experimental data from the research reactor SPERT IV D-12/25». In: *Nuclear Engineering and Design* 418 (2024), p. 112840. DOI: 10.1016/j.nucengdes.2023.112840 (cit. on p. 3).

[12] Seddon Atkinson, Anna Detkina, Dzianis Litskevich, and Bruno Merk. «A Comparison of Advanced Boiling Water Reactor Simulations between Serpent/CTF and Polaris/DYN3D: Steady State Operational Characteristics and Burnup Evolution». In: *Energies* 14 (2021), p. 838. DOI: 10.3390/en14040838 (cit. on p. 3).

[13] Ville Rintala, Heikki Suikkanen, Arndt Schubert, and Paul Van Uffelen. «Supplementing fuel behaviour analyses via coupled Monte Carlo neutronics and fission product solution». In: *Nuclear Engineering and Design* 389 (2022), p. 111668. ISSN: 0029-5493. DOI: 10.1016/j.nucengdes.2022.111668 (cit. on p. 3).

[14] Jiankai Yu, Hyunsuk Lee, Matthieu Lemaire, Hanjoo Kim, Peng Zhang, and Deokjung Lee. «MCS based neutronics/thermal-hydraulics/fuel-performance coupling with CTF and FRAPCON». In: *Computer Physics Communications* 238 (2019), pp. 1–18. DOI: 10.1016/j.cpc.2019.01.001 (cit. on p. 3).

[15] Jinsu Park, Yeongseok Kang, and Deokjung Lee. «Uncertainty quantification of steady state depeltion solution using multi-physics coupling code system based on nodal diffusion code RAST-K». In: *Nuclear Engineering and Technology* 57 (2025), p. 103751. DOI: 10.1016/j.net.2025.103751 (cit. on pp. 3, 57).

[16] Cody J. Permann et al. «MOOSE: Enabling massively parallel multiphysics simulation». In: *SoftwareX* 11 (2020), p. 100430. DOI: 10.1016/j.softx.2020.100430 (cit. on p. 3).

[17] John A. Turner, Kevin Clarno, Matt Sieger, Roscoe Bartlett, Benjamin Collins, Roger Pawlowski, Rodney Schmidt, and Randall Summers. «The Virtual Environment for Reactor Applications (VERA): Design and architecture». In: *Journal of Computational Physics* 326 (2016), pp. 544–568. DOI: 10.1016/j.jcp.2016.09.003 (cit. on p. 3).

[18] Jaakko Leppänen et al. «Current Status and On-Going Development of VTT's Kraken Core Physics Computational Framework». In: *Energies* 15.3 (2022), p. 876. DOI: 10.3390/en15030876 (cit. on pp. 3, 15, 22–25).

[19] Jaakko Leppänen, Ville Valtavirta, Antti Rintala, and Riku Tuominen. «Status of Serpent Monte Carlo code in 2024». In: *EPJ Nuclear Sciences and Technologies* 11 (2025), p. 3. DOI: 10.1051/epjn/2024031 (cit. on pp. 4, 23).

[20] Ville Valtavirta and Antti Rintala. «Validating Kraken for VVER-1000 fuel cycle simulations using the X2 benchmark». In: *Annals of Nuclear Energy* 190 (2023), p. 109878. DOI: 10.1016/j.anucene.2023.109878 (cit. on p. 4).

[21] Weston M. Stacey. *Nuclear Reactor Physics*. 2nd. Weinheim: Wiley-VCH, 2007. ISBN: 978-3-527-40679-1 (cit. on pp. 5–7).

[22] Judith F. Briesmeister. *MCNP—A General Monte Carlo N-Particle Transport Code, Version 4C*. Tech. rep. LA-13709-M. Los Alamos, New Mexico: Los Alamos National Laboratory, Mar. 2000 (cit. on p. 6).

[23] K. Devan and Abhitab Bachchan. «Homogeneous reactor and neutron diffusion equation». In: *Physics of Nuclear Reactors*. Elsevier, 2021. Chap. 4, pp. 193–262. DOI: 10.1016/B978-0-12-822441-0.00004-2 (cit. on p. 7).

[24] K. S. Smith. «Assembly homogenization techniques for light water reactor analysis». In: *Progress in Nuclear Energy* 17.3 (1986), pp. 303–335. DOI: 10.1016/0149-1970(86)90035-1 (cit. on pp. 8, 9, 11).

[25] Serpent Developer Team. *Input syntax manual — Serpent Wiki*. URL: https://serpent.vtt.fi/mediawiki/index.php/Input_syntax_manual (visited on 05/20/2024) (cit. on p. 8).

[26] Jaakko Leppänen, Maria Pusa, and Emil Fridman. «Overview of methodology for spatial homogenization in the Serpent 2 Monte Carlo code». In: *Annals of Nuclear Energy* 96 (2016), pp. 126–136. DOI: 10.1016/j.anucene.2016.06.007 (cit. on p. 10).

[27] VTT Technical Research Centre of Finland. *Serpent User Guide: 2.2.5. Group constant generation*. 2026. URL: https://serpent.vtt.fi/docs/user_guide/gc_generation.html (visited on 08/24/2026) (cit. on p. 10).

[28] Zhaoyuan Liu, Kord Smith, Benoit Forget, and Javier Ortensi. «Cumulative migration method for computing rigorous diffusion coefficients and transport cross sections from Monte Carlo». In: *Annals of Nuclear Energy* 112 (2018), pp. 507–516. DOI: 10.1016/j.anucene.2017.10.039 (cit. on p. 10).

[29] Jerzy Cetnar. «General solution of Bateman equations for nuclear transmutations». In: *Annals of Nuclear Energy* 33 (2006), pp. 640–645. DOI: 10.1016/j.anucene.2006.02.004 (cit. on p. 11).

[30] M. Pusa and J. Leppänen. «Computing the Matrix Exponential in Burnup Calculations». In: *Nuclear Science and Engineering* 164.2 (2010), pp. 140–150. DOI: 10.13182/NSE09-14 (cit. on p. 11).

[31] A.E. Isotalo and P.A. Aarnio. «Substep methods for burnup calculations with Bateman solutions». In: *Annals of Nuclear Energy* 38 (2011), pp. 2509–2514. DOI: 10.1016/j.anucene.2011.07.012 (cit. on p. 12).

[32] Mamoru Ishii and Takashi Hibiki. *Thermo-Fluid Dynamics of Two-Phase Flow*. New York, NY, USA: Springer Science & Business Media, 2006. ISBN: 978-0-387-28321-0 (cit. on p. 12).

[33] VTT Technical Research Centre of Finland. *Kharon theory manual*. URL: https://serpent.vtt.fi/kraken/index.php/Kharon_theory_manual (visited on 08/18/2026) (cit. on pp. 13, 24, 25).

[34] Lucid Learning. *Heat Conduction Equation in Cylindrical Coordinates*. URL: https://medium.com/@lucidlearning314/heat-conduction-equation-in-cylindrical-coordinates-3e26402ee1f8 (visited on 08/18/2026) (cit. on p. 14).

[35] Henri Loukusa, Jussi Peltonen, and Ville Valtavirta. *FINIX - Fuel behavior model and interface for multiphysics applications - Code documentation for version 1.19.12*. Research Report VTT-R-01103-19. Espoo, Finland: VTT Technical Research Centre of Finland, Dec. 2019 (cit. on pp. 14, 15, 23, 26).

[36] Nuclear Power. *Doppler Broadening – Doppler Effect*. nuclear-power.com. URL: https://www.nuclear-power.com/glossary/doppler-broadening/ (visited on 10/25/2023) (cit. on p. 15).

[37] Jeffrey Neil Cardoni. «Nuclear Reactor Multi-Physics Simulations with Coupled MCNP5 and STAR-CCM+». MA thesis. Urbana, Illinois: University of Illinois at Urbana-Champaign, 2011 (cit. on p. 15).

[38] NuScale Power, LLC. *NuScale Power - Official Website*. 2024. URL: https://www.nuscalepower.com/ (visited on 05/24/2024) (cit. on p. 17).

[39] NuScale Power, LLC. *NuScale Standard Plant Design Certification Application – Part 2, Tier 2, Chapter Four: Reactor*. Tech. rep. Revision 4.1. NuScale Power, LLC, June 2020 (cit. on pp. 17, 21, 22, 41, 47, 51, 71).

[40] NuScale Power, LLC. *NuScale US460 Plant Standard Design Approval Application – Final Safety Analysis Report, Chapter Four: Reactor*. Tech. rep. Revision 2. NuScale Power, LLC, 2025 (cit. on pp. 17, 52).

[41] Emil Fridman, Yurii Bilodid, and Ville Valtavirta. «Definition of the neutronics benchmark of the NuScale-like core». In: *Nuclear Engineering and Technology* 55 (2023), pp. 3639–3647. DOI: 10.1016/j.net.2023.06.029 (cit. on pp. 17–21, 65, 66).

[42] Una Baker, Marisol Garrouste, Sooyoung Choi, Gabriel J. Soto, Ross Snuggerud, Brendan Kochunas, and Ben Lindley. «Simulation of the NuScale SMR and Investigation of the Effect of Load-following on Component Lifetimes». Unpublished manuscript / Preprint. 2023 (cit. on pp. 17, 21, 46).

[43] M. J. Qin, S. C. Middleburgh, M. W. D. Cooper, M. J. D. Rushton, M. Puide, E. Y. Kuo, R. W. Grimes, and G. R. Lumpkin. «Thermal conductivity variation in uranium dioxide with gadolinia additions». In: *Journal of Nuclear Materials* 540 (2020), p. 152258. DOI: 10.1016/j.jnucmat.2020.152258 (cit. on p. 20).

[44] VTT Technical Research Centre of Finland. *Kraken Computational Framework*. URL: https://serpent.vtt.fi/kraken/index.php/Main_Page (visited on 05/20/2024) (cit. on pp. 22, 24, 25).

[45] Ville Sahlberg and Antti Rintala. «Development and First Results of a New Rectangular Nodal Diffusion Solver of ANTS». In: *PHYSOR 2018: Reactor Physics paving the way towards more efficient systems*. Cancun, Mexico, Apr. 2018, pp. 3861–3871 (cit. on pp. 23, 24).

[46] Jaakko Leppänen, Maria Pusa, and Emil Fridman. «Overview of methodology for spatial homogenization in the Serpent 2 Monte Carlo code». In: *Annals of Nuclear Energy* 96 (2016), pp. 126–136. DOI: 10.1016/j.anucene.2016.06.007 (cit. on p. 23).

[47] Riku Tuominen and Ville Valtavirta. «BEAVRS pin-by-pin calculations with Ants-SUBCHANFLOW-SuperFINIX code system». In: *Annals of Nuclear Energy* 180 (2023), p. 109447. DOI: 10.1016/j.anucene.2022.109447 (cit. on p. 23).

[48] Bangyang Xia and Zhongsheng Xie. «Flux expansion nodal method for solving multigroup neutron diffusion equations in hexagonal-z geometry». In: *Annals of Nuclear Energy* 33 (2006), pp. 370–376. DOI: 10.1016/j.anucene.2005.06.011 (cit. on p. 24).

[49] Topias Kähkönen. «SMR Core Depletion and Spent Fuel Characterization with Nodal Code Ants». In: *Nuclear Science and Engineering* (2026). DOI: 10.1080/00295639.2025.2607273. URL: https://doi.org/10.1080/00295639.2025.2607273 (cit. on p. 27).

[50] Ville Valtavirta and Antti Rintala. *Specifications for the generic polynomial group constant model of Ants*. Research Report VTT-R-00154-21. Espoo, Finland: VTT Technical Research Centre of Finland, 2021 (cit. on p. 29).

[51] Y. Bilodid, D. Kotlyar, M. Margulis, E. Fridman, and E. Shwageraus. «Spectral history model in DYN3D: Verification against coupled Monte-Carlo thermal-hydraulic code BGCore». In: *Annals of Nuclear Energy* 81 (2015), pp. 34–40. DOI: 10.1016/j.anucene.2015.03.030 (cit. on p. 30).

[52] Ville Valtavirta. *Kraken workshop: Group constant generation*. Presentation slides, VTT Technical Research Centre of Finland. Workshop presentation. Apr. 2024 (cit. on pp. 32, 33, 35, 36).

[53] Forrest B. Brown. «On the Use of Shannon Entropy of the Fission Distribution for Assessing Convergence of Monte Carlo Criticality Calculations». In: *Proceedings of the PHYSOR-2006 ANS Topical Meeting on Reactor Physics*. Canadian Nuclear Society. Vancouver, BC, Canada, Sept. 2006, p. C081 (cit. on p. 32).

[54] M. J. Driscoll, T. J. Downar, and E. E. Pilat. *The Linear Reactivity Model for Nuclear Fuel Management*. La Grange Park, Illinois: American Nuclear Society, 1990. ISBN: 0-89448-035-9 (cit. on p. 42).

[55] NuScale Power, LLC. *Subchannel Analysis Methodology*. Tech. rep. TR-0915-17564-NP, Rev. 2. Document: ML18305B218.pdf. Corvallis, Oregon: NuScale Power, LLC, Oct. 2018 (cit. on p. 48).

[56] Alexander Aures, Wolfgang Bernnat, Friederike Bostelmann, Jérémy Bousquet, Bernard Krzykacz-Hausmann, Andreas Pautz, Kiril Velkov, and Winfried Zwermann. «Reactor simulations with nuclear data uncertainties». In: *Nuclear Engineering and Design* 355 (2019), p. 110313. DOI: 10.1016/j.nucengdes.2019.110313 (cit. on p. 57).

[57] Christian Fedon, Elias Y. Garcia Cervantes, Lino Salamon, and Bernard Erasmus. «Application of deterministic sampling methods for uncertainty quantification in manufacturing tolerances in neutron physics». In: *Nuclear Engineering and Design* 373 (2021), p. 111023. DOI: 10.1016/j.nucengdes.2020.111023 (cit. on p. 57).

[58] Seyed Ali Hosseini, Reza Akbari, Amir Saeed Shirani, and Francesco D'Auria. «Analysis of the natural circulation flow map uncertainties in an integral small modular reactor». In: *Nuclear Engineering and Design* 378 (2021), p. 111156. DOI: 10.1016/j.nucengdes.2021.111156 (cit. on p. 57).